João Miguel Matos Nunes

Licenciado em Ciências da Engenharia Civil

Adaptive Tuned Mass Damper (ATMD) based in shape-memory alloy (SMA) elements.

Dissertação para obtenção do Grau de Mestre
em Engenharia Civil - Perfil de Estruturas

Orientador: Professor Doutor Filipe Amarante dos Santos
Professor Auxiliar, FCT/UNL

Júri:

Presidente: Prof. Doutora Zuzana Dimitrovová
Arguente: Prof. Doutor Corneliu Cismasiu
Vogal: Prof. Doutor Filipe Amarante dos Santos

FACULDADE DE CIÊNCIAS E TECNOLOGIA
UNIVERSIDADE NOVA DE LISBOA

Março de 2016

To my grandfather, Prof. Rogério Sanches de Matos

"Só devemos fazer aquilo que realmente enche o nosso coração de entusiasmo. Se deixamos isso de lado, se adiamos o momento de viver aquilo que sonhamos, perdemos a energia necessária para qualquer transformação importante na nossa vida."

Acknowledgments

The present dissertation arises, not only from extensive hours of study, hard work and dedication, but also as the result of a long academic journey, that would not have been accomplished without the support and assistance from many people who have either helped me or encouraged me.

I would like to express my deepest and heartfelt recognition to my adviser, Professor Filipe Amarante dos Santos for the support, knowledge transmission and availability demonstrated throughout the development of this thesis.

I would like to thank Engineer Mirko Maraldi and Professor Luisa Molari, not only for their academic support, but also for the availability and quality care provided during my abroad study experience in Italy.

I would also like to thank Mr. Alberto Cambalacho for the assistance in the preparation of the supports used in the experimental campaign.

I leave words of appreciation to my colleagues, Inês de Carvalho, Pedro Castanho, Bruno Alcobia, Daniel Ferreira, Filipe Loureiro and André Taveira, with whom I had the pleasure of working with and share true friendship moments along the way.

I am also indebted to my comrades André Martins, Nuno Cabral, André Jorge, Diogo Canelas, Pedro Palma, Rafael Silva, Tiago Gonçalves, André Palminha, Tomás Campos and all those omitted by mistake or forgetfulness, for their support and contribute to my growth as an engineer and mainly as human being.

A special thanks to Mafalda Aquino for the unconditional support in the good and bad times, throughout my entire academic career.

Finally, I must express my gratitude towards my dear mother Teresa Matos, my father Carlos Coito, my sister Joana Nunes and the rest of my family for their love, unfailing support and inspiration.

I hope this thesis may be an encouragement for the younger members of my family (Francisco and Mariana), and for all the people who read or work with it.

João Miguel Matos Nunes, March 2016

Abstract

The unique features of shape memory alloys (SMA) gives them an unmatched ability to be implemented in several fields of engineering. Considering their phase shift capacity, when thermoelectrically driven, SMAs assume an elastic modulus variation predicated upon two key parameters - stress and temperature.

Based on the above statement, the present dissertation aims to develop a new vibration control system, which makes use of SMAs in order to extend and improve its operational domain.

Initially, an experimental campaign is developed in order to design a mapping of the elastic modulus of a *FLEXINOL* ® SMA sample.This mapping seeks to explore and an optimize the inclusion of shape memory alloys in vibration control systems.

In a second step, two types of ATMDs (Suppressor and TMD) are mathematically studied in order to comprise the insertion of a SMA element in the control system.

Considering the main purpose of this thesis, a particular case study structure was chosen to carry out the implementation of the new vibration control system. The selected structure consists in a footbridge built over an important highway located in the Lisbon city center, Portugal. At this stage, both the design of the SMA element and the subsequent operational limits are presented.

Afterwards, a numerical model computed in MATLAB (The Mathworks, 2014) is developed to simulate the behavior of a two degrees of freedom (TDOF) system. This one provides the system's behavior (structure + ATMD) towards a predefined harmonic request, evaluating the effects of the implementation of the new vibration control system.

Using the above mentioned numerical model, an influence analysis of both control systems was carried out. Several comparisons between the variants of each ATMD (Suppressor and TMD) where drawn, showing the positive and negative aspects of their action. In the end, a single numerical model, with the ability to excite the structure, read its behavior, identify the vibration frequencies and properly tune the control system in real time, performed a complete structural analysis.

Finally, a concluding chapter is presented, where the obtained results are discussed. This chapter also mentions the main future development prospects, that may be considered in studies conducted by other researchers.

Dissertation produced in LaTeX software.

Keywords:

Shape memory alloys, Elastic modulus, Vibration control systems, Suppressor, Tuned mass damper, Variable stiffness.

Resumo

As características únicas das ligas com memória de forma (LMF) conferem-lhes uma aptidão inigualável para serem implementadas em diversos ramos da engenharia. Tendo em conta a sua capacidade de alteração de fase, quando termoelectricamente accionadas, as LMF assumem uma variação do módulo de elasticidade dependente de dois parâmetros principais - tensão e temperatura.

Posto isto, a presente dissertação tem como principal objectivo o desenvolvimento de um novo sistema de controlo de vibrações, que recorre à utilização de LMFs com o intuito de alargar o domínio do seu funcionamento.

Inicialmente apresenta-se um programa experimental que contribui para a concretização de um dos sub-objectivos desta tese, isto na medida da realização de um mapeamento do módulo de elasticidade em função da temperatura de uma liga de *FLEXINOL* ®. Este mapeamento visa uma tentativa de explorar e optimizar o comportamento das LMF.

Numa segunda fase, dois tipos de ATMDs (Supressor e TMD) são matematicamente estudados por forma a considerar a hipótese da inserção de um elemento constituído por LMF.

Tendo em conta o objectivo principal desta dissertação, recorreu-se a um caso de estudo para realizar a implementação do sistema de controlo de vibrações. Este consiste na análise de uma ponte pedonal construída sobre um importante eixo de ligação rodoviária no centro da cidade de Lisboa, Portugal. Nesta fase, é também apresentado um dimensionamento do elemento de LMF, bem como os limites operacionais associados á sua utilização.

Seguidamente é desenvolvido um modelo numérico em MATLAB (The Mathworks, 2014) que considera a modelação de um sistema de dois graus de liberdade. Este é desenvolvido por forma a obter o comportamento do sistema (estrutura + ATMD) face a uma solicitação harmónica pré-definida, avaliando assim os efeitos da implementação do novo tipo de sistema de controlo de vibrações.

Recorrendo ao modelo numérico desenvolvido, é realizada uma análise da influência que ambos os sistemas de controlo têm no comportamento estrutural. Uma série de comparações são realizadas entre as variantes de cada ATMD, evidenciando os aspectos positivos e negativos associados. É também apresentada uma análise estrutural feita com um modelo numérico completo, com a capacidade de excitar a estrutura, ler o seu comportamento, identificar as frequências de vibração e sintonizar correctamente o sistema de controlo em tempo real.

Para finalizar, é apresentado um capítulo conclusivo, onde os resultados obtidos nesta dissertação são comentados. Neste capítulo são também referidas as principais perspectivas de desenvolvimento futuro, que podem ser consideradas em estudos realizados por outros investigadores.

Dissertação produzida em LaTeX software.

Palavras chave:

Ligas com memória de forma, Módulo de elasticidade, Sistemas de controlo de vibrações, Supressor, Amortecedor de massa sintonizado, Rigidez variável.

Contents

List of Figures

List of Tables

List of Abbreviations, Acronyms and Symbols

Abbreviations and Acronyms

ATMD	Adaptive Tuned Mass Damper
DFT	Discrete Fourier Transform
DOF	Degree of Freedom
DSC	Differential Scanning Calorimetry
FCT	Faculdade de Ciências e Tecnologias
LMF	Liga com Memória de Forma
MDOF	Multi Degree of Freedom
NiTi	Nickel-Titanium alloy
PID	Proportional?Integral?Derivative controller
PSD	Power Spectral Density
SCS	Suppressor with Constant Stiffness
SDOF	Single Degree of Freedom
SMA	Shape Memory Alloy
STFT	Short Time Fourier Transform
SVS	Suppressor with Variable Stiffness
SVST	Suppressor with Variable Stiffness and stiffness Transition
TMD	Tuned Mass Damper
TMDCS	Tuned Mass Damper with Constant Stiffness
TMDVS	Tuned Mass Damper with Variable Stiffness
UNL	Universidade Nova de Lisboa

Symbols

ξ	Martensite phase fraction
ζ	Damping ratio
u	Displacement vector
A	Austenite
M	Martensite
M_s	Martensitic phase Start
M_f	Martensitic phase Finish
A_s	Austenitic phase Start
A_f	Austenitic phase Finish
σ	Stress
σ_M	Martensitic Stress
σ_A	Austenitic Stress
E	Modulus of Elasticity (Young)
E^w	Modulus of Elasticity of the wire
E_M	Modulus of Elasticity in Martensitic phase
E_A	Modulus of Elasticity in Austenitic phase
ε	Strain
ε_M	Strain in Martensitic phase
ε_A	Strain in Austenitic phase
ε_L	Maximum residual Strain
K_p	Proportional gain
K_i	Integral gain
K_d	Derivative gain
e	Error
t	Instantaneous time
τ	Variable of integration
g	Fit parameter
ν	Fit parameter

T_m	Fit parameter
T	Temperature
T^w	Wire temperature
L	Length
ΔL	Length variation
$f\,(T)$	Austenite phase fraction
m	Mass
c	Damping
k	Stiffness
m_1	Mass of the primary system (structure)
m_2	Mass of the secondary system (ATMD)
c_1	Damping coefficient of the primary system (structure)
c_2	Damping coefficient of the secondary system (ATMD)
k_1	Stiffness of the primary system (structure)
k_2	Stiffness of the secondary system (ATMD)
P_0	Amplitude of the force function
f	Vibration Frequency [Hz]
ω	Angular frequency [rad/s]
ω_1	Angular frequency of the primary system (structure)
ω_2	Angular frequency of the secondary system (ATMD)
x	Displacement
$\dot{x}$	Velocity
$\ddot{x}$	Acceleration
X_1	Amplitude of the displacement of the primary system (structure)
X_2	Amplitude of the displacement of the secondary system (ATMD)
X_{st}	Static deflection of the primary system (structure)
r_1	Ratio between the excitation frequency and the frequency of the primary system
r_2	Ratio between the excitation frequency and the frequency of the secondary system
q	Ratio between the TMD frequency and the frequency of the system

μ	Mass ratio between the primary and secondary system masses
ζ_2	Damping ratio of the TMD
$\zeta_{2,opt}$	Optimum Damping ratio of the TMD
$\omega_{2,opt}$	Optimal frequency of the TMD
a_{max}	Maximum acceleration
A	Area (cross section)
d	Diameter
K_M	Stiffness in Martensitic phase
K_A	Stiffness in Austenitic phase
S	Stroke
$\mathbb{M}$	Mass Matrix
$\mathbb{K}$	Stiffness Matrix
$\mathbb{C}$	Damping Matrix
$\underline{u}_0(t)$	Initial displacement vector
$\dot{\underline{u}}_0(t)$	Initial velocity vector
$\underline{P}(t)$	Excitation force vector
γ	Newmark's method stability coefficient
β	Newmark's method stability coefficient

Chapter 1

Introduction

"We shape our buildings, thereafter they shape us." - Winston Churchill

1.1 Problem Description

In the past few years, footbridges have evolved to overcome larger spans and achieve greater lightness to perfectly suit in the surrounding environments. Footbridges are usually steel structures, with great flexibility and low damping ratios, directly influencing their dynamic behavior. The decrease in the stiffness, often leads to structures with lower natural frequencies and with an increased risk of resonance.

With the purpose of mitigating this negative impact on structures, different approaches have been studied over the past few years. A well known vibration control approach is based in the use of Tuned Mass Dampers (TMD). A TMD reduces the vibration of a system with a comparatively lightweight component, stabilizing it against violent motions caused by harmonic vibrations. Roughly speaking, TMDs are currently tuned to either move the main mode away from a troubling excitation frequency, or to add damping excluding the possibility of resonance.

The main problem regarding TMDs usage is related to the fact that they are designed only to be tuned to the structure's natural frequency, which introduces the resonance effect. Therefore, their effect won't become so sharp when the harmonic action comprises other range of frequencies.

In order to overcome the above mentioned weakness, several control systems have been studied. Among the ones reported in the literature, one highlights a device studied by N. Varadarajan and S. Nagarajaiah [42] and S. Nagarajaiah and E. Sonmez [25], where a vibration control system with a property of "variable stiffness" was developed. This "variable stiffness" property allows a correct tuning of the device for a wider range of frequencies.

As in the above described case, the present dissertation studies an Adaptive Tuned Mass Damper (ATMD) device with the same "variable stiffness" property.

1.2 Objectives and Scope

Regarding the previously exposed problematic, the present dissertation aims to develop a new approach on a vibration control system, which increases the performance towards a wider range of vibration exposure. In order to achieve the above mentioned primary objective, different work stages with secondary objectives were considered.

- The first task will address the temperature/stress mapping of a SMA element with respect to its elastic modulus. For this, both an experimental and a numerical approach will be developed.
- In a second stage of the work, two ATMD vibration control systems will be studied considering the hypothesis of the inclusion of a SMA element in the system.
- The third stage regards the full definition of a numerical model based on a simplified two degree of freedom dynamic system implemented in MATLAB (The Mathworks, 2014), to simulate the behavior of the composed structural system (footbridge + ATMD), associated with a dynamic loading.
- Hereupon, through numerical simulations, several comparisons between different approaches on the vibration control system in concern will be considered and finally, some conclusions will be presented.

1.3 Dissertation Outline

The content of the dissertation is organized into the following chapters:

Chapter 1 - General approach to the subject of the present dissertation.

Chapter 2 - General introduction to SMAs, including a description of the superelasticity and shape-memory effects, triggered by martensitic transformations. SMAs applications in Civil Engineering. Constitutive models for SMAs and definition of the Mechanical and kinetic governing laws considered in this document.

Chapter 3 - Detailed description of the Experimental and Numerical approaches on the definition of the Young Modulus Mapping of *FLEXINOL* ® actuator wires. Reference to the proportional-integral-derivative (PID) algorithm used in the experimental tests. Review and application of the defined constitutive model. Comparisons between the different approaches and results.

Chapter 4 - Introduction to the vibration control systems (Suppressor and TMD) studied in this document. Mathematical definition of those two vibration control systems, according to the studies reported by Den Hartog [12].

Chapter 5 - Simplified overview of this document case study. Review of the studies reported by T. Krus [15]. Geometry, structural aspects and analysis of the case study footbridge. Implementation of a vibration control system in the Footbridge. Inclusion of the "variable stiffness" property in the considered vibration control systems, using SMAs, in order to increase their performance. Definition of the operating limits of both ATMDs.

Chapter 6 - Numerical implementation of the active control strategy, based on a Simplified Two Degree of Freedom Dynamic System. MATLAB (The Mathworks, 2014) implementation of the two Vibration Control Systems (Suppressor and TMD) previously studied. Definition and numerical implementation of a frequency tracking algorithm based on short-time Fourier transforms (STFT), to determine the real-time frequency of a sinusoidal signal as it changes over time.

Chapter 7 - Analysis of the results yielded by the numerical tests performed. Definition of the initial vibration problems of this case study footbridge, considering the developed numerical model. Single Numerical Model with the STFT frequency tracking algorithm in the Output response signal of the structure.

Chapter 8 - Summary of the proposed dissertation, conclusions and future research suggestions.

Chapter 2

Shape Memory Alloys

2.1 Introduction to Shape Memory Alloys (SMA)

In the present chapter, the main concepts underlying the definition of Shape Memory Alloys and their applications in Civil Engineering, are introduced. In the small group of smart materials, Shape Memory Alloys (SMAs) belong to a class that gives them the capacity to memorize their previous characteristics when subjected to certain kinds of stimulus such as thermomechanical variations. Taking advantage of their unique features and considering the research being developed, SMAs have drawn significant attention in a wide range of commercial applications, in the latest years.

SMAs are characterized by two main thermo-mechanical properties, the Shape Memory Effect and Superelasticity. The application of both properties, as well as the functioning of the material itself, is highly related with a diffusionless phase transformation, characteristic of SMAs, called martensitic transformation. Due to this transformation, the material atoms rearrange themselves differently according to external factors like Temperature or Stress variations. The two main types of atom rearrangements, yield to two different phases, Martensitic and Austenitic phase.

In 1932, the Swedish physicist Arne Ölander, discovered the superelastic behavior of an Au-Cd alloy. Then in 1938, Greninger and Mooradian observed the formation/disappearance of a martensitic phase when they decreased/increased the temperature of a Cu-Zn alloy. Only after a decade, in 1949, the Shape-Memory Effect phenomenon due to the thermoelastic behavior of the martensitic phase was reported by Kurdjumov and Khandros and also by Chang and Read (1951). The development of the Nickel and Titanium Shape-Memory Alloys (NiTi Alloys - Nitinol), occurred between 1962-1963 by the United States Naval Ordnance Laboratory, after their properties have been accidentally discovered by Dr. David S. Muzzey.

2.2 General aspects of Shape Memory alloys

Although SMAs can be composed by different chemical elements, this document only considers the ones composed by Nickel and Titanium alloys (NiTi SMAs), mostly known as Nitinol wires.

As mentioned in this chapter's introduction, SMAs are characterized by two important thermo-mechanical properties:

- Superelasticity;
- Shape-Memory effect.

Both mentioned thermo-mechanical properties are based upon martensitic transformations. Those properties and transformations are described in detail in the following sections.

2.2.1 Operating principles of SMAs

SMAs are characterized by comprising two main phases, where the internal organization of the crystals changes according to Temperature/Stress variations:

- Austenitic Phase;
- Martensitic Phase.

Both phases are further described in Table 2.1.

Table 2.1: Austenite and Martensite phases.

Austenite	**Martensite**
"Elastic behavior" phase	"Plastic behavior" phase
"Stronger" phase	"Weaker" phase
Stable at high temperatures	Stable at low temperatures
Cubic crystal structure	Monoclinic crystal structure

In order to clarify the operation of SMAs, the Figure 2.1 diagram is presented, illustrating the transition between the two mentioned crystallographic phases as function of temperature.

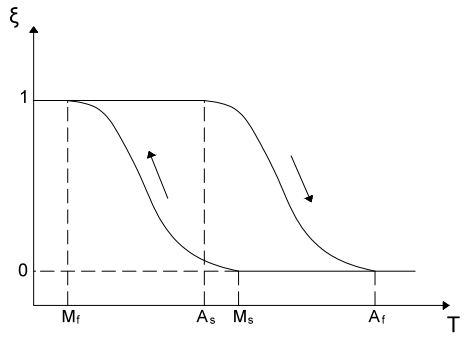

Figure 2.1: Phase alternation with respect to temperature. [38]

Figure 2.1 presents the relation between the Temperature (T) and the martensite phase fraction (ξ). The martensite phase fraction comprises values between 0 and 1, where 1 corresponds to the complete martensitic phase and 0 corresponds to the complete austenitic phase. With this, it is possible to observe that as the temperature increases, a phase transition from martensite to austenite occurs in the alloy. In order to define the start and finish point of each phase transition process, the following transformation temperatures are presented:

M_s - Martensitic phase Start.

M_f - Martensitic phase Finish.

A_s - Austenitic phase Start.

A_f - Austenitic phase Finish.

2.2.2 Superelasticity

The Superelasticity thermo-mechanical property of SMAs is a result of the internal rearrangement of the alloy crystals which gives to the SMA a higher elastic recovery in comparison to the metals and commonly used alloys. In SMAs, Superelasticity is associated with recoverable strains up to 8% during a mechanical cycle of loading and unloading that, when compared to 0.2% of the common alloys, represents a considerable increase.

To illustrate this phenomenon, one considers the example of a single SMA column (in the austenitic phase) with a fixed support at its basis and with the other edge free (Figure 2.2).

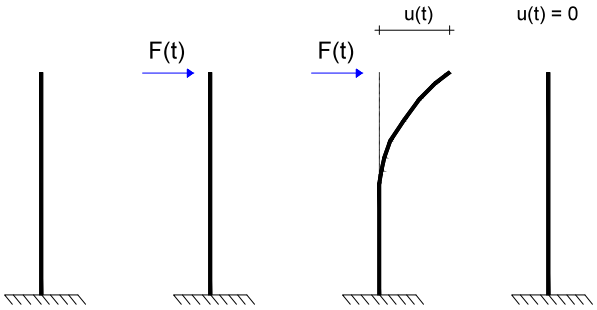

Figure 2.2: Superelasticity effect. Residual strain: $u_0 = 0$; Temperature variation: $\Delta T \approx 0$. (Adapted from [33]).

When a single load is applied at the free top edge of the column, it triggers a deformation process in that element. Due to its superelastic properties, when the load is removed, the column returns to its initial configuration, without any residual deformation.

2.2.3 Shape Memory effect

As the name implies, this property allows the alloy to recover its undeformed configuration after being subjected to a positive variation of its temperature. This positive variation of temperature must be within a range of values that allows martensitic transformations to occur. SMAs can be subjected to many shape-memory cycles without any loss of resistant stress.

To illustrate this phenomenon, one considers the example of section 2.2.2 but, this time, the SMA column is initially in the martensitic phase (Figure 2.3).

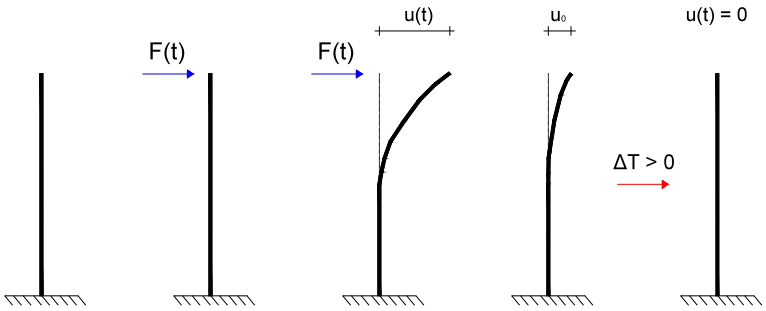

Figure 2.3: Shape Memory effect. Residual strain: $u_0 > 0$; Temperature variation: $\Delta T > 0$. (Adapted from [33]).

With the application of the single load, the column suffers an induced deformation process and when reaching a certain stress value, it enters into a plastic regime.

Unlike in the superelasticity phenomenon, when the load is removed, the column does not return to its original shape. This is due to the fact that the column comprised a plastic deformation and thus, a residual strain needs to be considered (the column recovers only part of the total strain to which it was subjected).

However, a positive temperature variation can be introduced into the system causing a phase transition from martensite to austenite, and then the structure will be able to completely recover its original shape. This phenomenon is called the shape memory effect.

The above represented cycle may be repeated many times without changes in the material properties.

To summarize the whole operation of NiTi alloys, Figure 2.4 presents a sequence of martensitic transformations which demonstrate the superelastic and shape memory behavior of this type of SMA.

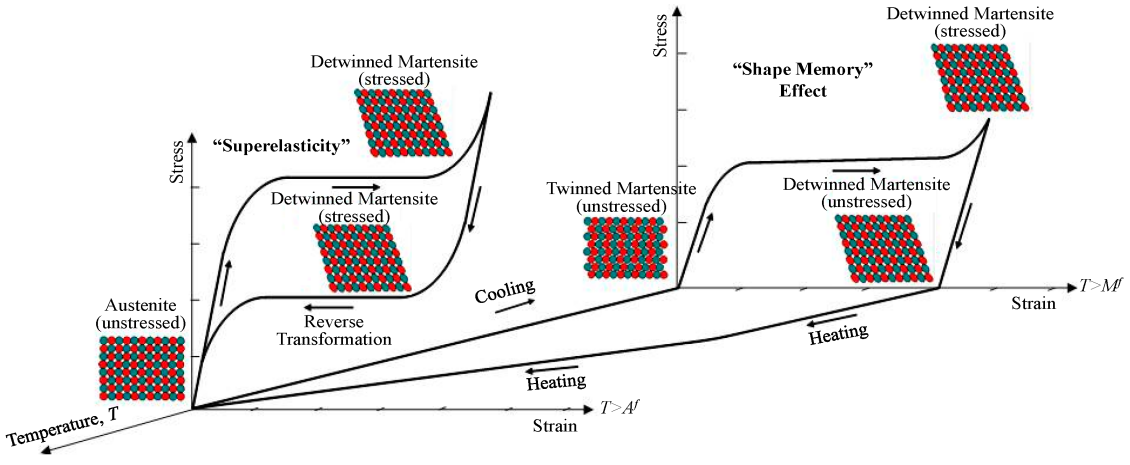

Figure 2.4: Properties of Shape-memory-alloys. Relations between Stress, Strain and Temperature. [34]

In accordance with Figure 2.4, when in a low temperature phase (Martensite) one applies a stress variation to the material, it suffers a continuous deformation without recovery of the original shape upon stress removal. Then, with the induction of a positive temperature variation, the alloy's crystals rearrange themselves differently, changing from a martensitic

phase to an austenitic one. Due to the "shape-memory effect", the alloy is now able to recover its undeformed shape. When in the austenitic phase, one applies a stress variation, the material will experience the expected deformation, but this time, upon the removal of the applied stress, it is able to completely recover the undeformed shape. This phenomenon occurs due to the "Superelasticity" property, characteristic of the austenitic phase.

2.3 Shape Memory Alloys in Civil Engineering

Nowadays, SMA's applications in civil engineering structures are quite occasional, even though, they begin to be more frequently seen in several applications. Perhaps the most relevant one is the application of SMA's in vibration control devices, mainly implemented in buildings and footbridges, which is the main subject of the present dissertation.

The application of these alloys is also increasing, in structural rehabilitation. The ability of this material to recover its original shape can be very useful in structural rehabilitation and also in the field of self-rehabilitation of damaged structural elements.

Most of the SMAs implementation examples in civil engineering structures, can be observed in Italy, with several successful cases of real applications of SMA materials. Most of these applications are related with the rehabilitation of historical structures damaged by seismic events [22] [13] [38].

Some studies, regarding the use of SMAs in vibration control systems, have also been conducted in other areas of civil engineering, such as Tensegrity structures [30]. SMAs are also often used to improve the behavior of several types of structures [1] [27], or even in specific structural elements [40].

Even though the use of SMAs may increase the structures performance, it always requires a substantial amount of material. This may be an important restraint to their implementation due to their high price, when compared with other conventional construction materials [31].

2.4 Constitutive Models for Shape-Memory Alloys

2.4.1 Introduction

In order to describe the highly complex behavior of Shape-Memory Alloys, different constitutive models have been developed. Each of these models takes into account the properties of SMAs that must be considered for a particular study, making the model more suitable for the study in concern.

These models are usually constituted by two main coupled laws, the Kinetic Law and the Mechanical Law. The Kinetic Law is used to describe the evolution of the phase fraction as a function of stress and temperature, governing the process of the crystallographic transformation between phases, while the Mechanical Law is mainly concerned with the stress-strain behavior of the alloy itself.

There are many constitutive models for SMAs available in the literature (references to these models can be found in [31] [3] [16] and [6]). The major difference between the different types of constitutive models is related with the consideration (or not) of the transformation rate and consequently the time factor. For this study the most appropriate model should understand that same factor. However, the constitutive model used in this study is based in [6] (Mechanical law) and [47] (Kinetic law).

2.4.2 Kinetic law

Several phenomenological kinetic equations have been proposed in the literature to describe kinetic data of different constitutive models for NiTi SMAs. These equations cover a wide range of mathematical approaches to the kinetic data, ranging from Exponential laws [39], Cosine based laws [16], Linear and Tangentially laws [14] and even Square-rooted based laws [17].

In order to mathematically describe the evolution of the degree of Martensitic transformation regarding the temperature, the kinetic law presented by Nikolay Zotov, Vladimir Marzynkevitsch and Eric J. Mittemeijer [47] is adopted in this work.

This model is based on the kinetic data (for Austenite fraction) obtained by DSC (differential scanning calorimetry) during the $M \rightarrow A$ transformation in order to obtain a better agreement with experimental data than the existing empirical models. Due to the fact that the transformation issues of NiTi SMAs depend on the composition and on the thermo-mechanical treatment of the alloys, in the referred article, the DSC analysis was applied to two NiTi SMAs with different compositions (nearly-equiatomic NiTi SMAs (50.1 at.% Ni) and Ni-rich NiTi SMA (50.7 at.% Ni)), but for the sake of simplicity, the present study will only focus on the nearly-equiatomic NiTi SMAs.

With the DSC test results obtained (see Figure 3.8), the degree of transformation can be determined from the enthalpy of the transformation, expressed by the area of the DSC graphic peak. According to [47], a baseline-corrected and *unsmeared* DSC curve, can be obtained using:

$$F_u(t) = F_m(t) + \frac{\tau \, dF_m(t)}{dt} \tag{2.1}$$

where $F_m(t) \sim \frac{d\Delta H}{dt}$, ΔH is the enthalpy change of the SMA specimen and τ is a time constant.

In order to preform the kinetic analysis of the austenite formation as a function of temperature, the data obtained from the DSC curves described above (mainly the baseline-corrected and *unsmeared* DSC curve given by equation (2.1)) can be used to find the austenite phase fraction applying:

$$f(T) = \left(\frac{1}{\Delta H_A}\right) \int_0^T F_u(y)dy \tag{2.2}$$

Where ΔH_A is the total enthalpy change of the $M \rightarrow A$ phase transformation and F_u is the unsmeared heat flux (2.1).

To obtain a more realistic description of the experimental kinetic data than the existing SMA kinetic models, Nikolay Zotov, Vladimir Marzynkevitsch and Eric J. Mittemeijer [47] proposed:

$$f(T) = \frac{1}{(1 + \exp(-g\nu(T - T_m)))^{\frac{1}{\nu}}} \tag{2.3}$$

Equation (2.3) describes the evolution of the Austenite phase fraction as function of Temperature, and it is ruled by three fit parameters (g, ν, T_m) that have simple physical meanings. T_m determines the temperature corresponding to the maximum transformation rate $(df/dT)_{max}$, g and ν determine the transformation rate (df/dT).

This type of kinetic equation approach is able to describe the experimental kinetic data and thus is applicable to a range of NiTi shape memory alloys of different compositions, microstructures and thermomechanical histories.

2.4.3 Mechanical law

In order to perform a stress-strain ($\sigma - \varepsilon$) analysis related to the temperature (T) and martensite phase fraction (ξ) of SMAs, a mechanical law is implemented. There are three main approaches that consider transformation phase fraction to be related with the elastic fraction of the response. According to [6], if the elastic fraction of the response is limited to the austenite phase, a simple serial model is obtained (see Figure 2.5a). If a parallel distribution of austenite and martensite phases is considered, a Voight scheme is obtained (see Figure 2.5b). If a periodical distribution of austenite and martensite phases within the material, orthogonal to the direction of the applied stress is considered, the Reuss scheme is obtained (see Figure 2.5c).

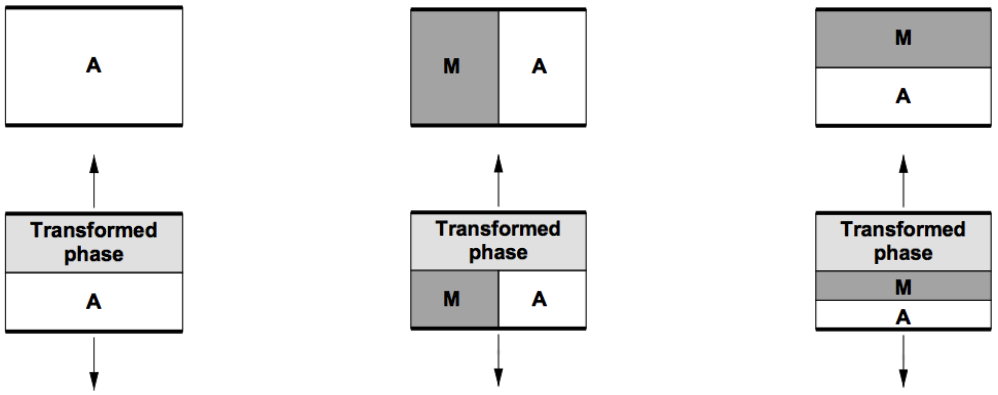

(a) Simple serial model (b) Voight scheme (c) Reuss scheme

Figure 2.5: Mechanical models for SMAs, [6]

Due to the interest of reporting the evolution of the Young Modulus regarding the temperature, is necessary to take into account the two main phases that occur in this material, as well as the length of variations between phases. Therefore, this document will only address the Voight and Reuss schemes which contemplate those two different crystallographic phases, austenite and martensite.

2.4.3.1 Voight scheme

Assuming that the austenitic and martensitic elastic strains are equal ($\varepsilon_{elast} = \varepsilon_M = \varepsilon_A$), the mechanical law governing the behavior of the material can be expressed as:

$$\sigma = \xi\,\sigma_M + (1 - \xi)\,\sigma_A \tag{2.4}$$

and considering Hooke's Law ($\sigma = E\,\varepsilon$), it is possible to obtain the following relationship, or "rule of mixture" [36]:

$$E^w = \xi\,E_M + (1 - \xi)\,E_A \tag{2.5}$$

Where E^w is the Young's Modulus of the SMA wire calculated from the martensite E_M and austenite E_A modulus, each of them representing an implicit constant of the material.

2.4.3.2 Reuss scheme

According to Reuss scheme, the prerequisite for the formulation of its mechanical law is based on the assumption that the total strain of the material depends on the percentage of phase associated with it, i.e:

$$\varepsilon = \xi\,\varepsilon_M + (1-\xi)\,\varepsilon_A \tag{2.6}$$

Considering the total stress in each phase, the individual phase strains are given by: $\varepsilon_A = \frac{\sigma}{E_A}$ and $\varepsilon_M = \frac{\sigma}{E_M} + \varepsilon_L$. Equation (2.6) results in:

$$\sigma = \frac{E_A\,E_M}{\xi\,E_A + (1-\xi)\,E_M}\,(\varepsilon - \varepsilon_L\,\xi) \tag{2.7}$$

Where ε_L is the maximum residual strain in the material. Considering Hooke's Law once again, the Young Modulus relation for the Reuss scheme can be expressed as:

$$E^w = \frac{E_A\,E_M}{\xi\,E_A + (1-\xi)\,E_M} \tag{2.8}$$

2.4.4 Constitutive Model Summary

In order to summarize the considered constitutive model as well as its constitutive laws, Table 2.2 is presented below.

Table 2.2: Constitutive Model for SMAs - Summary

Kinetic Law	[47]	$f(T) = \frac{1}{(1+\exp(-g\nu(T-T_m)))^{\frac{1}{\nu}}}$ (2.3)
Mechanical Laws	Voight	$E^w = \xi\,E_M + (1-\xi)\,E_A$ (2.5)
	Reuss	$E^w = \frac{E_A\,E_M}{\xi\,E_A+(1-\xi)\,E_M}$ (2.8)

Chapter 3

Mapping of the SMAs Modulus of Elasticity

3.1 Introduction

The behavior of the SMAs Young's modulus in a thermal cycle is a very interesting issue for the study of the application of these materials. Several articles in the literature already describe this specific behavior of SMA wires [47] [36].

Hereupon, one considers the mapping of the SMAs Young Modulus as the leading objective of the present chapter.

Although each crystallographic phase has a particular value of Young's Modulus associated with it, a non-linear and hysteretic dependence of the wire modulus $E^w = E^w(T)$, which occurs during the phase transition interval, is considered to be the focus of the present chapter.

In order to do this, two different methods were used. First, an experimental test was performed, where the modulus of elasticity of the NiTi wire was calculated based on the Hooke's law concepts, while in the second method, the calculation of the modulus of elasticity relied upon the use of the constitutive models specified in section 2.4, that have been based on a DSC analysis performed on the same NiTi wires.

3.2 SMA wire characteristics

The SMA wires used in this work were provided by *Dynalloy, Inc.* These small diameter *FLEXINOL* ® wires are made of Nickel and Titanium and they are able to contract when electrically driven or heated. Their ability to flex/shorten is considered a characteristic of SMAs, which dynamically change their internal structure when submitted to certain temperatures.

The NiTi wires have a 0,5 *mm* diameter, are straight, oxide free and can remember its shape at both high/low temperatures. The strength of the wire and its pulling force are function of the wires size and cross sectional area. According to the *FLEXINOL* ® catalog, if a load of 103 MPa is maintained during cooling, then nearly 5% memory strain will be obtained, and when heated through the transformation temperature, the wire will shorten by the same 4-5% that it was stretched, exerting stresses of 172 MPa when doing so. It is also important to refer that at stresses below 103 MPa, permanent strain will remain under 0,5%, even after hundreds of thousands of cycles.

The modulus of elasticity of SMA wires can vary considerably with composition, elongation, training, and temperature. For NiTinol, in the low temperature phase (Martensite), it varies between 28-40 GPa and in the high temperature phase (Austenite), it is around 83 GPa.

According to the *FLEXINOL* ® catalog the transformation temperature of the actuator wire is set around 60°C and 110°C (As = 90°C). This allows an easy heating process with modest electrical currents applied directly through the wire, and a quick cooling process to temperatures below the transformation temperature as soon as the current is stopped.

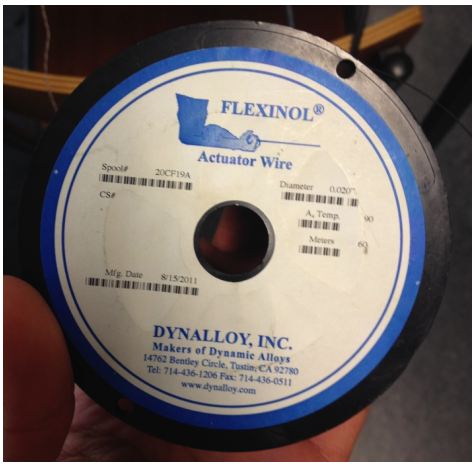

Figure 3.1: *FLEXINOL* ® actuator wire.

Relevant physical properties of *FLEXINOL* ®:

- Diameter: $0,5$ mm;
- Density: $6,45$ g/cm^3;
- Specific heat: $0,2$ cal/g.°C;
- Melting point: 1300 °C;
- Thermal Conductivity: $0,18$ W/cm °C;
- Thermal expansion coefficient:
  - Austenitic phase: $11,0 \times 10^{-6}$ /°C;
  - Martensitic phase: $6,6 \times 10^{-6}$ /°C;
- Approximate electrical resistance:
  - Austenitic phase: 100 micro-ohms.cm;
  - Martensitic phase: 80 micro-ohms.cm;

3.3 Experimental mapping - Young modulus of the SMA wire

In order to characterize the Young's modulus of the *FLEXINOL* ® alloy as function of temperature (and the applied stress, σ), an experimental procedure was conducted. To properly represent the application of the spring element of a TMD (tuned mass damper) in a reduced scale, the experimental structure was composed by a support, a SMA wire and a suspended mass.

The importance of the test to be performed in this way is due to the necessity of the SMA wire to be able to comprise vertical displacements at the bottom end, consequently extending and compressing freely both when subjected to a stress variation and/or a temperature variation, as in a real TMD. Regarding this fact, the test could not be accomplished with a conventional tensile test machine (example: *Zwick-Z050*) because in this way, both edges of the wire would be fixed, allowing no extension/contraction.

3.3.1 Experimental Device

The experimental device was composed of a main support and a $0,45\,m$ SMA wire suspending an attached mass, as shown in Figure 3.2. The SMA wire was attached to the two supports (main support and weights support) by clamps fixed on both edges. It is important to note that the upper base of the main support is an element of high stiffness, preventing any deformation at the mid span of the upper plate, that could occur during the loading procedure.

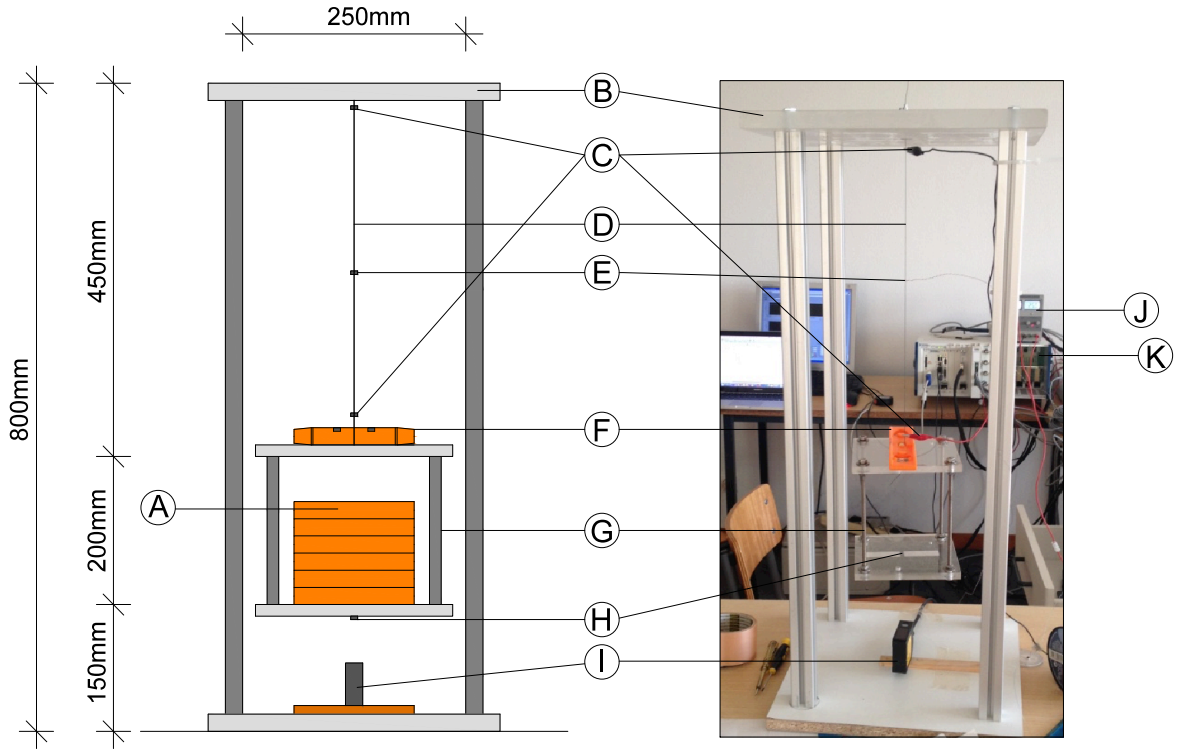

Figure 3.2: Experimental Device.

A - 1kg weights (each)

B - Main support

C - Electrical connectors

D - SMA wire sample

E - Thermocouple

F - Leveler device

G - Weight support

H - Laser target

I - Baumer Photoelectric sensor CH-8501 Class 2 laser

J - Kaise DC power supply hy3005d

K - *National Instruments* NI PXI-1052

Six weights of 1kg each were placed in the weights support, allowing for an increment of stress in the wire sample. The wire sample was electrically driven by two electrical connectors linked to a power source controller and connected to a power supplier that produces an electric potential difference, causing a thermal variation in the sample. To measure the wire's temperature in real time, a thermocouple was placed in the center of the wire sample. This thermocouple was connected to the *National Instruments* NI PXI-1052.

Figure 3.3: *National Instruments* NI PXI-1052 controller and *kaise DC power supply hy3005d.*

The *National Instruments* NI PXI-1052 offers advanced analog and digital signal conditioning, isolation, timing and synchronization features making this equipment very useful in a wide range of applications.

As it can be seen in Figure 3.4, a *Baumer Photoelectric sensor CH-8501 Class 2 laser* (supplied by a *kaise DC power supply hy3005d*), pointing into a target positioned at the bottom side of the support for weights, was placed under the support for weights in order to record the vertical displacements experienced by the wire throughout the whole test. This laser was also connected to the *National Instruments* NI PXI-1052 referred above. To ensure the verticality of the load and the suitability of the readings made by the laser, a leveler device was placed at the upper face of the weight support allowing to make adjustments when placing each load increment in the wire.

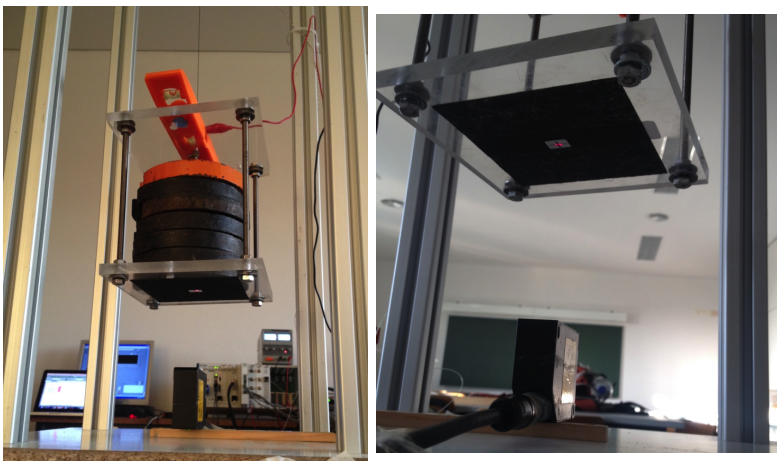

Figure 3.4: *Baumer Photoelectric sensor CH-8501 Class 2 laser*, Target and Leveler device.

The entire experimental process was monitored by the graphical environment of *LabVIEW* (*National Instruments*), which comprises a PID control algorithm for the temperature of the SMA wire in real time. The wire's temperature values read by the thermocouple, are computed into the *LabVIEW* platform in real time and then, through the PID algorithm, the platform is able to calculate the voltage required to apply to the SMA wire to achieve the desired temperature. As mentioned above, the heating process of the alloys is accomplished by Joule effect through the application of an electrical current. The cooling process is done by convection and therefore does not require any electric current in the wire sample.

In the *LabVIEW* VI two main windows can be found, one showing the lengthwise displacement that occurs in the wire in real time, while the other one shows the temperature of the same wire in real time as well.

3.3.2 Experimental Method

The test performed in this section approaches a typical tensile test, applying an increasing uniaxial tensile load on a specific specimen, but in this case, without reaching rupture (failure state). With this type of test, all the deformations brought into the material are uniformly distributed throughout the sample and, as the load increases in a reasonably slow speed, the tensile test allows a satisfactory measurement of the strain of the material.

All the steps performed during the experimental test are subsequently described below:

1. *Initial step*

   First, to obtain a proper application of the load, an initial weighing of the "weights support" was performed since this one is also suspended, counting as a load to the wire. Afterwards, in order to start the experimental procedure, all components were placed together. In this initial step, the wire supported no load (except the one corresponding to the weights support) and the laser beam was directly pointed to the target. In the *LabVIEW* environment, both wire temperature and strain are displayed and controlled.

2. *Temperature definition*

   A 20°C wire temperature (more or less the room temperature) was the experiment starting point. To achieve this temperature, the values read by the thermocouple were computed, in real time, to the *LabVIEW* platform and through the PID algorithm the platform was able to calculate the required voltage to be applied in the wire sample.

   During the experimental test, the PID algorithm compares the value of the instantaneous temperature of the wire (read by the thermocouple) with a target temperature value previously set, calculating the error and consequently the response to be imposed to the system, in order to change the wire's temperature. This process is repeated sequentially until the desired temperature becomes reached.

   A detailed description of this Proportional-Integral-Derivative controller (PID controller) is presented in the Appendix B of this dissertation.

   As 20°C was considered the room temperature, the wire length remained the same (0.45 m) and the data read by the laser comprised 0 mm of uniaxial extension.

3. *Loading procedure*

   By adding the 1kg weight to the "weights support", the first vertical displacement value was read by the laser sensor. Knowing the initial and final length of the wire (before and after the first loading), the total deformation ratio (strain) was calculated considering:

$$\varepsilon = \frac{\Delta L}{L} \tag{3.1}$$

   Where L is the initial length of the wire and ΔL is the value read by the laser sensor.

   Then, the second 1kg weight was added and new length measurements were obtained. The entire process was repeated until the maximum load (6 kg) is reached. It is important to note that according to *FLEXINOL* ®'s catalog, 345 MPa is the maximum yield strength defined for the high temperature phase and one must not exceed this limit. As 335,7 MPa was the major stress applied to the wire during the whole experimental test, the above mentioned recommendation was fully considered.

4. *Data recording*

   Considering a specific test temperature, all vertical displacement values were recorded (in mm) for each stress increment (in MPa), allowing to obtain a Stress Vs. Strain relation for the material, for the given temperature. It can be seen in Figure 3.5 that, as the stress in the wire increases, the strain also increases almost linearly.

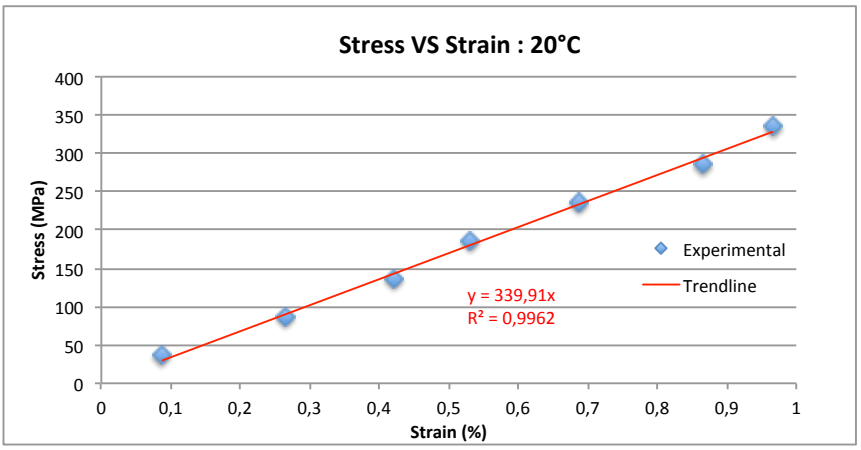

Figure 3.5: Stress - Strain curve for a 20°C temperature

   Using a linear regression (see Figure 3.5), it is possible to define a representative linear function containing a particular slope value. This slope corresponds to the Young modulus value of the SMA wire for the defined temperature. In this case (Figure 3.6a), the Young modulus obtained for a 20°C wire's temperature is $E^w = 33,99$ GPa.

5. *Temperature definition 2*

   In this step, all weights were removed from the "weights support" and the laser was reset to zero. Subsequently, through the aforementioned PID control algorithm, the wire's temperature was entirely increased by 10 °C, allowing the measurement of a new wire's length, caused by the heating effect. Finally, with the new temperature imposed, the laser is once again reset to zero and the loading procedure previously mentioned is reapplied.

6. *Next Steps*

   Steps 3, 4 and 5 were consecutively repeated with temperature increments in the order of 10 °C, from 20 °C up to a final temperature of 110 °C. When dealing with this temperature range, it is possible to ensure that the wire sample has suffered a phase transition from martensite (low temperature) to Austenite (high temperature).

3.3.3 Results

Before introducing the results of the above mentioned test, it is necessary to take into account that the accuracy of a tensile test strongly depends on the precision of the measurement devices used. With minor stress, deformation and temperature increments, it may have been possible to achieve higher precision results evaluating the stress-strain behavior of the wire sample.

The graphical results for the ten temperature values imposed to the wire are listed below.

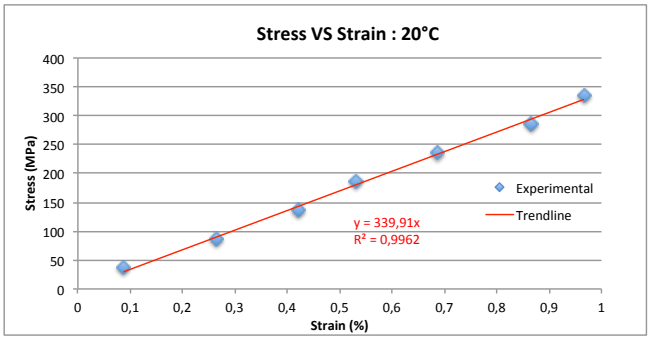

(a) Stress-Strain curve for 20°C

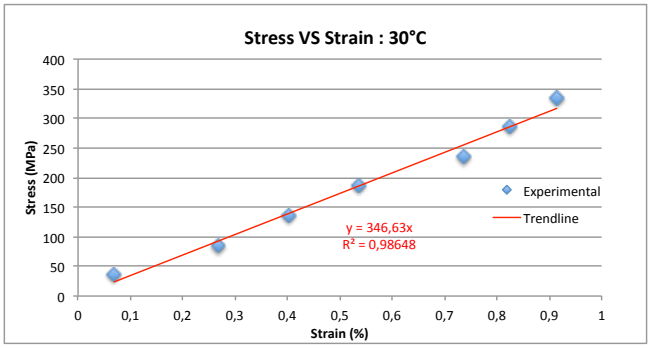

(b) Stress-Strain curve for 30°C

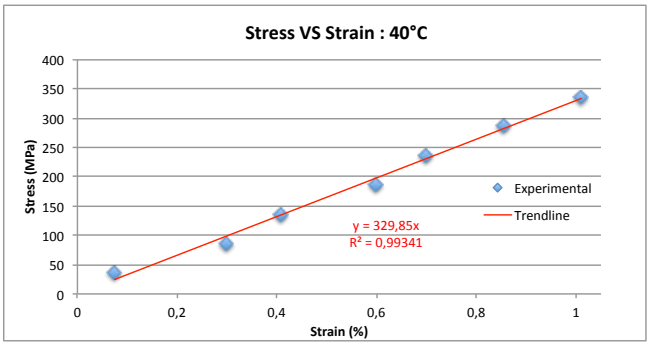

(c) Stress-Strain curve for 40°C

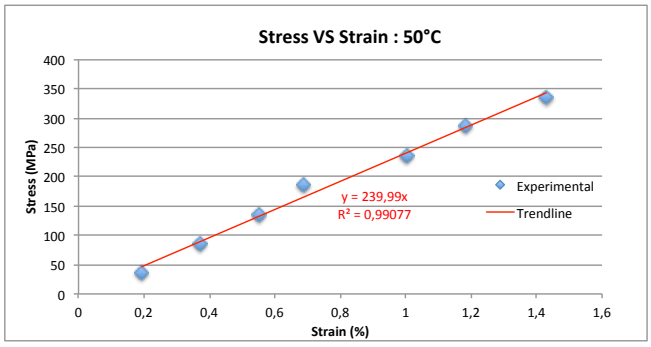

(d) Stress-Strain curve for 50°C

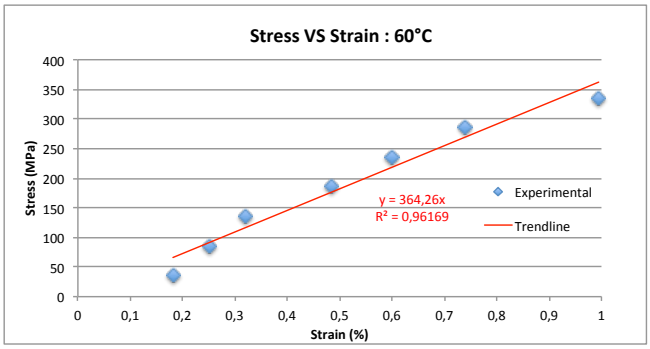

(e) Stress-Strain curve for 60°C

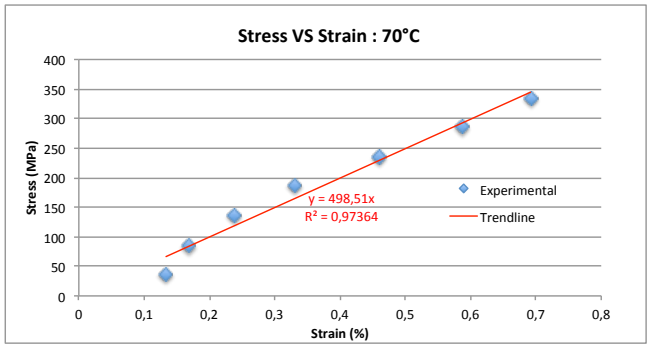

(f) Stress-Strain curve for 70°C

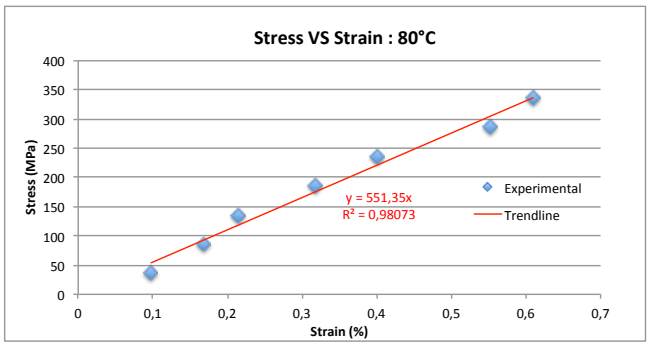

(g) Stress-Strain curve for 80°C

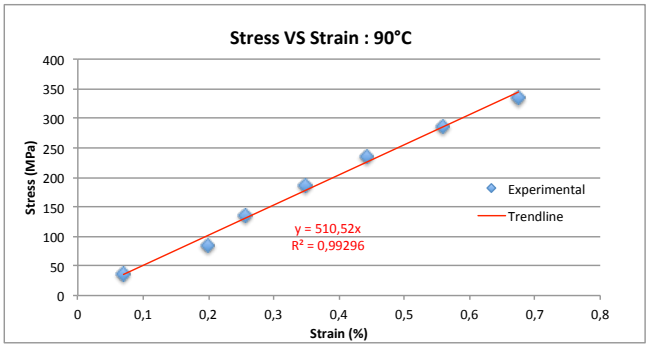

(h) Stress-Strain curve for 90°C

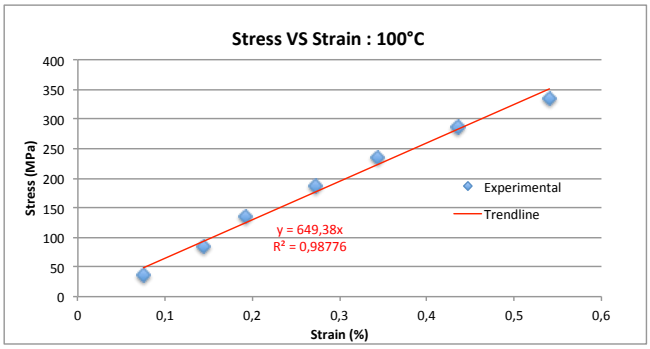

(i) Stress-Strain curve for 100°C

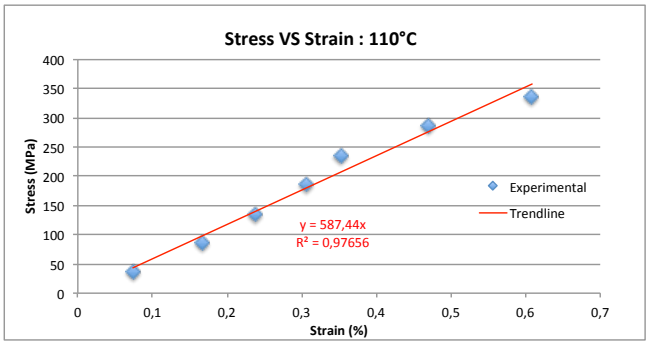

(j) Stress-Strain curve for 110°C

Figure 3.6: Stress-Strain curves obtained for the considered temperature range.

In the previously presented graphics, one can observe a similar behavior of the wire sample regardless of the temperature to which it is subjected, where the stress-strain curve presents a linear increasing behavior throughout its whole domain.

The main difference observed between graphics is related with the slope values. This effect consolidates the increase of the modulus of elasticity for positive temperature variations.

Regarding the shape recovery force exerted by the *FLEXINOL* ® wire, it is possible to observe (from 60°C) a reduction in the wire's extension (in %) when subjected to the same loads but for higher temperatures. This contraction effect can be easily noticed when the wire's length measurements depend only on the increasing temperature (with no loading).

Table 3.1: Wire length with no loading.

Temperature T(°C)	Wire length (m)
20	0.45
30	0.4496
40	0.4486
50	0.445
60	0.4305
70	0.43005
80	0.43
90	0.43
100	0.43
110	0.43

It can be seen in the previous table (Table 3.1), that as the temperature increases, the total length of the wire sample decreases. This reduction occurs from 0,45 m to 0,43 m, which is a contraction around 4.44% (between 4 and 5%) of the initial length. This value is in accordance with the *FLEXINOL* ® specifications mentioned in section 3.2. It is noteworthy that upon reaching 80°C (approximately As temperature) the variation of the wire's length (due to the increasing temperature) reaches a minimum value of 0,43 m.

In order to summarize the evolution of the modulus of elasticity of the SMA wire in this experimental test, Table 3.2 is presented bellow. This table contains the equations of the linear regressions for each graphic of Figure 3.6 as well as the values of Young's modulus associated to each temperature value.

Table 3.2: SMA wire Test Results

Temperature T (°C)	Trend line	Young's Modulus E (Gpa)
20	y = 339,91 x	33.99
30	y = 346,63 x	34.66
40	y = 329,85 x	32.98
50	y = 239,99 x	23.99
60	y = 364,26 x	36.42
70	y = 498,51 x	49.85
80	y = 551,35 x	55.13
90	y = 510,52 x	51.05
100	y = 649,38 x	64.93
110	y = 587,44 x	58.74

From the data of Table 3.2, it is possible to plot a scattering map, where one can observe the behavior of the modulus of elasticity as function of temperature.

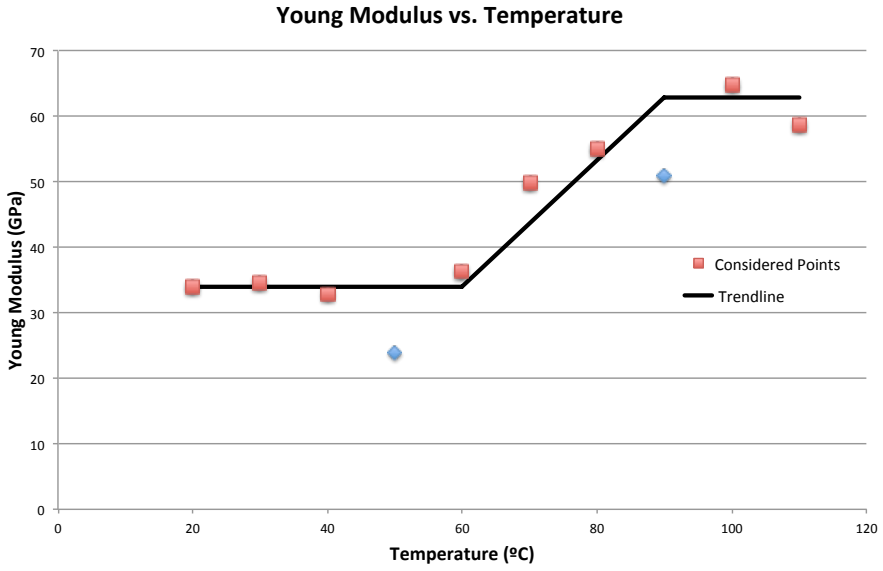

Figure 3.7: Modulus of elasticity as function of temperature.

In the previous graphic (Figure 3.7), one can observe the existence of a horizontal initial baseline (between 20°C and 60°C), followed by an increasing line (between 60°C and 100°C) which turns out to horizontally stabilize after that temperature range. Looking back at the vertical axis (E), it is concluded that initially the wire presented a modulus of elasticity around 34 GPa (in martensitic phase) followed by an increase and a new stabilization of the E values around 65 GPa (in austenitic phase).

With the proposed experimental procedure, it was possible to establish a clear relation between the Modulus of Elasticity of the SMA wire and its temperature.

For a more detailed analysis of the results for the whole experimental test, all the experimental data is described in the appendix A of this document.

3.4 Numerical approach - Young modulus of the SMA wire

Using the formulations presented in section 2.4, one will now implement a constitutive model, representative of the behavior of the wire sample, comprising a Kinetic Law and a Mechanical Law.

3.4.1 Kinetic law

In order to characterize the austenite phase fraction of the NiTi wire sample as function of temperature, the results from a differential scanning calorimetry (DSC) test, performed in [32] using a SETARAM-DSC92 thermal analyzer, have been taken into account. The sample, tested as received, was submitted to a thermal cycle, heated up to 130°C, held at this temperature for 6 minutes, and then cooled to -20°C, with heating and cooling rates of 7,5°C/min. As it is referred in [32], before the DSC experiment, the sample was submitted to a chemical etching (10 vol.% HF + 45 vol.% HNO3 + 45 vol.% H2O) in order to remove the oxide and the layer formed by the cutting operation. The results of the DSC test are presented in Figure 3.8 bellow.

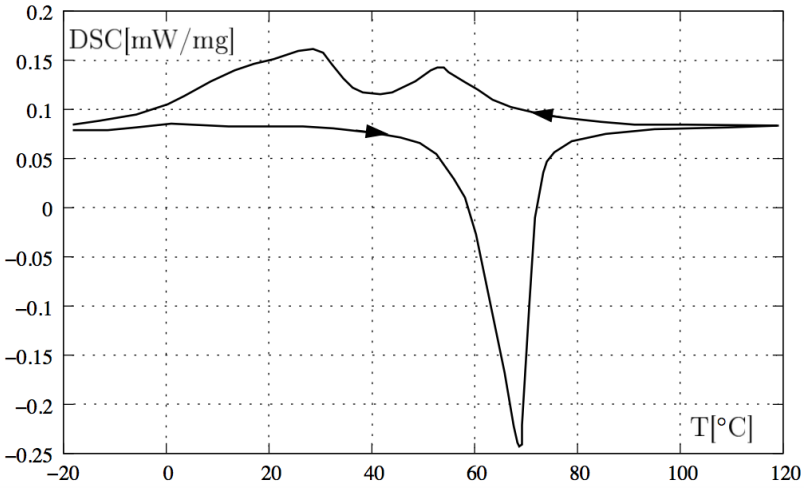

Figure 3.8: DSC analysis (from [32]) .

The obtained DSC curve exhibits a single-step endothermic $M \rightarrow A$ transition upon heating and an exothermic $A \rightarrow M$ transition upon cooling. By considering the $M \rightarrow A$ transition, due to the presence of its high peak, one can determine the A_s and A_f transformation temperatures, with values of about 40°C and 70°C, respectively.

With the aid of *PlotDigitizer App*, the DSC curve values (in mW/mg) from 39,9°C to 90°C, which was the temperature range comprising both martensite and austenite phases in the endothermic transition (driven by heating), were extracted (see Figure 3.9).

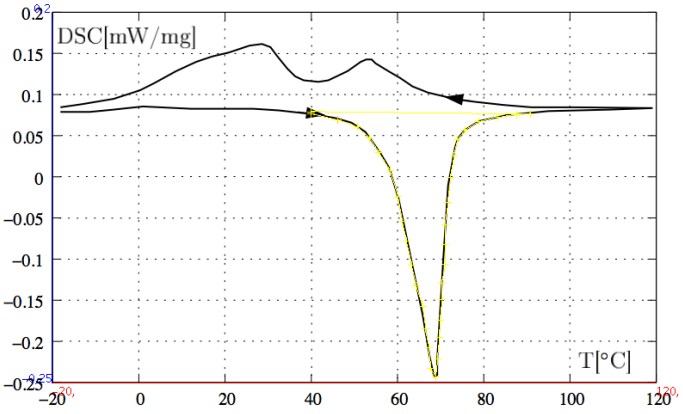

(a) Heat Flux - PlotDigitizer analisys.

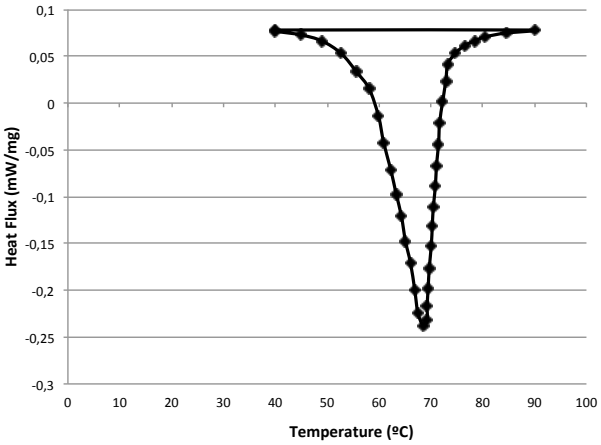

(b) Heat Flux [mW/mg].

Figure 3.9: Extraction of the Heat Flux values from the DSC curve.

According to the assumptions of chapter 2.4.2 and [47], the degree of transformation can be determined from the enthalpy of the system, expressed by the area of the DSC graphic peak. From equation (2.1) the following baseline-corrected and unsmeared DSC curve, was obtained:

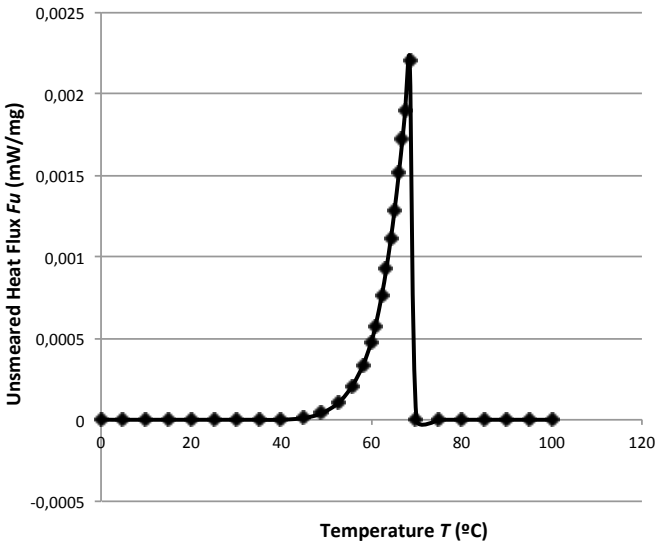

Figure 3.10: Unsmeared Heat Flux of the $M \rightarrow A$ transformation.

Considering the previous curve and applying the equation (2.2), one can obtain a representative curve of the austenite phase fraction *f(T)* as function of temperature.

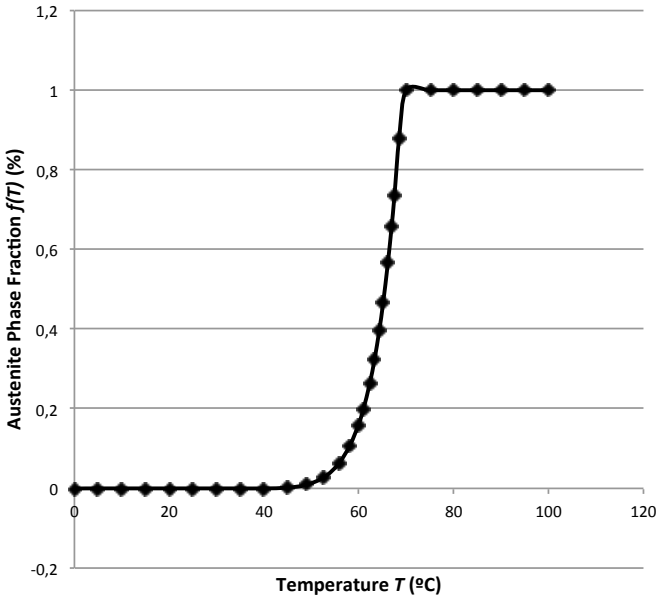

Figure 3.11: Austenite phase fraction evolution during the $M \rightarrow A$ transformation.

It is noteworthy that the A_s and A_f transformation temperatures stand around 40°C and 70°C respectively, just like it was presumed in the DSC run graphic.

Taking into account the SMA kinetic model developed by Nikolay Zotov, Vladimir Marzynkevitsch and Eric J. Mittemeijer [47], equation (2.3) was used to describe Figure's 3.11 data.

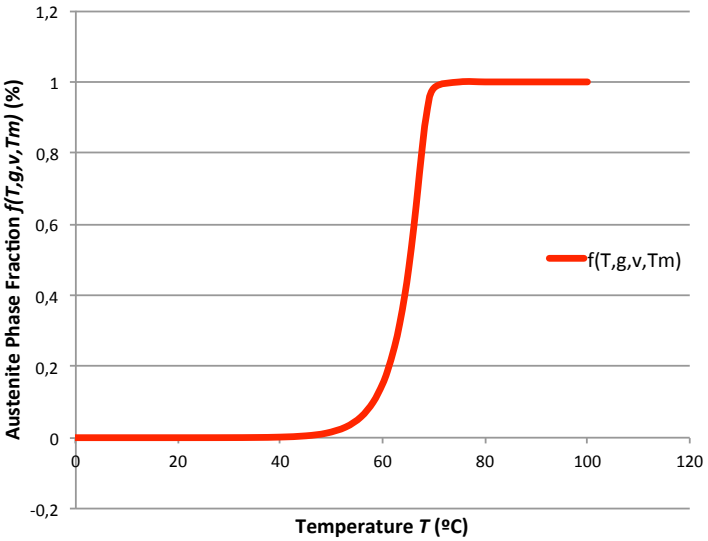

Figure 3.12: Austenite phase fraction - Equation (2.3), $f(T, g, \nu, T_m)$.

Table 3.3: Equation (2.3) fitting parameters.

Fit parameters		
g	ν	T_m
0.225	6	68.36

The g and ν fitting parameters used in the equation (2.3) were chosen considering the studies of [47], with the purpose of approximating the equation (2.3) to the behavior reported in the graphic of Figure 3.11. Regarding the T_m fitting parameter, it was obtained by interpolation between the temperatures corresponding to the maximum transformation rate $(df/dT)_{\max}$, (see Figure C.4 of Appendix C).

In order to verify the suitability of equation (2.3) (see Figure 3.12) to express the data of the Figure 3.11, a graphical overlay, represented in the Figure 3.13, was performed. It is possible to conclude that the kinetic equation (2.3) describes very well the data obtained from the DSC run.

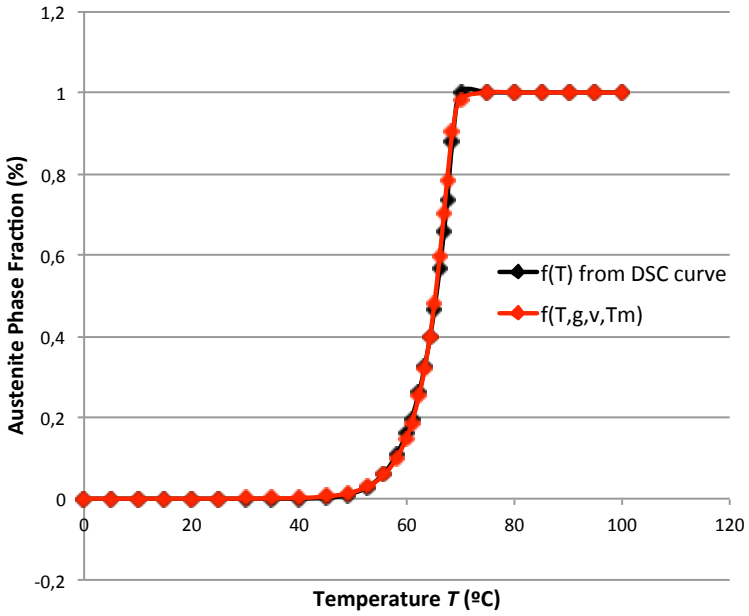

Figure 3.13: Suitability of equation (2.3) to the graphical data of Figure 3.11.

3.4.2 Mechanical law

To complete the SMA constitutive model, it is necessary to define the mechanical law that relates stress (σ) and strain (ε), in order to obtain the elasticity modulus (E). The martensite phase fraction (ξ) is an internal state variable representing the transformation in the material. It is complementary to the austenite phase fraction ($f(T)$) and can be mathematically represented as $\xi = 1 - f(T)$.

Both the two mechanical laws (Voight scheme and Reuss scheme), mentioned in Section 2.4.3, were used to simulate the behavior of the modulus of elasticity of the SMA wire sample.

Considering the experimental results from Section 3.3.3, the E_M and E_A values were established in accordance with the obtained maximum and minimum values of the modulus of elasticity. $E_M = 34\,GPa$ and $E_A = 65\,GPa$.

- *Voight scheme*

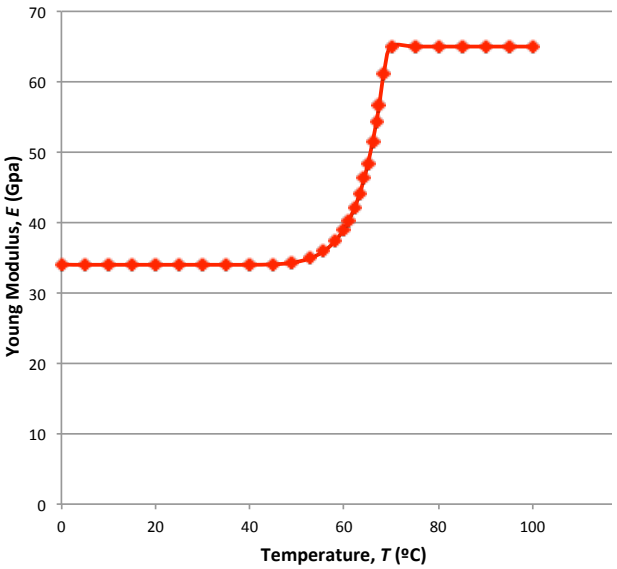

Figure 3.14: Voight scheme - Modulus of elasticity as function of temperature.

- *Reuss scheme*

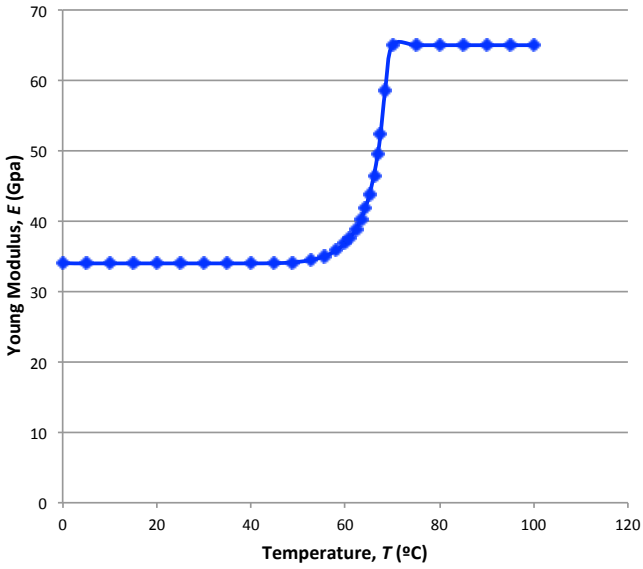

Figure 3.15: Reuss scheme - Modulus of elasticity as function of temperature.

The graphics in Figures 3.14 and 3.15 report the evolution of E according to the stress (σ), strain (ε), temperature (T) and martensite phase fraction (ξ), according to the Voight and Reuss schemes, respectively.

For a more detailed analysis, all the numerical data used in this approach is described in the appendix C of this document.

3.5 Experimental approach Vs. Numerical approach - Young modulus of the SMA wire

Both experimental and theoretical means have been used in the literature to obtain the relevant characteristics of SMAs.

In this section, all the models defining the modulus of elasticity as function of temperature are plotted in a single graphic, to compare all the obtained results.

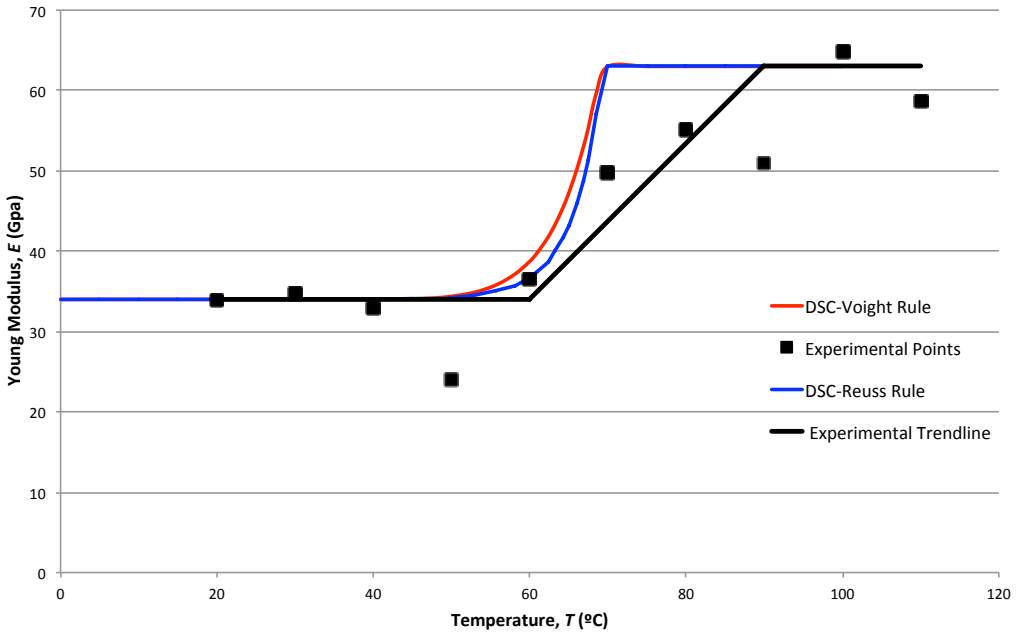

Figure 3.16: Experimental approach Vs. Numerical approach - Young modulus of the SMA wire.

Observing the graphic in Figure 3.16, it is possible to draw some important conclusions. Despite the similar behaviors presented by all curves, it is possible to observe certain differences, mainly between the experimental and the numerical approach.

The key difference observed in Figure's 3.16 graphic, is reflected in the beginning of the austenitic baseline, where one can verify that in the numerical approach (Voight and Reuss schemes) the A_f value rounds $A_f \pm 70^oC$, while in the experimental approach the A_f value is higher, rounding $A_f \pm 80^oC$.

The above-mentioned point turns out to be mitigated, due to the fact that the data obtained through the experimental approach, yields a scattering graphic, where the results are described by single points. The non consideration of a variable stress in the numerical model approach, may be a cause for the slightly different behavior between the results of both approaches.

Either way, even with the constraints of the experimental test, the results of the Young modulus mapping were considered acceptable. As the Reuss model curve is the one that best suits the experimental data, the results established by this model will be subsequently used in the course of this document.

Chapter 4

Vibration Control Systems - Adaptive Tuned Mass Damper

4.1 Introduction

Vibration control systems are a set of technical means with the objective of mitigating vibrational impacts in structures.

Nowadays, a large survey is being conducted at the level of vibration control in civil engineering structures. Several types of vibration control systems have been studied and appear in the literature ([24] [44]) organized according to their way of action, being therefore, divided into active, passive or hybrid systems.

Active control systems comprise real-time actions with input signal processing equipment and actuators employing large amounts of energy. On the other hand, passive control systems have no feedback capability, applying a suitable control only for the considered situation. Hybrid control systems combine features of both active and passive control systems.

This dissertation focuses the application of a hybrid control system composed by an adaptive tuned mass damper (ATMD) with specific features. To do so, the present chapter describes the implementation of the two following vibration control systems:

- The Undamped Dynamic Vibration Absorber.
- The Damped Dynamic Vibration Absorber.

Initially, those two types of control systems are presented and their operational and theoretical basis are explained, according to the studies of Den Hartog [12].

Afterwards, both control systems are compared in order to highlight their main differences and key features.

4.2 The Undamped Dynamic Vibration Absorber - Vibration Suppressor

Any ordinary structure, subjected to a steady alternating force of constant frequency may suffer obnoxious vibrations, especially when the excitation frequency is close to the natural frequency of the structure, causing resonance problems. In order to prevent this situation, one should consider the possibility of removing the force or changing the structure's characteristics, namely the mass and/or the stiffness. Unfortunately, in the majority of the cases, both of two options previously referred are impractical [12]. The third possibility relies in the application of a control system in the structure.

In this section, the Undamped Dynamic Vibration Absorber (Vibration Suppressor) is the control system in concern.

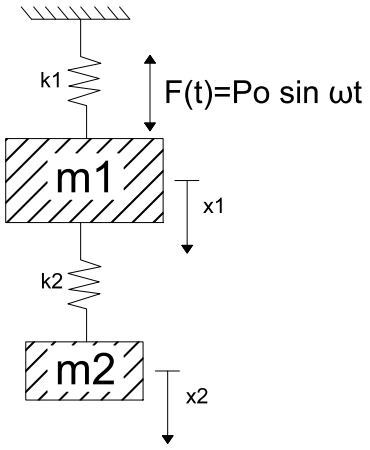

Figure 4.1: Main System and the Undamped Dynamic Vibration Absorber.

The vibration Suppressor of Figure 4.1 consists in a secondary smaller vibratory system (k_2, m_2) attached to the main mass (m_1) of the primary system that is under the effect of a sinusoidal force $F(t) = P_o \sin \omega t$. The main goal is to tune the vibration suppressor with the acting force by choosing a natural frequency for the secondary system ($\omega_2 = \sqrt{\frac{k_2}{m_2}}$) equal to the frequency ω of the acting force. Consequently, the secondary system will vibrate in such way that its spring force is equal and opposite to the one applied in the main system ($F(t) = P_o \sin \omega t$), making both forces cancel each other and then the main mass does not vibrate at all.

In order to demonstrate the operation of the vibration suppressor, one obtains the following equations of motion.

From the dynamic equilibrium equation:

$$F(t) = m\,\ddot{x} + c\,\dot{x} + k\,x \tag{4.1}$$

For the main and secondary system, one obtains respectively:

$$m_1\,\ddot{x_1} + (k_1 + k_2)\,x_1 - k_2\,x_2 = P_0 \sin \omega t \tag{4.2}$$

$$m_2\,\ddot{x_2} + k_2(x_2 - x_1) = 0 \tag{4.3}$$

The forced vibration of the system will be of the form:

$$\begin{cases} x_1 = X_1 \sin \omega\, t \\ x_2 = X_2 \sin \omega\, t \end{cases} \tag{4.4}$$

Replacing these two expressions in equations of motion (4.2) and (4.3), using two differentiations (in order to the variable t) and dividing both by $\sin \omega\, t$, one obtains:

$$X_1(-m_1\,\omega^2 + k_1 + k_2) - k_2\, X_2 = P_0 \tag{4.5}$$

$$-k_2\, X_1 + X_2(-m_2\,\omega^2 + k_2) = 0 \tag{4.6}$$

According to Den Hartog [12] and taking into account the following relations:

- $X_{st} = \frac{P_0}{k_1}$, Static deflection of the main system;
- $\omega_2^2 = \frac{k_2}{m_2}$, Natural frequency of the absorber;
- $\omega_1^2 = \frac{k_1}{m_1}$, Natural frequency of the main system;

soving for X_1 and X_2,

$$\frac{X_1}{X_{st}} = \frac{1 - \frac{\omega^2}{\omega_2^2}}{\left(1 - \frac{\omega^2}{\omega_2^2}\right)\left(1 + \frac{k_2}{k_1} - \frac{\omega^2}{\omega_1^2}\right) - \frac{k_2}{k_1}} \tag{4.7}$$

$$\frac{X_2}{X_{st}} = \frac{1}{\left(1 - \frac{\omega^2}{\omega_2^2}\right)\left(1 + \frac{k_2}{k_1} - \frac{\omega^2}{\omega_1^2}\right) - \frac{k_2}{k_1}} \tag{4.8}$$

Through the equation (4.7) (main system), when the frequency of excitation (ω) equals the natural frequency of the absorber (ω_2), the numerator $(1 - \frac{\omega^2}{\omega_2^2})$ becomes equal to zero and consequently the amplitude (X_1) of the main mass becomes also zero. For the same situation ($\omega = \omega_2$), in equation (4.8) (Suppressor), the amplitude (X_2) of the Suppressor is reduced to:

$$X_2 = -\frac{k_1}{k_2}\, X_{st} = -\frac{P_0}{k_2}$$

These relations are true for any value of $\frac{\omega}{\omega_1}$ and thus, the initially proposed statement is proved.

Now, considering,

$$\omega_2 = \omega_1 \quad \text{and} \quad \frac{k_2}{m_2} = \frac{k_1}{m_1} \text{ or } \frac{k_2}{k_1} = \frac{m_2}{m_1}$$

one defines,

- $\mu = \frac{m_2}{m_1}$, as the mass ratio between the two masses.

And the amplification factor regarding μ is defined:

$$\frac{X_1}{X_{st}} = \frac{1 - \frac{\omega^2}{\omega_2^2}}{\left(1 - \frac{\omega^2}{\omega_2^2}\right)\left(1 + \mu - \frac{\omega^2}{\omega_2^2}\right) - \mu} \tag{4.9}$$

$$\frac{X_2}{X_{st}} = \frac{1}{\left(1-\frac{\omega^2}{\omega_2^2}\right)\left(1+\mu-\frac{\omega^2}{\omega_2^2}\right)-\mu} \tag{4.10}$$

With the introduction of this control system, the structure now comprises two new natural frequencies of vibration, which both differ from the initial natural frequency of the structure without the control system (see Figure 4.2).

Those new natural frequencies are determined by setting the denominators equal to zero:

$$\begin{gathered}\left(1-\frac{\omega^2}{\omega_2^2}\right)\left(1+\mu-\frac{\omega^2}{\omega_2^2}\right)-\mu=0 \Leftrightarrow \\ \Leftrightarrow \left(\frac{\omega}{\omega_2}\right)^2 = \left(1+\frac{\mu}{2}\right) \pm \sqrt{\mu+\frac{\mu^2}{4}}\end{gathered} \tag{4.11}$$

According to equation (4.9) and considering an approximately 5% mass ratio (μ), one obtains the following graphical representation of the structure's amplification factor regarding a chosen frequency range.

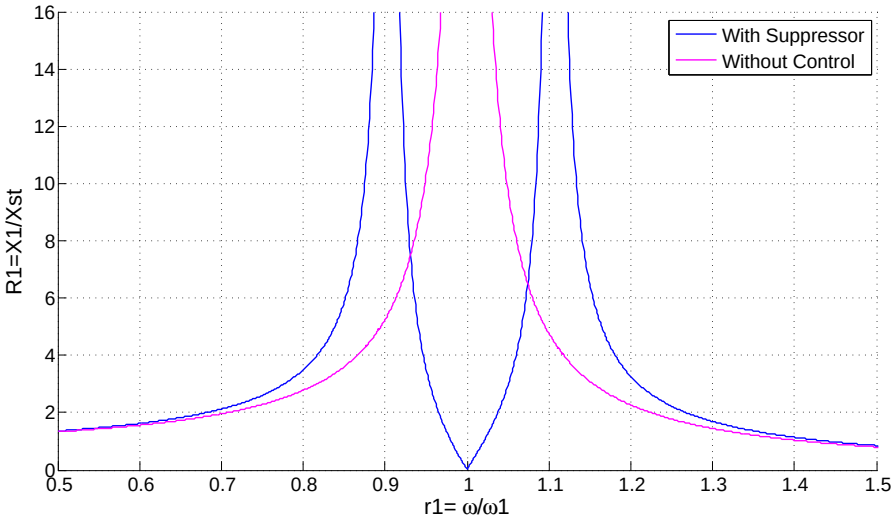

Figure 4.2: Amplitude of the main system motion with and without Suppressor.

As shown in Figure 4.2, with the introduction of the vibration suppressor in the system, the structure will now have two fundamental frequencies instead of one. One of the frequencies will be inferior and the other one will be superior to the original natural frequency of the structure.

In the previous graphic is, once again, possible to observe that for $\omega = \omega_2 = \omega_1$, the amplitude (X_1) of the main mass becomes zero.

Finally, in order to correctly design the vibration suppressor, it is necessary to ensure that its natural frequency equals the frequency of the applied force.

$$\omega = \omega_2 = \sqrt{\frac{k_2}{m_2}} \tag{4.12}$$

4.3 The Damped Vibration Absorber - Tuned Mass Damper (TMD)

Unlike the Suppressor, the introduction of a TMD in the structure does not allow for the complete attenuation of structural vibrations. In fact, a TMD only allows for a reduction of the vibrations up to a given value, but for a wider range of frequencies than the Suppressor, yielding a better efficiency.

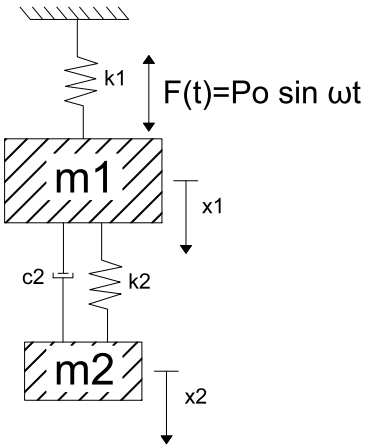

Figure 4.3: Main System and the Damped Vibration Absorber.

If an additional damper is added to the system presented in Figure 4.1, one obtains the system designed in Figure 4.3, representative of a TMD implementation.

Applying the Newton's first law to the mass m_1, one obtains the equations of motion for the main and secondary system respectively,

$$m_1\,\ddot{x_1} + k_1\,x_1 + k_2\,(x_1 - x_2) + c_2\,(\dot{x_1} - \dot{x_2}) = P_0\,\sin\omega\,t \tag{4.13}$$

$$m_2\,\ddot{x_2} + k_2(x_2 - x_1) + c_2\,(\dot{x_2} - \dot{x_1}) = 0 \tag{4.14}$$

According to [15], and taking into account the relations defined by Moutinho [24],

- $r_1 = \frac{\omega}{\omega_1}$, ratio between the excitation frequency and the frequency of the system;
- $q = \frac{\omega_2}{\omega_1}$, ratio between the TMD frequency and the frequency of the system;
- $\mu = \frac{m_2}{m_1}$, as the mass ratio between the two masses;
- $X_{st} = \frac{P_0}{k_1}$, Static deflection of the main system;
- $\zeta_2 = \frac{c_2}{2\sqrt{k_2 m_2}}$, TMD damping ratio.

the amplitudes of the standing motion of the mass m_1 and m_2 are respectively given by:

$$\frac{X_1}{X_{st}} = \sqrt{\frac{(2\zeta_2 r_1 q)^2 + (r_1^2 - q^2)^2}{(r_1^4 - [1 + (1+\mu)q^2]r_1^2 + q^2)^2 + (2\zeta_2 r_1 q)^2[1 - r_1^2(1+\mu)]^2}} \tag{4.15}$$

$$\frac{X_2}{X_{st}} = \sqrt{\frac{q^4 + (2\zeta_2 q)^2}{(r_1^4 - [1 + (1+\mu)q^2]r_1^2 + q^2)^2 + (2\zeta_2 r_1 q)^2[1 - r_1^2(1+\mu)]^2}} \tag{4.16}$$

Considering once again an approximately 5% mass ratio (μ), according to equation (4.15) one obtains the graphical representation of the structure's amplification factor, presented in Figure 4.4.

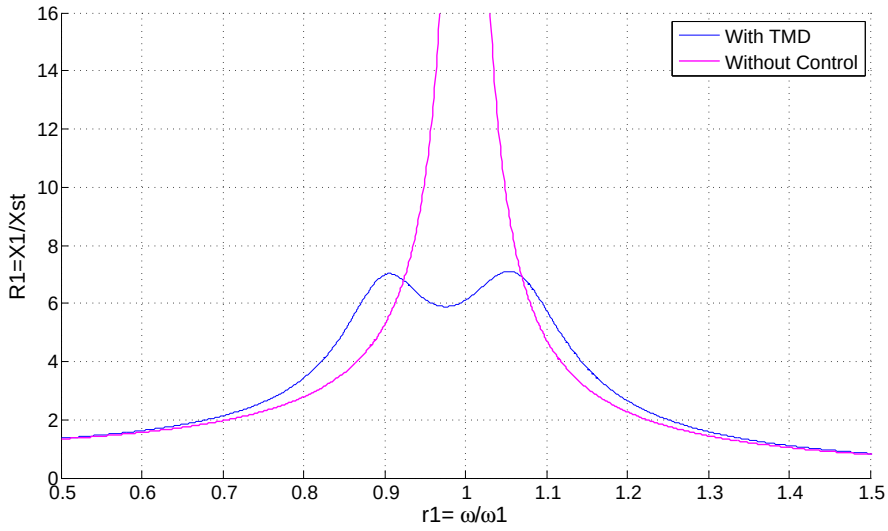

Figure 4.4: Amplitude of the main system motion with and without TMD.

As in the vibration suppressor case, with the introduction of the TMD, the structure will also have two fundamental frequencies instead of one, as it is possible to see in Figure 4.4.

Considering ζ_2, q and μ as the key parameters controlling the system's amplification, it is important to note that: ζ_2 is the parameter which controls the maximum amplitude value of the two peaks displayed in the structural response of the main system; q the one that regulates the difference between the maximum value of both peaks of the system's amplification; and μ being the parameter that regulates the gap between those two referred peaks.

Note: For $\zeta_2 = 0$, the system is able to completely eliminate the vibrations when the excitation frequency equals the system frequency, thus representing the aforementioned Suppressor case (see section 4.2).

The structure in which the control system is being applied is characterized by a very low damping ratio ($0 < \zeta < 1\%$) and, therefore, one can calculate the optimal parameters for the TMD, using the solution found by Den Hartog [12].

It is important to note that Den Hartog's solution is based on an imposition that both peaks, regarding the TMD usage (Figure 4.4), present the same displacement amplitude.

- Maximum amplitude of the main system displacement:

$$\frac{X_1}{X_{st}} = \sqrt{1 + \frac{2}{\mu}} \tag{4.17}$$

- Optimal frequency of the TMD:

$$\omega_{2,opt} = \frac{1}{1+\mu}\,\omega_1 = q_{opt} \times \omega_1 \tag{4.18}$$

- Optimum damping ratio of the TMD:

$$\zeta_{2,opt} = \sqrt{\frac{3\mu}{8(1+\mu)^3}} \tag{4.19}$$

- Optimal stiffness of the TMD:

$$k_2 = \omega_{2,opt}^2 \times m_2 \tag{4.20}$$

4.4 Suppressor Vs. TMD

Figure 4.5 exhibits the amplitude of the system's vibratory motion described for a certain range of frequencies according to equations (4.9) and (4.15), where both Suppressor and TMD are correctly tuned for a generic structure.

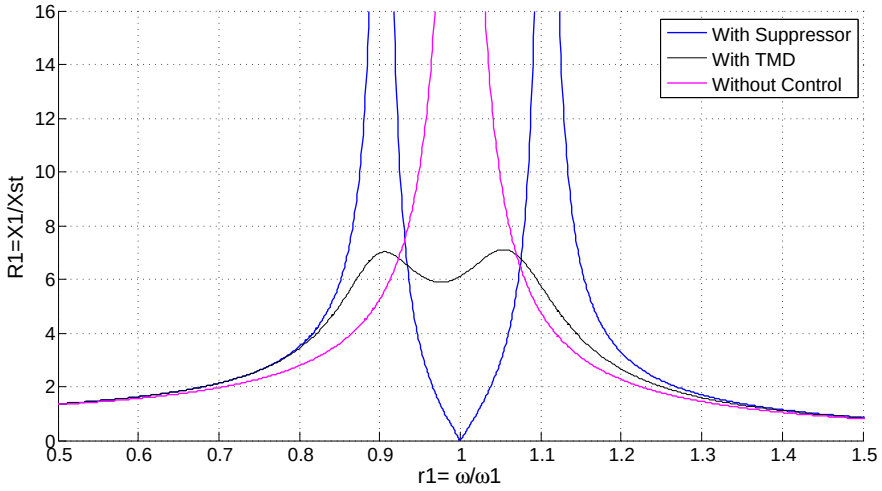

Figure 4.5: Amplitude of the main system motion with Suppressor, with TMD and without control system.

When the Undamped Dynamic Vibration Absorber (Suppressor) is designed for a resonance situation, it completely eliminates the motion of the main mass, becoming in this way the best solution (for frequencies close to the resonance situation). However, this reduction proves to be useful in a very limited frequency range, since in the vicinity of this resonance frequency, the dynamic amplification factor highly increases again.

In the Damped Vibration Absorber (TMD) case, although it does not completely removes the structure's motion for the resonant frequency, it turns out to be very efficient since the reduction of the amplification comprises a larger domain of frequencies, keeping the dynamic amplification factor always below a pre-defined value.

Chapter 5

Implementation of an Adaptive Tuned Mass Damper in a Footbridge

5.1 Introduction

The present chapter describes the implementation of the two previously presented adaptive vibration control systems in a footbridge structure.

Initially, a section with the considered case study is presented. This case study intends to implement the formulations developed on the considered vibration control systems in a real structure.

Afterwards, taking into account the characteristics of the footbridge, a Damped Dynamic Vibration Absorber (TMD) is designed in order to attenuate the amplitude of the vibrations caused by a sinusoidal force acting on structure. This TMD design is built upon the studies carried out by T. Krus [15]. The Undamped Dynamic Vibration Absorber (Suppressor) is also designed to operate in the same structure and also for the same force.

Then, the "spring" component of both aforementioned control systems was characteristically changed, being now composed of a SMA wire. With this, it became possible to develop two new control systems with the ability to modify their stiffness.

Lastly, the operational limits of both control systems are disclosed and new alternatives for their usage, outside the defined operating limits, are presented.

5.2 Case Study - Footbridge

The purpose of this section is to present an overview of the structure studied in this document.

The case study is based on a footbridge built over the Avenida Marechal Gomes da Costa (Figure 5.1), which is an important avenue located in the Lisbon city center, Portugal. This footbridge allows pedestrians to safely cross the aforementioned avenue and it is characterized by lightness attributes, suiting the urban area where it is located.

This structure has been previously studied by T. Krus in [15], and thus, most of the data regarding its operation was obtained from that document.

Figure 5.1: Footbridge over the Avenida Marechal Gomes da Costa, T. Krus, [15].

5.2.1 Footbridge Geometry

The footbridge consists on a simple supported structure that comprises a 30m span establishing the connection between two edge supports with the same altimetric quota. The cross section of the platform is 2,85 m width by 2,80 m height. This footbridge is mainly composed by a steel structure, where both the upper and lower chords are made of metallic profiles of the HEB type. The majority of the other structural elements are also characterized by HEB and IPE metallic profiles.

A simple schematic representation of the footbridge, can be seen in Figure 5.2.

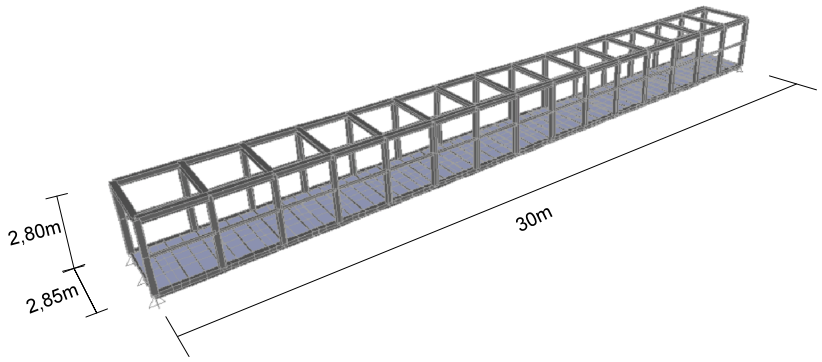

Figure 5.2: Three dimensional view of the footbridge model, T. Krus, [15].

5.2.2 Dynamic behavior

In order to obtain an appropriate dynamic design of this case study footbridge, it was necessary to correctly estimate its damping coefficient. This coefficient essentially depends on the type of materials and structural connections used. According to [20], Table 5.1 displays the typical values of the equivalent viscous damping ratio ζ for footbridges under the pedestrian action.

Table 5.1: Common values of damping ratio ζ for footbridges, [20].

	Damping ratio (ζ)		
Construction Type	min.	mean	max.
Reinforced concrete	0.008	0.013	0.020
Prestressed concrete	0.005	0.010	0.017
Composite	0.003	0.006	-
Steel	0.002	0.004	-

Based on Table 5.1 one considered a damping ratio of $\zeta = 0,002$ (0,2%), and performed a modal analysis of the structure.From here, the author of [15], obtained the structure's eigenvalues, eigenvectors and also its natural frequencies and vibration modes.

Figure 5.3 represents the configuration of the first vertical vibration mode of the structure, which is the one taken into account throughout the development of this thesis.

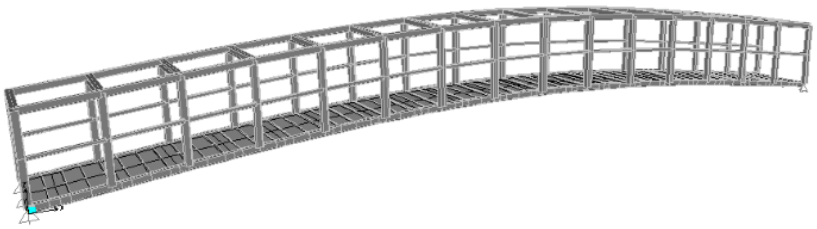

Figure 5.3: Configuration of the 2^{nd} vibration mode of the structure - 1^{st} vertical vibration mode: f=3,46 Hz - T. Krus, [15].

5.2.3 Dynamic Actions and Structural Response

In the majority of the cases, vibration problems in footbridges are caused by a forced motion imposed by the stepping rate of pedestrians. According to [20], the average walking rate of pedestrians is near 2 Hz with a standard deviation of 0,175 Hz, meaning that more or less 95% of pedestrians walk at rates between 1,65 Hz and 2,35 Hz. In some cases, running pedestrians with a walking rate over 3,5 Hz also need to be considered.

In order to study these types of actions, footbridges are often modeled as equivalent Single Degree of Freedom (SDOF) Systems [20].

According to the studies carried out by T. Krus [15], in order to evaluate the effect of a pedestrian crowd walking on the bridge, a simplified loading model - Sétra Model - was considered. Based on this model, this structure was classified as a Class I footbridge (urban bridge connecting areas of high pedestrian density or frequently used by dense crowds, subjected to a high pedestrian traffic), comprising an average density of 1 pedestrian/m^2

Table 5.2 describes the calculation of the distributed loads regarding the pedestrians mass, according to the Sétra Model [35].

Table 5.2: Distributed loads regarding the pedestrians mass, [15]

Footbridge class	Pedestrian density (d) [pedestrians/m^2]	Effective area (S) [m^2]	Total number of pedestrians (N=S·d)	Equivalent number of pedestrians ($N_{eq} = 1,85\sqrt{N}$)	Pedestrians total weight [kN]	Distributed load [kN/m]
Class I	1	2,4 · 30	72	15,7	50,4	1,68

Once the loading is applied in accordance with the pedestrian traffic class, the new natural frequency of the structure is obtained and presented in Table 5.3.

Table 5.3: Natural frequency of the structure.

Vibration mode	Mode type	Natural frequency [Hz]
2	1^{st} Vertical	3,03

Taking into account the natural vibration frequency obtained for 1^{st} vertical mode of the structure, one considered the following load case.

Table 5.4, adapted from [15], describes the implementation of the distributed loads corresponding to the dynamic component of the pedestrians action. The load application process is a dynamic one (time dependent) and it is represented by a time-history force function.

Table 5.4: Time-history force function for the 1^{st} Vertical mode of a Class I footbridge, considering the Sétra Model [35].

Vibration mode	Mode type	Footbridge class	Distributed load function	Distributed max. load [N/m]	Time-history force function
2	1^{st} Vertical	Class I	$70 \cdot N_{eq} \cdot \psi$ / L $\cdot \cos(2 \cdot \pi \cdot f \cdot t)$	18,7	$18,7 \cdot \cos(2 \cdot \pi \cdot 3,03 \cdot t)$

The ψ coefficient, is presented as a reduction coefficient of the action, depending on the frequency range in concern and it was defined as $\psi = 0,51$ for this case study, by T. Krus [15].

Once again according to T. Krus studies, the footbridge in concern suffers from vibration problems, overcoming the vertical acceleration limits. Hence, one concludes that it is necessary to implement a vibration control system to improve its behavior.

5.3 Implementation of the Vibration Control System to the Case Study

5.3.1 Design of a TMD with constant stiffness - Case Study

In order to summarize the studies conducted by T. Krus [15], which carried out the design of a passive control solution for the footbridge referred in section 5.2, some of the main features described in [15] are presented in this section.

Regarding the theoretical design of a TMD system cited in section 4.3, one should note that it is based on a simple two degrees of freedom system.

Considering that the footbridge structure is composed by multiple degrees of freedom, to be able to use the formulation of section 4.3, is necessary to condense all those DOF in a single degree of freedom system with a similar dynamic behavior to the original structure.

If one solely considers the vertical vibration modes of the structure, the design of the vibration control system has to be performed for the most influential one: Mode 2 which is the first vertical mode, with a frequency of 3,03 Hz.

Analyzing the structure's deformed shape for the vibration mode in concern, the point of maximum displacement, regarding the undeformed shape, indicates the optimal location of the control device.

According to T. Krus [15], performing a modal analysis of the structure using the SAP2000 software, the maximum modal component value (β_2) and the structure's modal mass (m_1) for the vibration mode in concern (2^o mode) were obtained:

$$\beta_2 = 0,306 \quad , \quad m_1 = 10,68\,ton$$

Knowing that the Eurocode 0, EN - 1990 limits the vertical acceleration of the pedestrian bridge to a limiting value of:

$$a_{\max} \leq 0,7\mathrm{m/s^2}$$

The maximum displacement of the structure, which limits the vertical acceleration to the above mentioned value, is calculated:

$$X_1 = \frac{a_{\max}}{\omega_n^2} = \frac{0,7}{(3,03 \times 2\pi)^2} = 0,001944\,\mathrm{m} \tag{5.1}$$

Taking into account the time history function $F(t) = 18,7\cos(3,03 \cdot 2\pi \cdot t)$ (Sinusoidal force) representative of the applied force that stimulates the first vertical vibration mode of the structure, T. Krus [15] obtained the structure's static displacement:

$$X_{st} = 0,000276\,\mathrm{m} \tag{5.2}$$

and the maximum dynamic amplification factor:

$$\frac{X_1}{X_{st}} = \frac{0,001944}{0,000276} = 7,04 \tag{5.3}$$

Knowing the maximum value of the dynamic amplification factor, the optimal parameters of the TMD are determined in accordance with the relations defined in section 4.3 (Equations (4.17) (4.18) (4.19)).

$$\frac{X_1}{X_{st}} = \sqrt{1+\frac{2}{\mu}} \quad \Leftrightarrow \quad \mu = 0,0411 \tag{5.4}$$

$$\omega_{2,opt} = \frac{1}{1+\mu}\,\omega_1 = \frac{1}{1+0,0411}\,(3,03\cdot 2\pi) = 18,285 rad/s \tag{5.5}$$

$$\zeta_{2,opt} = \sqrt{\frac{3\mu}{8(1+\mu)^3}} = 0,0117 \tag{5.6}$$

Thereby, the optimal parameters of TMD are obtained:

$$m_2 = \mu \cdot m_1 = 0,0411 \cdot 10,68 = 0,440\text{ton} \tag{5.7}$$

$$k_2 = \omega_{2,opt}^2 \times m_2 = 18,285^2 \cdot 0,440 = 147,1 \text{ kN/m} \tag{5.8}$$

$$c_2 = 2 \cdot \zeta_{2,opt} \cdot \sqrt{k_2 \cdot m_2} = 2 \cdot 0,0117 \cdot \sqrt{147,1 \cdot 0,440} = 1,88 \text{ kN.s/m} \tag{5.9}$$

Table 5.5 summarizes the main features of the designed TMD to be installed in the footbridge structure.

Table 5.5: Optimal parameters of the vertical TMD.

Vibration Mode	Vertical Acceleration Limit (m/s^2)	μ	q_{opt}	$\omega_{2,opt}$ (rad/s)	m_2 (ton)	k_2 (kN/m)	c_2 (kN.s/m)
1^{st} vertical	0.7	0.0411	0.96	18.285	0.440	147.1	1.88

5.3.2 Design of a Vibration Suppressor with constant stiffness - Case Study

To design the Suppressor implemented in the footbridge case study, the majority of the choices that conditioned the TMD design (in section 5.3.1), were taken into account. The Suppressor was also dimensioned considering the same type of disturbance force and the same vibrational mode (2^{nd}vibrational mode of the structure corresponding to the 1^{st}vertical mode).

Aiming to use the same parameters previously defined for the TMD, the Supressor's mass ratio was also set to $\mu = 0,0411$.

Considering,

$$\omega_2 = \omega_1 \quad \text{and} \quad \tfrac{k_2}{m_2} = \tfrac{k_1}{m_1} \text{ or } \tfrac{k_2}{k_1} = \tfrac{m_2}{m_1}$$

as a fundamental principle and knowing that $F(t) = 18,7\cos(3,03\cdot 2\pi\cdot t)$, the stiffness of the Suppressor's "spring" is obtained through equation (4.12):

$$k_2 = \omega^2 \times m_2 = (3,03\cdot 2\pi)^2 \cdot 0,440 = 159,477 \text{ kN.s/m} \tag{5.10}$$

According to equation (4.11) the two new natural frequencies of the structure are defined by the ratio between the excitation frequency and the natural frequency of the whole system,

$$\begin{cases} \left(\frac{\omega}{\omega_2}\right) = 0,90 \\ \left(\frac{\omega}{\omega_2}\right) = 1,11 \end{cases} \tag{5.11}$$

and these values correspond to the vertical asymptotes of the graphic in Figure 4.2.

Table 5.6 summarizes the main features of the designed Suppressor to be installed in the footbridge structure.

Table 5.6: Optimal parameters of the vertical suppressor.

Vibration Mode	μ	ω_2 (rad/s)	m_2 (ton)	k_2 (kN/m)
1^{st} vertical	0.0411	19.038	0.440	159.477

5.4 Design of SMA Wires - Control System "spring"

The SMA cables used in the control systems, provide them with the "variable stiffness" factor and consequently increase their performance. The SMA wire design follows the specifications described in [29], and the tests were performed considering a dynamic system comprising a $m_2 = 440$ kg mass which represents the vibration controller.

According to *FLEXINOL* ® and the assumptions mentioned in chapter 3.2, one can define $\sigma = 103$ MPa as the maximum stress that the wire is capable of withstanding, in order to ensure a proper cyclic behavior.

1. *Choice of wire diameter* - The wire diameter and cross sectional area are based on the maximum allowable stress of 103 MPa. Then, the required cross sectional area for a load of 4312 N yields:

$$A = \frac{F}{\sigma_{\max}} = \frac{4312}{103} = 41,86 \text{ mm}^2 \tag{5.12}$$

$$d = \sqrt{\frac{4A}{\pi}} = 7,30 \text{ mm} \tag{5.13}$$

2. *Choice of wire length* - In order to achieve stiffness values in both martensitic and austenitic phase, comprising a range of values where the optimum stiffness of the vibration controller is located, a 15m length wire was adopted. *i.e.* In the TMD case, for a natural frequency of the structure of 3,03 Hz, a stiffness of 147,1 kN/m is required for the SMA wire ("spring"). In the vibration suppressor case, for the same natural frequency of the structure, a stiffness of 159,477 kN/m is required for the SMA wire.

   Considering the mapping of the modulus of elasticity as function of temperature defined in chapter 3 (with respect to Reuss scheme), one was able to predict the SMA wire behavior during heating. In order to increase the interval where the SMA wire is able to change its stiffness, the E_M and E_A limit values were defined according to the ones set in the *FLEXINOL* ® protocol.

Then, with a length of 15m and considering $E_M = 40$ GPa, $E_A = 83$ GPa in a first stage, the following values of stiffness were obtained:

$$K_M = \frac{E_M\, A}{L} = 111,64 \text{ kN/m} \tag{5.14}$$

$$K_A = \frac{E_A\, A}{L} = 231,65 \text{ kN/m} \tag{5.15}$$

Thus, it's possible to to check that,

For the TMD: $\underbrace{111,64}_{K_M} < \underbrace{147,1}_{K_{\text{optm}}} < \underbrace{231,65}_{K_A}$ kN/m

For the Suppressor: $\underbrace{111,64}_{K_M} < \underbrace{159,477}_{K_{\text{optm}}} < \underbrace{231,65}_{K_A}$ kN/m

Knowing that the stiffness values for the SMA cable also depend on the wire's length, one had to study this measurement according to the strain that can occur in both phases. The two distinct types of effects capable of producing length variations in the SMA cable (and consequently in its stiffness), are subsequently presented.

($E_M = 40$ GPa, $E_A = 83$ GPa, $A = 41,86$ mm^2, $F = 4312$ N)

- Stress influence in the wire's strain/stiffness:
  Considering stress as the factor producing wire length variations, the strains in both high and low temperature phases were studied:

$$\varepsilon_M = \frac{F}{E_M\, A} = 0,2575\% \tag{5.16}$$

$$\varepsilon_A = \frac{F}{E_A\, A} = 0,1241\% \tag{5.17}$$

  With those strain values, new wire lengths were obtained for each phase and considering equation (5.14) and (5.15) the following stiffness values were achieved:

$$K_M = 111,35 \text{ kN/m}$$

$$K_A = 231,36 \text{ kN/m}$$

  The following table summarizes the stress influence in the wire's strain/stiffness, providing the final lengths of the wire as well as the error (%) associated with the stiffness variation regarding the values presented in (5.14) and (5.15).

Table 5.7: Stress influence in the wire's strain/stiffness

Strain		**Length**		**Stiffness**		**"error" (%)**	
Martensite ε_M (m/m)	Austenite ε_A (m/m)	Martensite $L+\varepsilon_M$ (m)	Austenite $L+\varepsilon_A$ (m)	Martensite $K(L+\varepsilon_M)$ (kN/m)	Austenite $K(L+\varepsilon_A)$ (kN/m)	Martensite ΔK (%)	Austenite ΔK (%)
0.002575	0.001241	15.0386	15.0186	111.3508	231.3608	-0.2568	-0.1239

Through the previous results one can conclude that in this case, stiffness variations are low enough to not be considered.

- Temperature influence in the wire's strain/stiffness:
  Alternatively, considering the Temperature as the main cause of length variations in the wire, the strains in both high and low temperature phases are recalculated. As in the low temperature phase the heating has not yet occurred, the strain only depends on the stress applied to the wire, remaining equal to the one previously calculated.

$$\varepsilon_M = 0,2575\%$$

According to [29], for a certain length value, there is a corresponding value of stroke that needs to be considered. This stroke value is directly related to the specifications of the wire itself, where for *FLEXINOL* ®, nearly 5% memory strain can be obtained, when the wire is heated through its transformation temperatures.

Once again, one should report the experimental results obtained in chapter 3, where Table 3.1 shows a contraction in the wire's length of 4.44%, when thermoelectrically driven.

$$\varepsilon_A \approx 5\%$$

Then, knowing the strains in both phases and considering a cable with $L = 15m$ a specific stroke (S) value was obtained:

$$S = (\varepsilon_M - \varepsilon_A)\, L = -0,7114 \text{ m} \tag{5.18}$$

Austenitic wire length can be easily obtained by subtracting the stroke to the Martensitic length. The following table summarizes the Temperature influence in the wire's strain/stiffness, providing the final lengths of the wire as well as the error (%) associated with the stiffness variation, regarding the values presented in (5.3) and (5.4).

Table 5.8: Temperature influence in the wire's strain/stiffness

Strain		**Length**		**Stiffness**		**"error" (%)**	
Martensite ε_M (m/m)	Austenite ε_A (m/m)	Martensite $L+\varepsilon_M$ (m)	Austenite $L+\varepsilon_A$ (m)	Martensite $K(L+\varepsilon_M)$ (kN/m)	Austenite $K(L+\varepsilon_A)$ (kN/m)	Martensite ΔK (%)	Austenite ΔK (%)
0.002575	0.05	15.0386	14.3273	111.3508	242.5251	-0.2568	4.6956

As it can be seen in the table above, the error (%) obtained for stiffness in the austenitic phase is now considerable (4.6956%). Therefore, one can conclude that it is necessary to take into account the wire shortening effect caused by temperature, achieving new length and stiffness values for both phases.

Hence, from Table 5.8,

$$\underbrace{111,35}_{K_M} < K^{\text{wire}} < \underbrace{242,53}_{K_A} \text{ kN/m} \tag{5.19}$$

are considered the stiffness limit values for the SMA cable.

Taking into account the assumptions defined in this section and the studies carried out in chapter 3, the SMA wire stiffness-temperature mapping is presented in the appendix D of this dissertation.

5.5 SMA Wire Operating Limits - Control systems with variable stiffness

In accordance with the above seen, SMA wires are characterized by having stiffness boundaries associated with both the austenitic and martensitic phases. Thus, the vibration control devices, where the SMA wires are implemented, will also be subjected to certain operating limits when changing their stiffness according to a specific vibration.

5.5.1 Suppressor with Variable Stiffness

The stiffness values referred in the previous section were considered to determine the range of frequencies for which the Suppressor is able to operate within. Regarding the operation principle of the Suppressor, the minimum and maximum operating frequency values are obtained, considering the stiffness values mentioned in eq. (5.19):

$$\omega = \sqrt{\frac{k}{m}} \text{ (rad/s)} \tag{5.20}$$

$$f = \frac{\omega}{2\pi} \text{ (Hz)} \tag{5.21}$$

- Minimun operating frequency: (Martensite Phase)

$$\begin{aligned} K_M = 111,35 \text{ kN/m} \rightarrow \omega = \sqrt{\frac{111,35}{440 \times 10^{-3}}} = 15,9082 \text{ (rad/s)} \rightarrow \\ \rightarrow f = \frac{15,9082}{2\pi} = 2,5319 \text{ (Hz)} \end{aligned} \tag{5.22}$$

- Maximun operating frequency: (Austenite Phase)

$$\begin{aligned} K_A = 242,53 \text{ kN/m} \rightarrow \omega = \sqrt{\frac{242,53}{440 \times 10^{-3}}} = 23,4775 \text{ (rad/s)} \rightarrow \\ \rightarrow f = \frac{23,4775}{2\pi} = 3,7366 \text{ (Hz)} \end{aligned} \tag{5.23}$$

For the sake of simplicity, the following approximations have been considered.

- Minimun operating frequency: (Martensite Phase)

$$f = 2,5319 \simeq 2,54 \text{ Hz} \tag{5.24}$$

- Maximun operating frequency: (Austenite Phase)

$$f = 3,7366 \simeq 3,73 \text{ Hz} \tag{5.25}$$

Finally, with the limit frequencies defined, the definitive stiffness values for the Suppressor are obtained:

$$f = 2,54 \text{ Hz} \rightarrow K_M = 112,07 \text{ kN/m} \tag{5.26}$$

$$f = 3,73 \text{ Hz} \rightarrow K_A = 241,67 \text{ kN/m} \tag{5.27}$$

Dividing the limit frequencies earlier defined, by the value of the structure's natural frequency (3,03 Hz), one obtains the Suppressor operating boundaries.

$$\text{Max. operating limit:} \quad r_1 = \frac{\omega}{\omega_1} = \frac{2,54 \times 2\pi}{3,03 \times 2\pi} = 0,8383 \tag{5.28}$$

$$\text{Min. operating limit:} \quad r_1 = \frac{\omega}{\omega_1} = \frac{3,73 \times 2\pi}{3,03 \times 2\pi} = 1,2310 \tag{5.29}$$

These boundaries and the Suppressor operating domain are displayed in the following graphic (Figure 5.4).

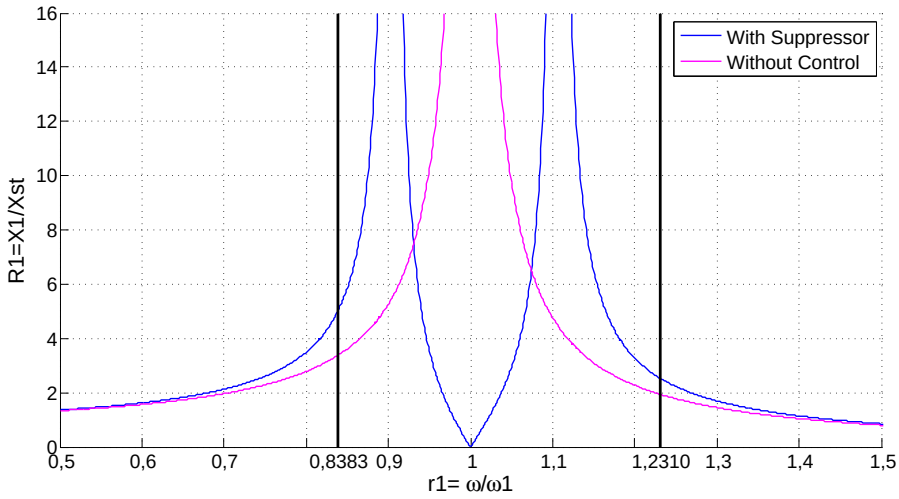

Figure 5.4: Suppressor Operating Limits.

Figure 5.4 displays the dynamic amplification curves of the pedestrian action according to the frequency of excitation, with and without the implementation of the control system.

Here, the "spring" of the Suppressor is able to change its stiffness between the operating limits specified in Figure 5.4, adjusting this characteristic for any frequency value between $2,54 < f < 3,73\,\text{Hz}$. With this, the dynamic amplification factor (X_1/X_{1st}) remains near to zero in this complete range of frequencies.

To ensure that beyond the maximum and minimum operating limits previously defined, the dynamic amplification factor (X_1/X_{1st}) remains below 7,04 (see equation (5.3)) and consequently the maximum acceleration registered with the control system (Suppressor) is also below the imposed limit $(\text{a} < 0,7\text{m/s}^2)$, required for the structure [15], one defined the following stiffness transitions:

$$\text{For:} \quad f < 2,54 \text{ Hz} \quad \rightarrow \quad k_2 = K_A = 241,67 \text{ kN/m} \quad (T^w \geq 70°C) \tag{5.30}$$

$$\text{For:} \quad f > 3,73 \text{ Hz} \quad \rightarrow \quad k_2 = K_M = 112,07 \text{ kN/m} \quad (T^w \leq 35°C) \tag{5.31}$$

$$\text{For:} \quad 2,54 < f < 3,73 \text{ Hz} \quad \rightarrow \quad k_2 = \text{variable} \quad (T^w = \text{variable}) \tag{5.32}$$

With this, when the excitation frequency exceeds the defined operating limits, a stiffness transition from K_A to K_M or vice versa, occurs.

T^w is the wire temperature that, according to the studies carried out in chapter 3, ensures the proposed stiffness values. The considered stiffness-temperature relation can be found in Figure D.2 of the appendix D.

To ensure the energetic efficiency of the proposed control system, it must comprise a system of sensors that allow its activation only when strictly necessary.

In order to clarify the considerations set in this section, Table 5.9 summarizes the most important points of the Suppressor's operating limits.

Table 5.9: Suppressor's operating limits

Frequency		**Operating limits**		**Stiffness limits**	
Martensite f_{supp} (Hz)	Austenite f_{supp} (Hz)	Martensite f_{supp}/f_n (Hz/Hz)	Austenite f_{supp}/f_n (Hz/Hz)	Martensite K_M (kN/m)	Austenite K_A (kN/m)
2.54	3.73	0.8383	1.2310	112.07	241.67

5.5.2 TMD with Variable Stiffness

In order to maintain the same stiffness boundaries previously calculated for the Suppressor in section 5.5.1 $(112,07 < K^{\text{wire}} < 241,67 \text{ kN/m})$, the minimum and maximum TMD operating frequencies were obtained according to equations (4.20), (4.18) and (5.21):

$$k_2 = m_2 \times \omega_{2,opt}^2$$

$$\omega_{2,opt}^2 = \frac{1}{1+\mu} \times \omega_1 \text{ (rad/s)}$$

$$f = \frac{\omega}{2\pi} \text{ (Hz)}$$

- Minimun operating frequency: (Martensite Phase)

$$K_M = 112,07 \text{ kN/m} \rightarrow \omega_{2,opt} = \sqrt{\frac{112,07}{440 \times 10^{-3}}} = 15,9596 \text{ (rad/s)} \tag{5.33}$$

considering equation (4.18):

$$\rightarrow \omega = 15,9596 \times (1 + \mu) = 16,6171 \text{ (rad/s)} \tag{5.34}$$

$$\rightarrow f = \frac{16,6171}{2\pi} = 2,6447 \text{ (Hz)} \tag{5.35}$$

- Maximun operating frequency: (Austenite Phase)

$$K_A = 241,67 \text{ kN/m} \rightarrow \omega_{2,opt} = \sqrt{\frac{241,67}{440 \times 10^{-3}}} = 23,4359 \text{ (rad/s)} \tag{5.36}$$

considering equation (4.18):

$$\rightarrow \omega = 23,4359 \times (1 + \mu) = 24,4014 \text{ (rad/s)} \tag{5.37}$$

$$\rightarrow f = \frac{24,4014}{2\pi} = 3,8836 \text{ (Hz)} \tag{5.38}$$

Dividing the limit frequencies above mentioned by the value of the structure's natural frequency (3,03 Hz), one achieves the operating boundaries of the TMD.

$$\text{Max. operating limit:} \quad r_1 = \frac{\omega}{\omega_1} = \frac{2,6447 \times 2\pi}{3,03 \times 2\pi} = 0,8728 \tag{5.39}$$

$$\text{Min. operating limit:} \quad r_1 = \frac{\omega}{\omega_1} = \frac{3,8836 \times 2\pi}{3,03 \times 2\pi} = 1,2817 \tag{5.40}$$

The previously defined limits and the TMD operating domain are displayed in the following graphic (Figure 5.5).

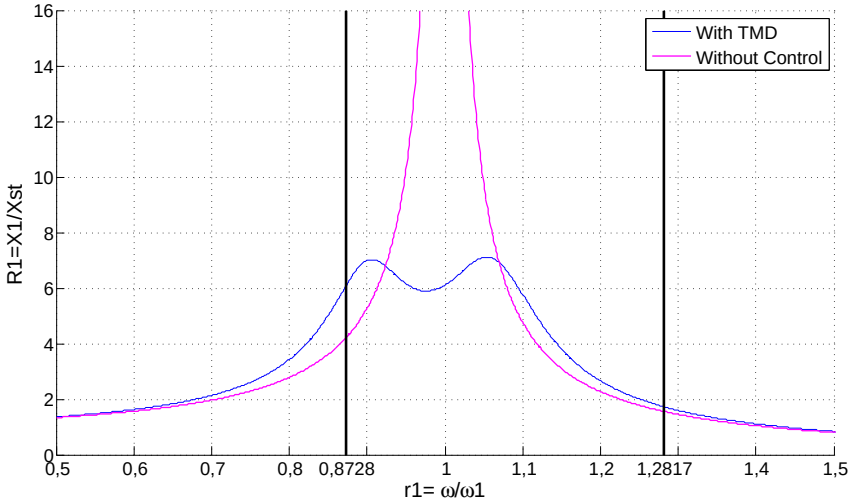

Figure 5.5: TMD Operating Limits.

Figure 5.5 displays the dynamic amplification curves of the pedestrian action according to the frequency of excitation, with and without the implementation of the control system.

Here, the TMD's "spring" is able to change its stiffness between the operating limits specified in Figure 5.5, adjusting this characteristic for any frequency value between $2,6447 < f < 3,8836$ Hz.

For frequency values outside the operating limits, the TMD presents the following stiffnesses:

$$\text{For:} \quad f < 2,447 \text{ Hz} \quad \rightarrow \quad k_2 = K_M = 112,07 \text{ kN/m} \quad (T^w \leq 35°C) \tag{5.41}$$

$$\text{For:} \quad f > 3,8836 \text{ Hz} \quad \rightarrow \quad k_2 = K_A = 241,67 \text{ kN/m} \quad (T^w \geq 70°C) \tag{5.42}$$

$$\text{For:} \quad 2,447 < f < 3,8836 \text{ Hz} \quad \rightarrow \quad k_2 = \text{variable} \quad (T^w = \text{variable}) \tag{5.43}$$

It is important to emphasize that for the entire frequencies domain, the dynamic amplification factor (X_1/X_{1st}) remains below 7.04 and consequently the maximum acceleration registered with the control system (TMD) is also below the imposed limit ($a < 0,7 \text{m/s}^2$).

In order to clarify the considerations set in this section, Table 5.10 summarizes the most important points of the TMD's operating limits.

Table 5.10: TMD's operating limits

Frequency		**Operating limits**		**Stiffness limits**	
Martensite f_{exc} (Hz)	Austenite f_{exc} (Hz)	Martensite f_{exc}/f_n (Hz/Hz)	Austenite f_{exc}/f_n (Hz/Hz)	Martensite K_M (kN/m)	Austenite K_A (kN/m)
2.6447	3.8836	0.8728	1.2817	112.07	241.67

All the numerical data of section 5.4 and section 5.5 is described in the appendix D of this document.

Chapter 6

Numerical Analysis of a Simplified Two Degree of Freedom Dynamic System

6.1 Introduction

This chapter discusses the analysis of a Simplified Two Degree of Freedom Dynamic System. The implementation of such system in MATLAB (The Mathworks, 2014) software, is also addressed. Some practical examples regarding the case study of section 5.2 are further presented, in order to validate and prove the efficiency of the proposed control systems. Comparisons between variants of those control systems are also presented in this chapter.

In this section an implementation of the short-time Fourier transformation algorithm (STFT) is discussed, to be used in the model to determine the real-time frequency of a sinusoidal signal as it changes over time.

Lastly, two numerical models, applied to this thesis case study, are presented. Those models are capable of applying a force to the structure, reproduce its behavior (displacement, velocity or acceleration), read the structural response throughout the STFT model and tune the control systems, changing their stiffness in order to improve their performance and mitigate the structural response.

6.2 Simplified Two Degree of Freedom Dynamic System

In order to perform a numerical analysis of the structural behavior (footbridge - case study) when subjected to a vibration control using the two devices referenced in sections 4.3 and 4.2 (TMD and Suppressor), two Simplified Two Degree of Freedom Dynamic Systems were implemented in MATLAB (The Mathworks, 2014) software, each one corresponding to a control system device.

- *Vibration Suppressor*:

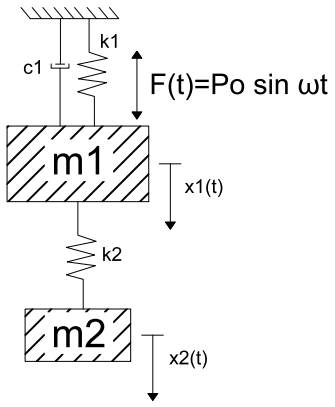

Figure 6.1: Vibration Suppressor - Two Degree of Freedom Dynamic System.

- *TMD*:

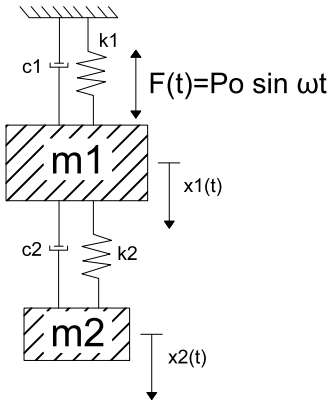

Figure 6.2: TMD - Two Degree of Freedom Dynamic System.

Where,

$$m_1 = 10,68 \text{ ton}; \quad c_1 = 0,8133 \text{ kN.s/m}; \quad k_1 = 3870,9 \text{ kN/m};$$
$$m_2 = 0,440 \text{ ton}; \quad c_2 = 1,8827 \text{ kN.s/m}; \quad k_2 = \text{variable kN/m}.$$

The damping coefficient of the primary system (c_1) was based on,

$$\zeta = \frac{c_1}{2\sqrt{k_1 \cdot m_1}} \tag{6.1}$$

where, according to section 5.2, $\zeta = 0,002$ is the damping ratio considered for the footbridge.

It is mandatory to note that this damping coefficient (c_1) corresponds to a very low damping ratio ($0 < \zeta < 1\%$) and is therefore possible to use the Den Hartog's solution [12], as previously mentioned in section 4.3.

6.3 Short-time Fourier transforms

6.3.1 Short-time Fourier transforms - Description

"The short time Fourier transform (STFT) is the most widely used method for studying non-stationary signals." - Nagarajaiah and Varadarajan, [26]

In order to test the efficiency of a vibration control system with the peculiarity of being able to change its spring stiffness (using SMAs), the sinusoidal excitation signal applied to a structure must be composed by two or more sections where different vibration frequencies can be highlighted.

Thus, in order to identify those excitation frequencies, as well as the instant of transition between them, a STFT based algorithm was implemented.

The basic idea of short time Fourier transforms is to break the complete signal into small time segments in order to analyze them, tracking the frequency of each of those segments.

For each different time segment, a different frequency spectrum is obtained and the sum of all spectra corresponds to the complete time-frequency distribution of the whole signal.

The idea proposed in this study is to use STFT to identify the dominant frequency in each time segment of the signal and monitor its variation as function of time in order to be able to correctly tune the stiffness of the control system in concern.

According to [25], Short-time Fourier transforms can be mathematically described by:

$$\mathrm{STFT}(t,\omega) = S(t,\omega) = \int \mathrm{s}(\tau)\mathrm{w}(\tau - t)e^{-j\omega\tau}d\tau \tag{6.2}$$

Here, $\mathrm{w}(\tau - t)$ is the window function, commonly a Hann window around zero, chosen to leave the signal more or less unaltered around the time (t), and $\mathrm{s}(\tau)$ is the signal to be transformed. $S(t,\omega)$ is the Fourier Transform of $\mathrm{s}(\tau)\mathrm{w}(\tau - t)$, a complex function representing the phase and magnitude of the signal over time and frequency. The running time is τ and the fixed time is t. Since the window function emphasizes the signal around time, t, the Fourier spectrum will emphasize the frequencies at that time.

It is extremely important to properly define the window size. A small window size allows to identify the precise time at which the signal changes, yet it turns difficult to identify its precise frequencies. On the other hand, a large window size allows the frequencies to be precisely identified but the time between frequency changes becomes blurred.

The correct implementation of the STFT in the control algorithm follows the arrangement of Figure 6.3.

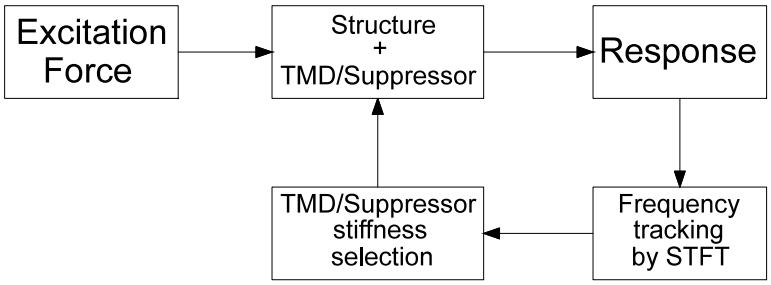

Figure 6.3: Implementation of the STFT in the control algorithm.

6.3.2 Short-time Fourier transforms - Implementation

Unlike the traditional tuned mass damper (TMD) system, which can only be tuned to a fixed frequency, the new "variable stiffness" control system, developed in this dissertation, is capable of continuously vary its stiffness and retuning the structure's frequency in real time throughout a STFT control algorithm.

In order to deploy this STFT control algorithm in the Two Degree of Freedom Dynamic System numerical model, a simple STFT frequency-tracker model was developed in MATLAB (The Mathworks, 2014) software, using MATLAB's Signal Processing Toolbox, spectrogram feature.

The MATLAB implementation of the simple STFT frequency-tracker model is further described in the Appendix E of this dissertation.

6.3.2.1 STFT in the Two Degree of Freedom Dynamic System

Initially, the STFT algorithm was applied to the signal of the excitation force acting on the structure of this thesis case study (see section 5.2).

A sinusoidal force $F(t) = P_o \sin \omega t$, was applied in the main mass of the two degrees of freedom system, representative of the case study structure. This sinusoidal force has a duration of 10 seconds, where the frequency changes from 5 Hz to 3,03 Hz triggering a resonance situation in the structure, as it can be seen in Figures 6.4 and 6.5.

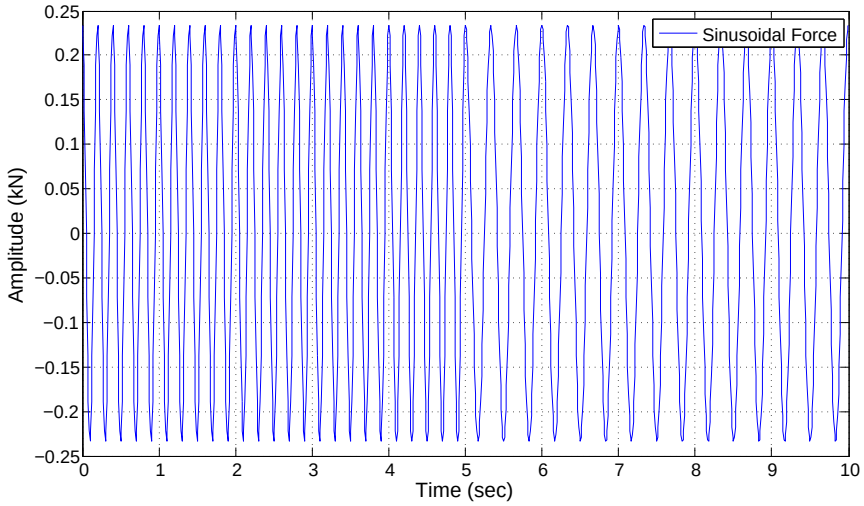

Figure 6.4: Sinusoidal force where the frequency changes from 5 Hz to 3,03 Hz - Input force signal.

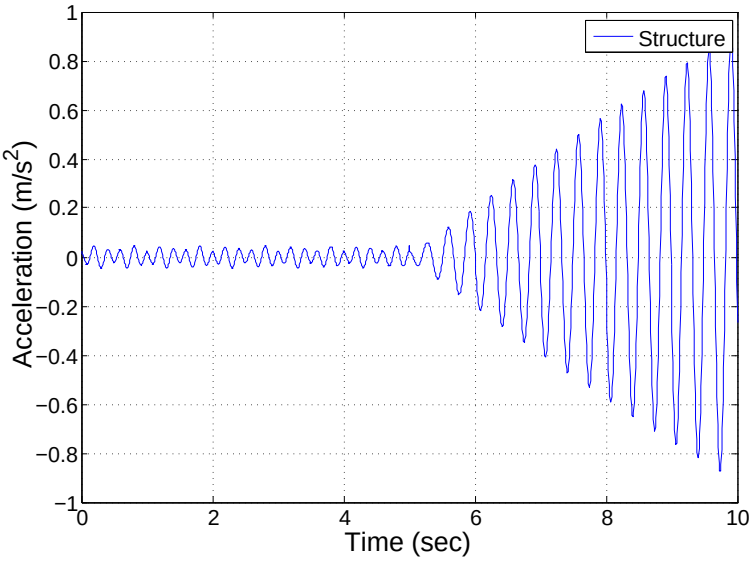

Figure 6.5: Resonance situation triggered in the structure of the case study - Output response signal.

In Figure 6.5, when the frequency of the input force (Figure 6.4) changes from 5 Hz to 3,03 Hz, the structure enters into a resonance state, where its vertical acceleration increases to values beyond the previously defined limit of 0,7 m/s^2.

Running the STFT algorithm implemented in the input force signal (sinusoidal force), one obtains the spectrogram represented in Figure 6.6.

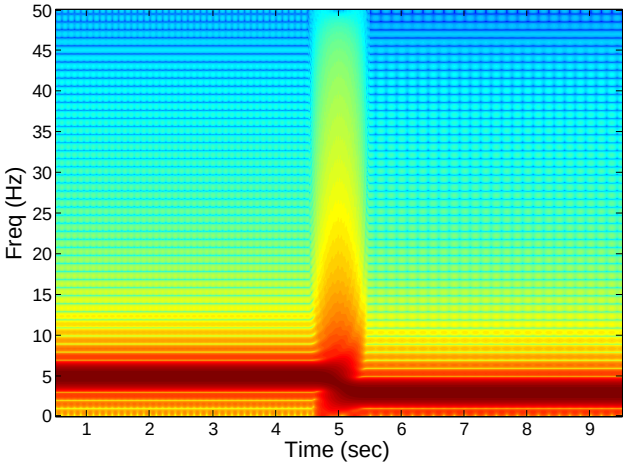

Figure 6.6: Short-time Fourier transform spectrum - Input force signal.

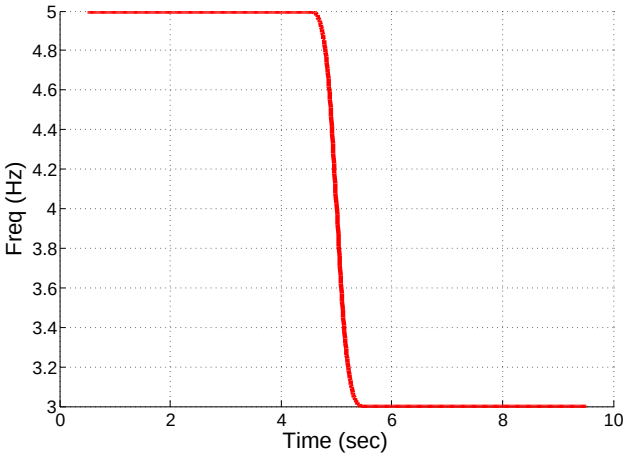

Figure 6.7: Frequency tracking - Input force signal.

Alternatively, running the STFT algorithm in the output response signal (structure's response to the input force signal), one obtains the following spectrogram:

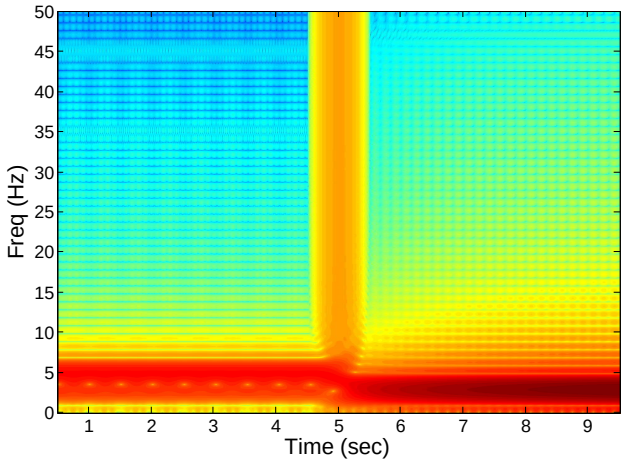

Figure 6.8: Short-time Fourier transform spectrum - Output response signal.

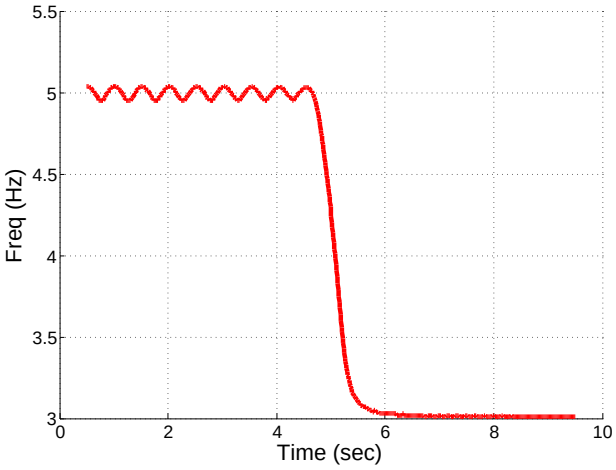

Figure 6.9: Frequency tracking - Output response signal.

Comparing the spectra obtained in Figures 6.6 and 6.7 with the ones from Figures 6.8 and 6.9, it is possible to draw some conclusions. A slightly different accuracy between the spectra of the Figures 6.6 and 6.8 turns out to be more pronounced during the first 5 seconds of the acting force, where the frequency remains at 5 Hz. This difference is also easily noted by comparing Figures 6.7 and 6.9, where in the last one, the initial baseline slightly bounces around 5 Hz.

Despite those differences, the results of applying the STFT algorithm in the applied force and in the structure's response end up being very similar.

A complete model for the case study, applying the STFT algorithm directly into the structural response, will also be further presented in this study.

6.4 Two Degree of Freedom Dynamic System - MATLAB Implementation

The model implemented in this section relies upon a dynamic analysis of a Two Degree of Freedom System. This model is based on the Newmark's method which is a numerical integration method used to solve differential equations and numerically evaluate the dynamic response of structures.

The model is suitable for both TMD and Suppressor control systems, differing only in the configuration of the damping matrix ($\mathbb{C}$), in the operating limits and in the calculation of the stiffness matrix ($\mathbb{K}$), according to the control system in concern.

6.4.1 Dynamic Analysis Model - MATLAB

The Dynamic Analysis Model can be unfolded into a set of five main Scripts, each one with a different purpose:

1. `harmonic_force.m`
2. `force_interpolation.m`
3. `STFT_algorithm.m`
4. `control_system_stiffness.m`
5. `newmark_mdof.m`

1. `harmonic_force.m`

   Defines the sinusoidal force $F(t) = P_0 \cos(\omega \cdot t)$ acting on the structure.

   Considering this thesis case study, the previously defined time history force function $F(t) = 18,7\cos(3,03 \cdot 2\pi \cdot t)$, representative of the applied force that stimulates the first vertical vibration mode of the structure for a pedestrian density of 1pedestrian/m^2, was taken into account.

   In order to successfully implement this force in the one degree of freedom system (structure) one had to apply a P_0 concentrated load (N) instead of a distributed one (N/m). Thus, it became necessary to multiply $P_0 = 18,7$ N/m by the influence length of the footbridge. Knowing that the footbridge is bi-supported and counts on a 30m length between the ends, it was considered a certain load distribution for the supports that resulted in a 12,5m influence length.

   Then, $F(t) = 18,7 \cdot 12,5 \cdot \cos(\omega \cdot t)$ is the force function acting on the structure, which has the ability to change its frequency (ω) over time. This force function comprises a fixed duration (eg: total_time = 10 sec) and, with a time step of $dt = 0.01$sec, it produces a 'force.txt' file with $NrSteps = (\text{total\_time}/dt) + 1$ steps. This 'force.txt' file contains the data describing the acting force in each step time.

2. `force_interpolation.m`

   Performs an interpolation between the values from the 'force.txt' file regarding each time step. This MATLAB defined function will be subsequently used for the calculation of the vertical acceleration of the structure, in the `newmark_mdof.m` script.

3. `STFT_algorithm.m`

   The STFT algorithm was implemented according to the assumptions specified in section 6.3.2. It breaks the Input signal into small time segments in order to analyze them, determining the frequencies in each segment. For each different time segment, a different frequency spectrum is obtained and the sum of all spectra corresponds to the complete time-frequency distribution of the whole signal.

4. `control_system_stiffness.m`

   The idea expressed in this script is to compute the stiffness of the control system as function of the frequency obtained through `STFT_algorithm.m`. This step is applied differently depending on the control system in concern.

   Using the TMD (with variable stiffness) as the vibration control system applied, the stiffness k_2 is calculated in accordance with the procedure described in section 5.5.2.

   Using the Vibration Suppressor (with variable stiffness) as the vibration control system applied, the stiffness k_2 is calculated in accordance with the procedure described in section 5.5.1.

   It is important to remember that each vibration control system is characterized by having different operating limits and thus it is necessary to define them. The stiffness limit values (due to the use of the SMA cable), and the stiffness transition boundaries used in the code are defined in sections 5.5.2 and 5.5.1.

5. `newmark_mdof.m`

   In the numerical models commonly used in the literature, the structures are often discretized into n degrees of freedom and their dynamic behavior is described through the well known differential equation used in the dynamics of structures. For a given spatial discretization, equation of motion assumes the form,

$$\mathbb{M}\ddot{\underline{u}} + \mathbb{C}\dot{\underline{u}} + \mathbb{K}\underline{u} = \underline{P} \tag{6.3}$$

   which involves the mass, the damping and the stiffness matrices of the structure (symmetrical matrices with DOF×DOF dimension), the vector of the "nodal" forces $\underline{P} = \underline{P}(t)$ and the displacement vector $\underline{u} = \underline{u}(t)$ (unknown) with the respective derivatives in order to time, $\dot{\underline{u}} = \dot{\underline{u}}(t)$ and $\ddot{\underline{u}} = \ddot{\underline{u}}(t)$ representing velocity and acceleration respectively.

   Considering a simplified two degrees of freedom system (TDOF), the inertia, stiffness, and damping matrices are defined by:

$$\mathbb{M} = \begin{bmatrix} m_1 & 0 \\ 0 & m_2 \end{bmatrix} (\text{ton}) \tag{6.4}$$

$$\mathbb{K} = \begin{bmatrix} k_1 + k_2 & -k_2 \\ -k_2 & k_2 \end{bmatrix} \text{(kN/m)} \tag{6.5}$$

$$\mathbb{C} = \begin{bmatrix} c_1 + c_2 & -c_2 \\ -c_2 & c_2 \end{bmatrix} \text{(kN.s/m)} \tag{6.6}$$

The input vectors of the initial conditions and the excitation force vector are defined as:

$$\underline{u}_0(t) = \begin{bmatrix} 0 \\ 0 \end{bmatrix} \text{(m)} \tag{6.7}$$

$$\dot{\underline{u}}_0(t) = \begin{bmatrix} 0 \\ 0 \end{bmatrix} \text{(m/s)} \tag{6.8}$$

$$\underline{P}(t) = \begin{bmatrix} P_0 \cos(\omega \cdot t) \\ 0 \end{bmatrix} \tag{6.9}$$

All the parameters of the equation of motion 6.3 are now set. Counting on this study purpose, it is now necessary to introduce the "variable stiffness feature" in the system. Then, for each step time, the stiffness matrix ($\mathbb{K}$) may or may not be changed depending on the variation of the excitation frequency. This change is characterized by the introduction of the k_2 stiffness, measured in `control_system_stiffness.m`, in the main $\mathbb{K}$ matrix. With the continuous variation of the $\mathbb{K}$ matrix, the equation of motion will consequently be changing for each time step.

In order to proceed with the dynamic analysis, the Newmark time-stepping method was applied in an algorithm adapted from *Chopra, Dynamics of Structures* [4].

The algorithm was based on the Newmark's Integration for MDOF Linear Elastic Systems and relies on the function:

$$\text{[t,u,v,a,fe]=newmark\_mdof(m,k,c,T,dt,u0,v0,force,varargin)} \tag{6.10}$$

This function integrates a MDOF system with mass matrix "m", stiffness matrix "k" and damping matrix "c", when subjected to an external load,

$$\underline{\text{force function}}: \quad \text{p(t)=force(t,ndof)} \tag{6.11}$$

defined in `harmonic_force.m`, where p(t) is a column vector with applied forces on the corresponding DOF. This function returns the displacement, velocity and acceleration of the system with respect to an inertial frame of reference.

INPUT:

[m] : Mass matrix of the system

[k] : Stiffness matrix of the system

[c] : Damping matrix of the system

[T]: Duration of the analysis

[dt]: Time-step

[u0]: Initial Position

[v0]: Initial Velocity

[force] : Function describing the applied force

[varargin]: Options - Include changing the value of the γ and β coefficient which appear in the formulation of the method.

OUTPUT:

[t]: Time vector

[u]: Displacement Response

[v]: Velocity

[a]: Acceleration

[fe]: Elastic force over time

The γ and β coefficients define the variation of the acceleration over a time step and also the stability and accuracy characteristics of the method.

Considering the average acceleration method, one defined: $\gamma = \frac{1}{2}$ and $\beta = \frac{1}{4}$, which are the recommended values to ensure that the method is unconditionally stable.

Summarizing the computer implementation, [4],

a) *Initial calculations*:

i. From the equation of motion: $\ddot{u}_0 = \frac{1}{m}(p_0 - c \cdot \dot{u}_0 - k \cdot u_0)$

ii. Select: dt (time step).

iii. Define: $\hat{k} = k + \frac{\gamma}{\beta\, dt}\, c + \frac{1}{\beta\, (dt)^2}\, m$

iv. Define: $a = \frac{1}{\beta\, dt}\, m + \frac{\gamma}{\beta}\, c \quad$ and $\quad b = \frac{1}{2\,\beta}\, m + dt\, \left(\frac{\gamma}{2\,\beta} - 1\right)\, c$

b) *Calculations for each time step, i*:

i. $\Delta\hat{p}_i = \Delta p_i + a \cdot \dot{u}_i + b \cdot \ddot{u}_i$

ii. $\Delta u_i = \frac{\Delta\hat{p}_i}{\hat{k}}$

iii. $\Delta\dot{u}_i = \frac{\gamma}{\beta\, dt}\, \Delta u_i - \frac{\gamma}{\beta}\, \dot{u}_i + dt\, \left(1 - \frac{\gamma}{2\,\beta}\right)\, \ddot{u}_i$

iv. $\Delta\ddot{u}_i = \frac{1}{\beta\,(dt)^2}\,\Delta u_i - \frac{1}{\beta\,dt}\,\dot{u}_i - \frac{1}{2\,\beta}\,\ddot{u}_i$

v. $u_{i+1} = u_i + \Delta u_i, \quad \dot{u}_{i+1} = \dot{u}_i + \Delta\dot{u}_i, \quad \ddot{u}_{i+1} = \ddot{u}_i + \Delta\ddot{u}_i, \quad p_{i+1} = p_i + \Delta p_i$

c) *Repetition for the next time step*: Replace i by $i+1$ and repeat step b).
Now, considering the equation of motion 6.3, one can obtain the acceleration for each time step:

$$\ddot{u}_{i+1} = \frac{1}{m}(p_{i+1} - c \cdot \dot{u}_{i+1} - k \cdot u_{i+1}) \tag{6.12}$$

Note that the k matrix varies according to each time step.

After this whole procedure is complete and the entire action is analyzed, the graphics reporting the acceleration of the structure and control system, as function of time, are plotted and the dynamic analysis is completed.

Chapter 7

Results of the Numerical Analysis

7.1 Introduction

Considering the studies carried out in chapter 3, the present chapter focus on the results obtained from the application of the control devices, designed in chapter 4, to the structure of section 5.2.

Several comparisons shall be developed with the primary purpose of proving the benefits of applying a SMA "spring" that enables both control devices (TMD and Suppressor) to have the "variable stiffness" property and hence, to be able to properly tune themselves for a wider range of frequencies.

Finally, the results obtained through a single numerical model, that computes the STFT algorithm directly on the structural response, in real time, will also be presented.

7.2 Initial Case

Performing an acceleration-time analysis for the case study structure (see section 5.2), using the model developed in chapter 6, important conclusions regarding the suitability of its application, can be drawn.

Applying the previously defined time history function $F(t) = 18,7 \cdot 12,5 \cdot \cos(3,03 \cdot 2\pi \cdot t)$ in the numerical model, one obtains the graphic of Figure 7.1.

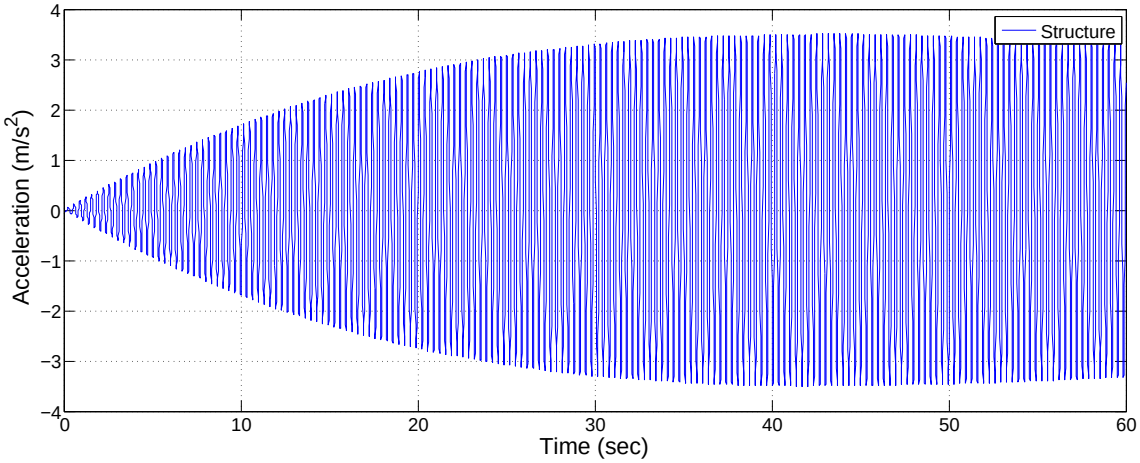

Figure 7.1: Acceleration-time graphic for the case study structure.

Figure 7.1 presents the acceleration-time history for the case study structure, when subjected to an input force with a frequency of 3,03 Hz. The structure enters into a resonance state, where its vertical acceleration achieves a maximum value of 3,5 m/s^2, which is consistent with the results obtained by T. Krus [15]. This maximum acceleration value is beyond the previously defined limit of 0,7 m/s^2, confirming once again, the necessity to implement a vibration control system in this structure.

7.3 Suppressor

This section presents the application of the Suppressor (designed in chapter 4) as the vibration control device in concern. Comparisons between different featured Suppressors are also shown in order to highlight their advantages.

7.3.1 Suppressor with Constant Stiffness (SCS) Vs. Suppressor with Variable Stiffness (SVS)

In order to highlight the importance of having a Suppressor with variable stiffness, one reports the following case.

With the introduction of this control system (without variable stiffness), the structure now comprises two new natural frequencies of vibration, which both differ from the initial natural frequency of the structure without the control system.

Considering the Suppressor designed in section 4.2, taking into account equation 4.11 and $\mu = 0,0411$, one calculates the new "upper" natural frequency of the structure (with Suppressor):

$$\begin{gathered}\left(\frac{\omega}{\omega_2}\right)^2 = \left(1+\frac{\mu}{2}\right) + \sqrt{\mu+\frac{\mu^2}{4}} \quad \Leftrightarrow \quad \left(\frac{\omega}{\omega_2}\right) = 1,11 \\ \Leftrightarrow \quad \omega = 1,11 \cdot 3,03 \cdot 2\pi \text{rad/s} \\ \text{Knowing that,} \quad \omega = f \cdot 2\pi \quad \rightarrow \quad f = 3,36\,Hz\end{gathered} \tag{7.1}$$

The goal of this comparison is to apply a time history force function $F(t) = 18,7 \cdot 12,5 \cdot \cos(f \cdot 2\pi \cdot t)$, where the frequency f changes from 3,03 Hz (natural frequency of the structure without control system) to 3,36 Hz (new superior natural frequency of the structure with Suppressor), and evaluate the behavior of the two types of Suppressor devices (without and with variable stiffness).

According to equation (4.9) and considering a Suppressor with Constant Stiffness (SCS) designed for a 3,03 Hz natural frequency, one obtains the following graphical representation of the structure's amplification factor.

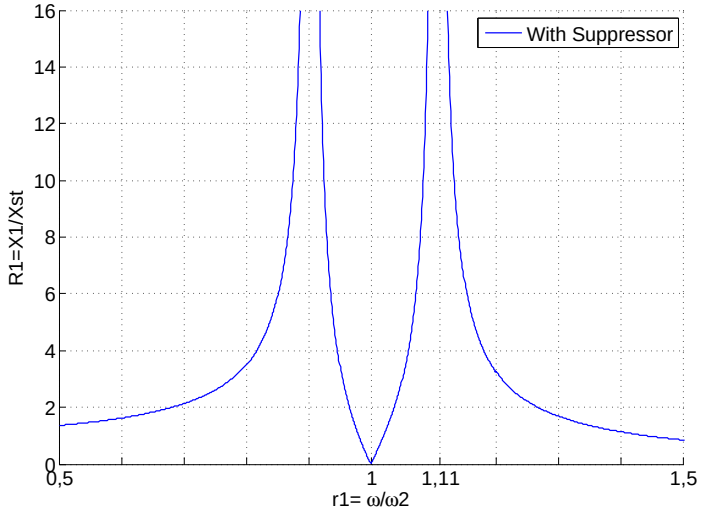

Figure 7.2: Amplitude of the main system motion with Suppressor (SCS) designed for a 3,03 Hz natural frequency.

Regarding the above mentioned statement, one divides the action in two phases:

1^{st} phase (0<Time<30 sec) $\rightarrow$ f = 3,03 Hz $\rightarrow$ Optimum stiffness: $k_2 = 159{,}477\,\mathrm{kN/m}$

2^{nd} phase (30<Time<60 sec) $\rightarrow$ f = 3,36 Hz $\rightarrow$ Optimum stiffness: $k_2 = 196{,}106\,\mathrm{kN/m}$

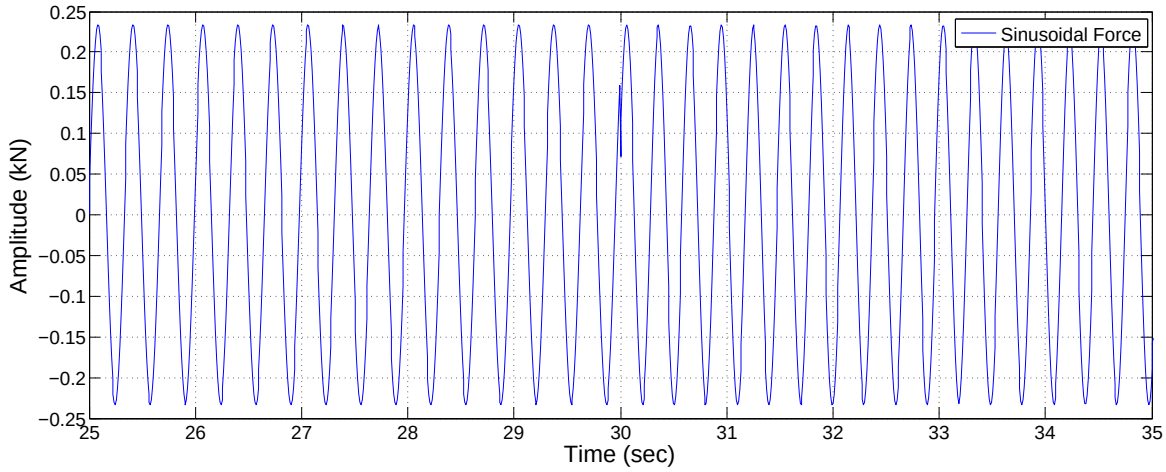

Figure 7.3: Sinusoidal force where the frequency changes from 3,03 Hz to 3,36 Hz. ($0 < \text{Time} < 30$ seconds $\rightarrow f = 3,03$ Hz) ; ($30 < \text{Time} < 60$ seconds $\rightarrow f = 3,36$ Hz).

Then, through the numerical analysis, one obtains the following acceleration-time graphics for the Suppressor with Constant Stiffness (SCS) and for the Suppressor with Variable Stiffness (SVS), respectively.

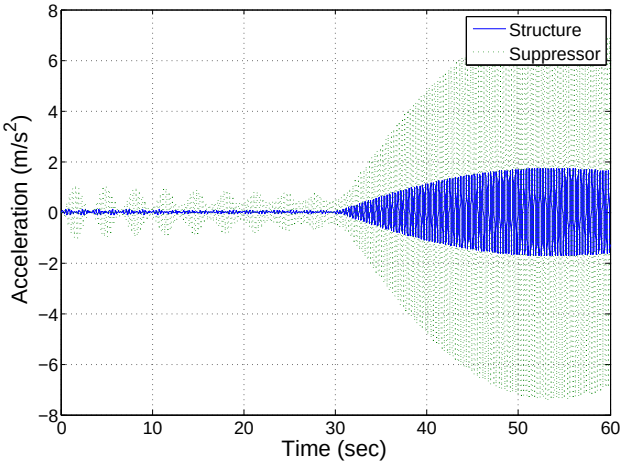

Figure 7.4: Acceleration-time graphic for the Suppressor with Constant Stiffness (SCS). $k_2 = 159{,}477\,\mathrm{kN/m}$ is maintained during the two phases.

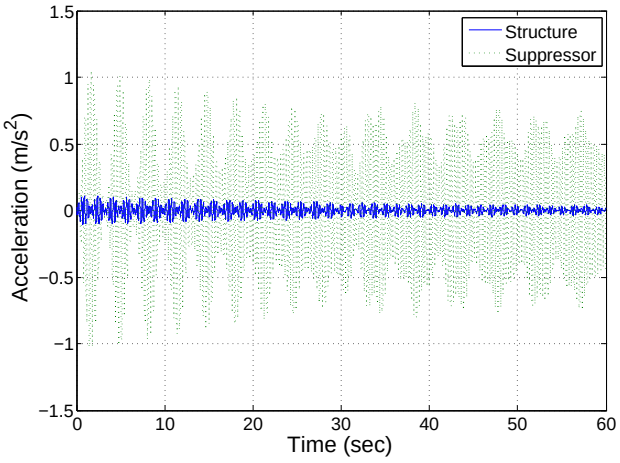

Figure 7.5: Acceleration-time graphic for the Suppressor with Variable Stiffness (SVS). In the 1^{st} phase $k_2 = 159{,}477\,\mathrm{kN/m}$ and in the 2^{nd} phase $k_2 = 196{,}106\,\mathrm{kN/m}$

The obtained results, for the structural acceleration, are very clear and can be summarized from the following observations:

- Regarding Figure 7.4 - Suppressor with Constant Stiffness (SCS):

$$1^{st}\text{ phase} \quad \rightarrow \quad a_{\max}\,(f = 3,03\mathrm{Hz}) = 0,107\,\mathrm{m/s^2}$$
$$2^{nd}\text{ phase} \quad \rightarrow \quad a_{\max}\,(f = 3,36\mathrm{Hz}) = 1,72\,\mathrm{m/s^2}$$

- Regarding Figure 7.5 - Suppressor with Variable Stiffness (SVS):

$$1^{st}\text{ phase} \quad \rightarrow \quad a_{\max}\,(f = 3,03\mathrm{Hz}) = 0,107\,\mathrm{m/s^2}$$
$$2^{nd}\text{ phase} \quad \rightarrow \quad a_{\max}\,(f = 3,36\mathrm{Hz}) = 0,060\,\mathrm{m/s^2}$$

In the 1^{st} phase (0<Time<30 sec) of Figure 7.4, with the Suppressor designed for the 3,03 Hz frequency ($k_2 = 159{,}477\,\mathrm{kN/m}$), the structural acceleration is nearly zero ($a_{\max} = 0,107\,\mathrm{m/s^2}$), as expected. Then, in the 2^{nd} phase (30<Time<60 sec), the frequency changes to 3,36 Hz but the Suppressor stiffness remains the same. This effect leads to a non-tuned Suppressor, causing an increase in the structural acceleration ($a_{\max} = 1,72\,\mathrm{m/s^2}$) to values beyond the predefined limits ($a_{\max} = 0,7\,\mathrm{m/s^2}$).

In the 1^{st} phase (0<Time<30 sec) of Figure 7.5, the structural acceleration is equal to the one defined for the Suppressor with Constant Stiffness (SCS), (Figure 7.4). In the 2^{nd} phase (30<Time<60 sec), when the frequency changes to 3,36 Hz, the Suppressor changes its stiffness (to $k_2 = 196{,}106\,\mathrm{kN/m}$) and stays tuned. With this, the structural acceleration remains near zero ($a_{\max} = 0,107\,\mathrm{m/s^2}$) and the action of the Suppressor (SVS) becomes widespread.

Considering the ability to change its stiffness, in the 2^{nd} phase of the action, the Suppressor (SVS) promotes an improvement in the reduction of the structural acceleration of 96.51% when compared with the Suppressor (SCS).

7.3.2 SVS with no Stiffness Transition Vs. SVS with Stiffness Transition (SVST)

The main goal of this comparison is to highlight the importance of having a Suppressor with Stiffness Transition, confirming the principles described in section 5.5.1. For this, it is extremely important to review the operating limits implicit in Table 5.9 and the stiffness transitions mentioned in equations (5.30), (5.31) and (5.32).

In order to achieve the situation where the Suppressor operating limits become exceeded, a specific time history force function had to be applied, where the frequency f changes from 3,73 Hz (upper frequency operating limit of the Suppressor) to 3,90 Hz (frequency beyond the operating limit of the Suppressor).

It is noteworthy that this frequency ($f = 3{,}90$ Hz) was chosen to be beyond the Suppressor's "upper" operating limit and was obtained by setting the denominator of the equation 4.7 to zero, but this time, counting on a Suppressor tuned for $\omega_2 = 3,73 \cdot 2\pi$ rad/s.

Then, the action is divided in two phases:

1^{st} phase (0<Time<30 sec) $\rightarrow$ f = 3,73 Hz $\rightarrow$ Optimum stiffness: $k_2 = 241{,}67$ kN/m

2^{nd} phase (30<Time<60 sec) $\rightarrow$ f = 3,90 Hz $\rightarrow$

$$\rightarrow \quad \text{Optimum stiffness:} \begin{cases} k_2 = 112,07\,\text{kN/m} & \text{(With Stiffness Transition)} \\ k_2 = 241,67\,\text{kN/m} & \text{(Without Stiffness Transition)} \end{cases}$$

Considering the above mentioned specifications, one obtains the following graphical representation of the structure's amplification factor, with and without stiffness transition.

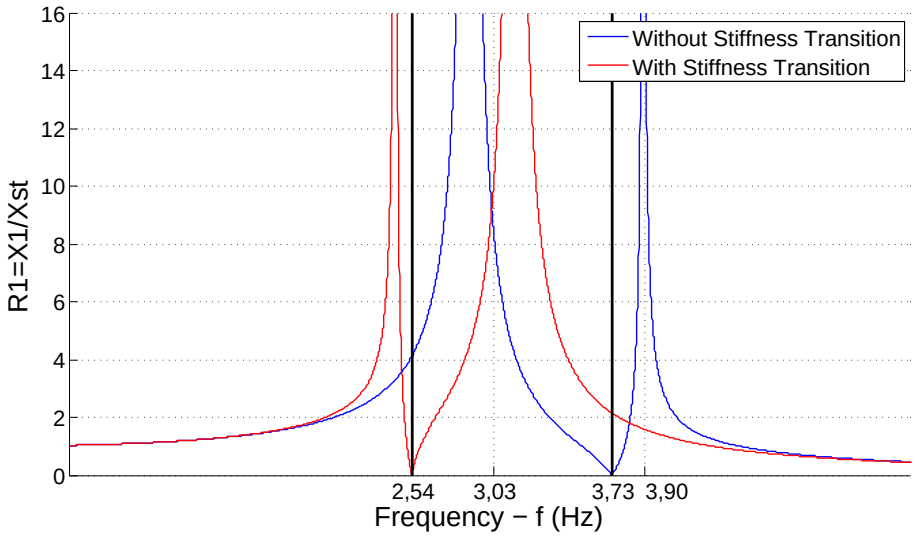

Figure 7.6: Amplitude of the main system motion with Suppressor. Stiffness transition and Operating Limits representation.

The above Figure 7.6 was obtained by considering the same foundations as the graphic of Figure 7.2, but in this case, the operational limits from Table 5.9 are displayed (vertical black lines) and the horizontal axis represent the excitation frequency imposed to the structure.

- SVS Without Stiffness Transition: When f changes from 3,73 Hz to 3,90 Hz, as the Suppressor reached the defined operating limit, its stiffness remains constant (k_2 = 241,67 kN/m) and the graphic displays the "Blue" position. Here, it is possible to observe that for f = 3,90 Hz, the amplitude of the main system motion increases and consequently also does the structural acceleration.

- SVS With Stiffness Transition: When f = 3,73 Hz, the Suppressor stiffness becomes k_2 = 241,67 kN/m and the graphic displays the "Blue" position. When f = 3,90 Hz, the Suppressor stiffness changes to k_2 = 112,07 kN/m and the graphic now displays the "Red" position. Here, it is possible to observe that for f = 3,90 Hz, the amplitude of the main system motion (and consequently the structural acceleration) remains close to zero.

Then, through the numerical analysis, one obtains the following acceleration-time graphics for the Suppressor SVS without and with stiffness transition, respectively.

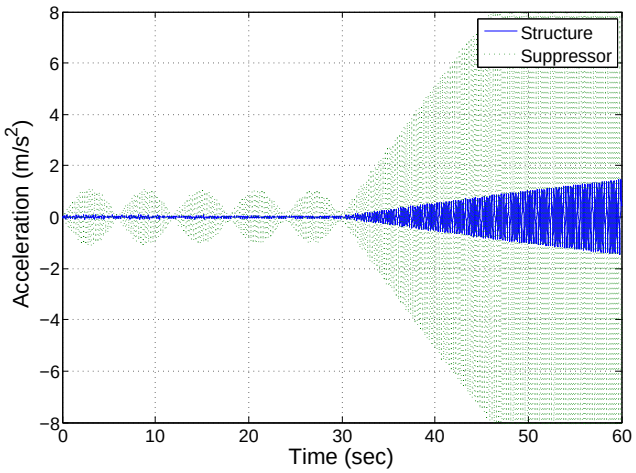

Figure 7.7: Acceleration-time graphic for the Suppressor (SVS) Without Stiffness Transition. k_2 = 241,67 kN/m is maintained during the two phases.

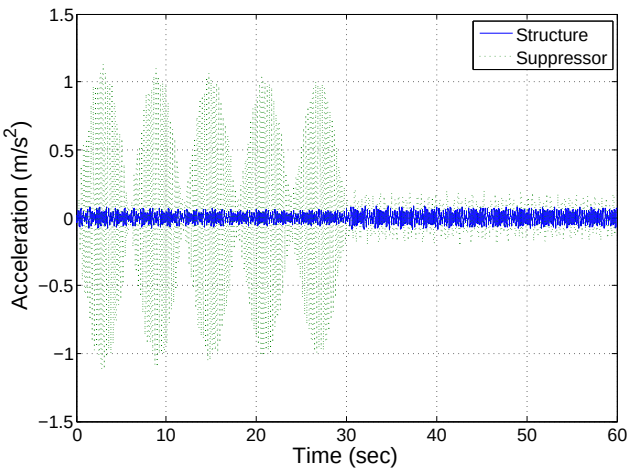

Figure 7.8: Acceleration-time graphic for the Suppressor (SVS) With Stiffness Transition. In the 1^{st} phase k_2 = 241,67 kN/m and in the 2^{nd} phase k_2 = 112,07 kN/m.

The obtained results, for the structural acceleration, can be summarized from the following observations:

- Regarding Figure 7.7 - Suppressor (SVS) Without Stiffness Transition:

$$1^{st} \text{ phase} \quad \rightarrow \quad a_{\max}\,(f = 3,73\text{Hz}) = 0,075\,\text{m/s}^2$$
$$2^{nd} \text{ phase} \quad \rightarrow \quad a_{\max}\,(f = 3,90\text{Hz}) = 1,45\,\text{m/s}^2$$

- Regarding Figure 7.8 - Suppressor (SVS) With Stiffness Transition:

$$1^{st} \text{ phase} \quad \rightarrow \quad a_{\max}\,(f = 3,73\text{Hz}) = 0,075\,\text{m/s}^2$$
$$2^{nd} \text{ phase} \quad \rightarrow \quad a_{\max}\,(f = 3,90\text{Hz}) = 0,088\,\text{m/s}^2$$

For this specific situation, in the 2^{nd} phase of the action, the Suppressor (SVS) With Stiffness Transition promotes an improvement in the reduction of the structural acceleration of about 93.93%, when compared to the Suppressor (SVS) Without Stiffness Transition.

7.4 Tunned Mass Damper (TMD)

This section presents the application of the TMD (designed in chapter 4) as the vibration control device in concern. Comparisons between TMD's with and without variable stiffness were preformed in order to demonstrate the improvements brought by this new kind of approach.

7.4.1 TMD with Constant Stiffness (TMDCS) Vs. TMD with Variable Stiffness (TMDVS)

With the introduction of the TMD control system (without variable stiffness), the dynamic amplification factor of the structure is reduced, fulfilling the acceleration requirements previously stated. Yet, in the neighborhood of the TMD's (TMDCS) natural frequency, the amplification factor increases considerably (not as much as in the Suppressor case). This phenomenon can be seen in Figure 7.9.

Considering the TMD with Constant Stiffness (TMDCS) designed in section 5.3.1 for a 3,03 Hz natural frequency, one obtains the following graphical representation of the structure's amplification factor.

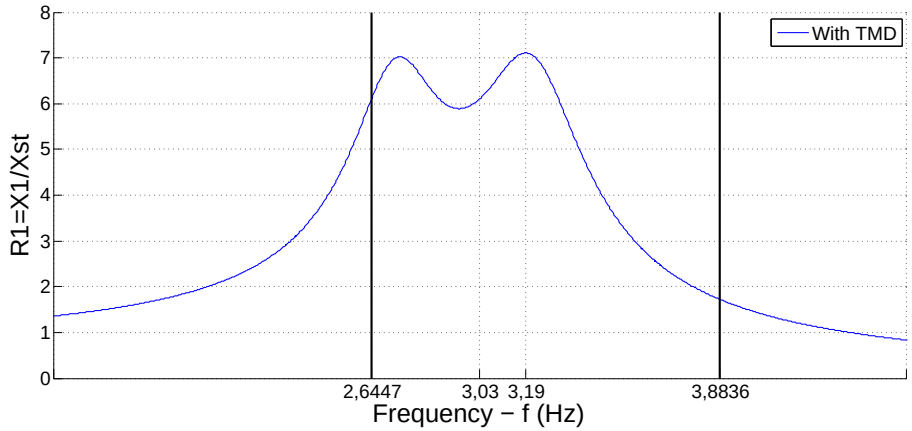

Figure 7.9: Amplitude of the main system motion with the TMD (TMDCS) designed for a 3,03 Hz natural frequency. Operating limits displayed (vertical lines).

The goal of this comparison is to apply a time history force function where the frequency f changes from 3,03 Hz (natural frequency of the structure without control system) to 3,19 Hz (new "upper" natural frequency of the structure with the TMD), and evaluate the behavior of the two types of TMD devices (without and with variable stiffness).

Regarding the above mentioned statement, one divides the action in two phases:

1^{st} phase (0<Time<30 sec) $\rightarrow$ f = 3,03 Hz $\rightarrow$ Optimum stiffness: $k_2 = 147{,}1\,\mathrm{kN/m}$

2^{nd} phase (30<Time<60 sec) $\rightarrow$ f = 3,19 Hz $\rightarrow$ Optimum stiffness: $k_2 = 163{,}1\,\mathrm{kN/m}$

It is worth noting that both frequencies are within the operating limits (variable stiffness domain) and also that the optimum stiffness values were based on the calculation method of the equations (5.5) and (5.8).

Then, through the numerical analysis, one obtains the following acceleration-time graphics for the TMD with Constant Stiffness (TMDCS) and for the TMD with Variable Stiffness (TMDVS), respectively.

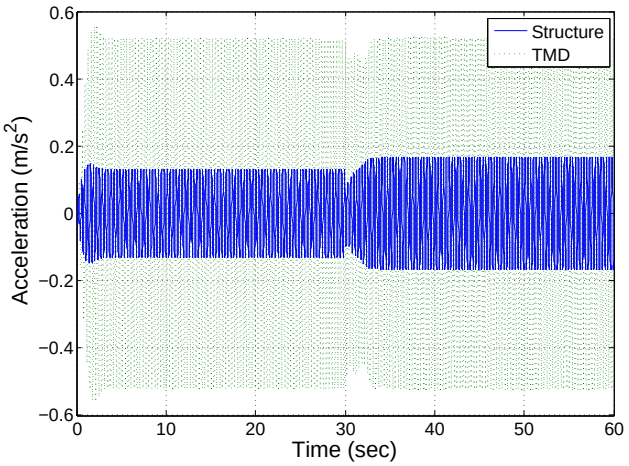

Figure 7.10: Acceleration-time graphic for the TMD with Constant Stiffness (TMDCS). $k_2 = 147{,}1\,\mathrm{kN/m}$ is maintained during the two phases.

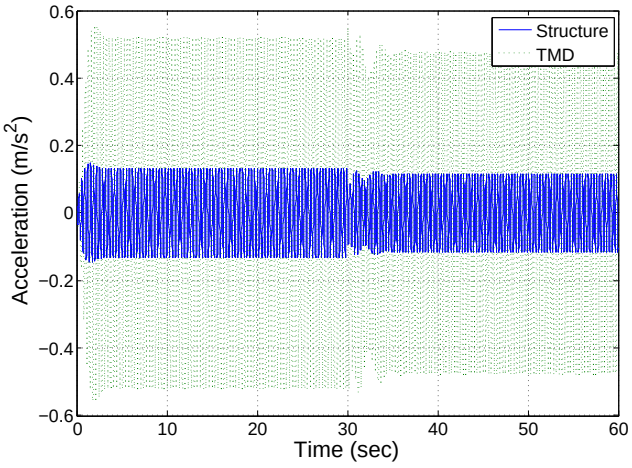

Figure 7.11: Acceleration-time graphic for the TMD with Variable Stiffness (TMDVS). In the 1^{st} phase $k_2 = 147{,}1$ kN/m and in the 2^{nd} phase $k_2 = 163{,}1\,\mathrm{kN/m}$.

The obtained results, for the structural acceleration, can be summarized from the following observations:

- Regarding Figure 7.10 - TMD with Constant Stiffness (TMDCS):

$$1^{st}\text{ phase} \quad \rightarrow \quad a_{\max}\,(f = 3,03\mathrm{Hz}) = 0,1315\,\mathrm{m/s^2}$$
$$2^{nd}\text{ phase} \quad \rightarrow \quad a_{\max}\,(f = 3,19\mathrm{Hz}) = 0,168\,\mathrm{m/s^2}$$

- Regarding Figure 7.11 - TMD with Variable Stiffness (TMDVS):

$$1^{st}\text{ phase} \quad \rightarrow \quad a_{\max}\,(f = 3,03\mathrm{Hz}) = 0,1315\,\mathrm{m/s^2}$$
$$2^{nd}\text{ phase} \quad \rightarrow \quad a_{\max}\,(f = 3,19\mathrm{Hz}) = 0,115\,\mathrm{m/s^2}$$

Considering the TMD with Constant Stiffness (TMDCS), when f changes from 3,03 Hz to 3,19 Hz, the TMD stiffness remains constant ($k_2 = 147{,}1\,\mathrm{kN/m}$) and then, in the 2^{nd} phase (30<Time<60 sec) this device is no longer correctly tuned, leading to a slight increase of the structural acceleration.

Considering the TMD with Variable Stiffness (TMDVS), when f changes from 3,03 Hz to 3,19 Hz, the TMD stiffness increases from $k_2 = 147{,}1\,\mathrm{kN/m}$ to $k_2 = 163{,}1\,\mathrm{kN/m}$ staying tuned and leading, this time, to a slight decrease of the structural acceleration.

Given the ability to change its stiffness, in the 2^{nd} phase of the action, the TMD (TMDVS) promotes an improvement in the reduction of the structural acceleration of 31.5% when compared to the TMD (TMDCS).

7.5 TMD Vs. Suppressor

Previously, it has been proven that the variable stiffness property provides significant benefits to the action of both control systems (TMDVS and SVST). Now, in this section, a comparison between those two control systems is performed and, to do so, a specific case where the frequency changes from 5 Hz to 3 Hz ($\approx$ resonant frequency) is considered.

Few conclusions about the action of both control systems, with variable stiffness, will also be presented.

7.5.1 Tuned Mass Damper (TMDVS) Vs. Suppressor (SVST)

Applying a time history force function where the frequency f changes from 5 Hz to 3 Hz, one can evaluate the behavior of the two types control systems (TMDVS) and (SVST).

Regarding the above mentioned statement, and considering a force applied during 10 seconds, one divides the action in two phases:

1^{st} phase (0<Time<5 sec) $\rightarrow$ f = 5 Hz

2^{nd} phase (5<Time<10 sec) $\rightarrow$ f = 3 Hz

Note: The STFT frequency tracking results for this action are reproduced in Figures 6.6 and 6.7.

Then, through the numerical analysis, one obtains the following acceleration-time graphics for the Tuned Mass Damper (TMDVS) and the Suppressor (SVST) actions, respectively.

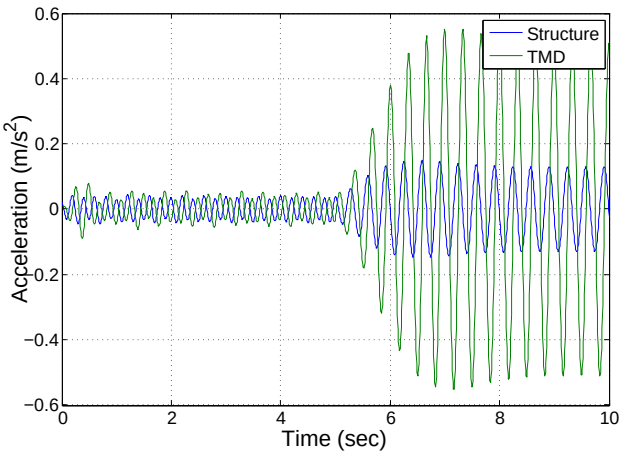

Figure 7.12: Acceleration-time graphic for the TMDVS action.

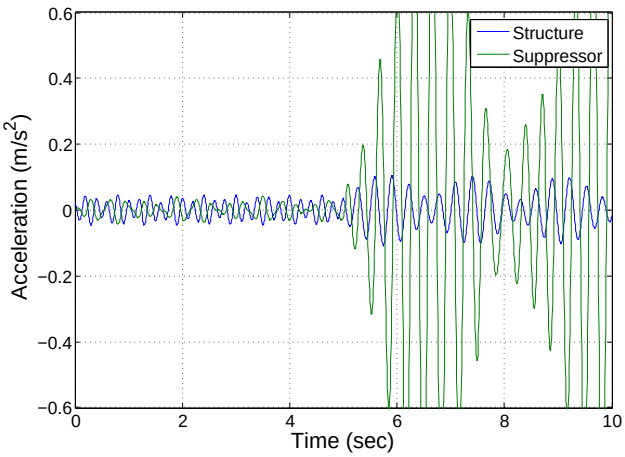

Figure 7.13: Acceleration-time graphic for the SVST action.

The obtained results, for the structural acceleration, can be summarized from the following observations:

- Regarding Figure 7.12 - (TMDVS):

$$1^{st} \text{ phase} \rightarrow a_{\max}\,(f = 5\text{Hz}) = 0,044\,\text{m/s}^2$$
$$2^{nd} \text{ phase} \rightarrow a_{\max}\,(f = 3\text{Hz}) = 0,148\,\text{m/s}^2$$

- Regarding Figure 7.13 - (SVST):

$$1^{st} \text{ phase} \quad \rightarrow \quad a_{\max}\,(f = 5\text{Hz}) = 0,045\,\text{m/s}^2$$
$$2^{nd} \text{ phase} \quad \rightarrow \quad a_{\max}\,(f = 3\text{Hz}) = 0,105\,\text{m/s}^2$$

It should be noted that, given the ability to change their stiffness, both control systems offer good results, showing an adequate reduction of the structural acceleration.

In the 1^{st} phase of the action, as the excitation frequency is relatively high, the structural acceleration presents itself moderate and then, both control systems do not have a major influence.

In the 2^{nd} phase of the action, when the excitation frequency becomes close to the natural frequency of the structure, the Suppressor (SVST) promotes an improvement in the reduction of the structural acceleration of about 29% when compared with the TMD (TMDVS). The improvement increases as the control system's action extends itself over time.

Although the Suppressor (SVST) is able to take the maximum advantage of the SMA's usage (regarding their capacity to change their stiffness), if a failure in the tuning process occurs, the opposite effect may be triggered, exponentially increasing the structural acceleration. In the TMD (TMDVS) case, the improvement achieved may not be so sharp, but the control system features the redundancy property i.e. if something in the tuning process fails, it does not cause major problems, giving it an advantage over the Suppressor (SVST).

7.6 TMD and Suppressor - STFT algorithm in the Output response signal

In the course of this dissertation, one considers the importance of the development and presentation of a single numerical model, which brings together all the scripts mentioned in section 6.4.1, computing the STFT frequency tracking algorithm directly on the structural response, in real time, as it should be.

This section presents several comparisons between the numerical model (STFT - Input force signal) described in section 6.4.1 and the new single model (STFT - Output response signal), in order to show the abilities and disabilities of this last one.

To do so, the same time history force function defined in section 7.5.1, is applied.

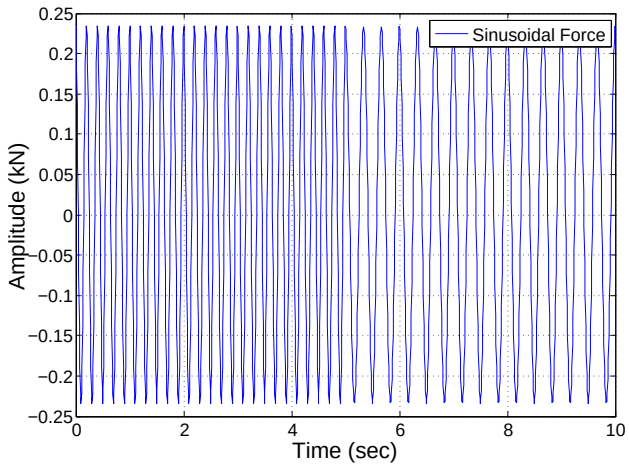

Figure 7.14: Sinusoidal force where the frequency changes from 5 Hz to 3 Hz.

7.6.1 Suppressor (SVST)

By applying the sinusoidal force displayed in Figure 7.14 to the case study structure and reproducing its behavior through the single numerical model, one obtains the following results.

With the introduction of the Suppressor in the system, it will change the way the main system behaves. Apart from reducing the structural vibration, this one will also change, somehow, the way in which the structure vibrates.

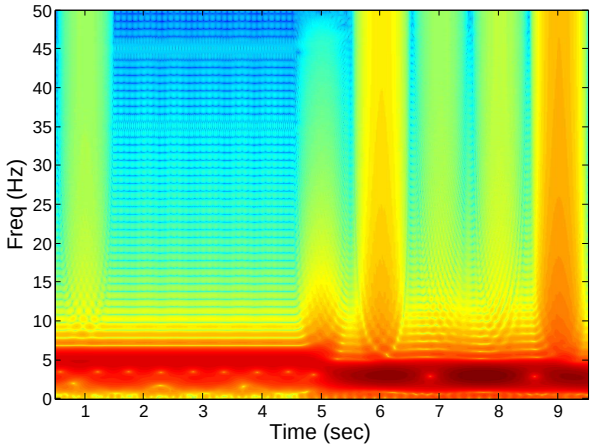

Figure 7.15: Short-time Fourier transform spectrum - Output response signal of the structure with SVST.

Through the observation of the Figure's 7.15 spectrum, some imperfections in the frequency-time domain can be highlighted, especially when compared with the spectrum from Figure 6.8.

Even with these imperfections, a correct major transition from 5 Hz to 3 Hz frequency can be easily seen.

Then, through the numerical analysis performed with the previously mentioned single numerical model, one obtains the following acceleration-time graphic for the Suppressor (SVST) action:

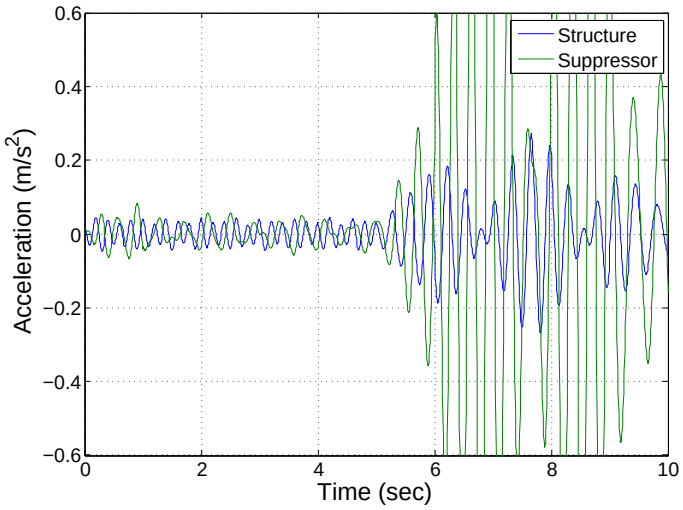

Figure 7.16: Acceleration-time graphic for the SVST action - STFT in the Output response signal.

Regarding Figure's 7.16 acceleration-time graphic, one obtains the following results:

$$1^{st} \text{ phase} \quad \rightarrow \quad a_{\max}\,(f = 5\text{Hz}) = 0,046\,\text{m/s}^2$$

$$2^{nd} \text{ phase} \quad \rightarrow \quad a_{\max}\,(f = 3\text{Hz}) = 0,270\,\text{m/s}^2$$

Now looking at Figure's 7.13 graphic, where the STFT frequency tracking algorithm was applied in the Input signal (force) and comparing it with the one obtained in the above Figure 7.16, some similarities and differences can be found.

In general, the structural behavior, presents himself similar in both graphics. Regarding the acceleration values, it is possible to observe that in the Figure's 7.16 case, the structural acceleration values are slightly higher (especially in the 2^{nd} phase). The appearance of more severe acceleration peaks, triggered by the Suppressor's movement influence in the system, could be the basis of the previous statement. This effect is softened over time.

Even with this slightly "more onerous" behavior, reproduced by the single numerical model with the STFT frequency tracking algorithm applied in the Output response signal, the Suppressor (SVST) action presents itself extremely effective, maintaining the structural acceleration far beneath the recommended limits.

7.6.2 Tuned Mass Damper (TMDVS)

Analyzing the same situation (as the above section 7.6.1), one reproduces the behavior of the structure with TMDVS, through the single numerical model with the STFT frequency tracking algorithm applied in the Output response signal.

With the introduction of the TMD on the main system, it will also change the way the main system behaves (as in the Suppressor case). Apart from reducing the structural vibration, this one will also change, the way in which the structure vibrates. Now considering Figure's 7.17 spectrum, one can highlight some imperfections in the frequency-time domain, especially when compared to the spectrum from Figure 6.8.

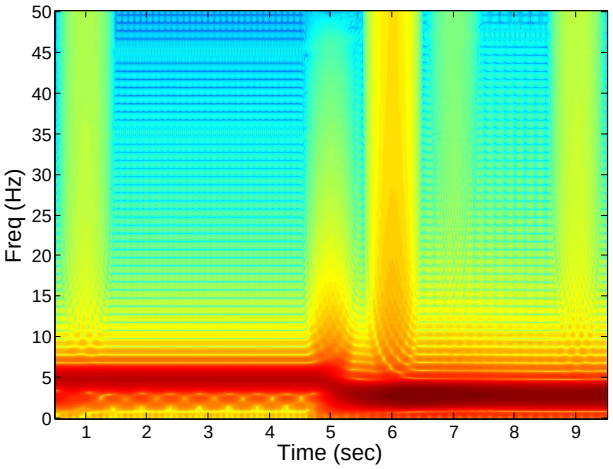

Figure 7.17: Short-time Fourier transform spectrum - Output response signal of the structure with TMDVS.

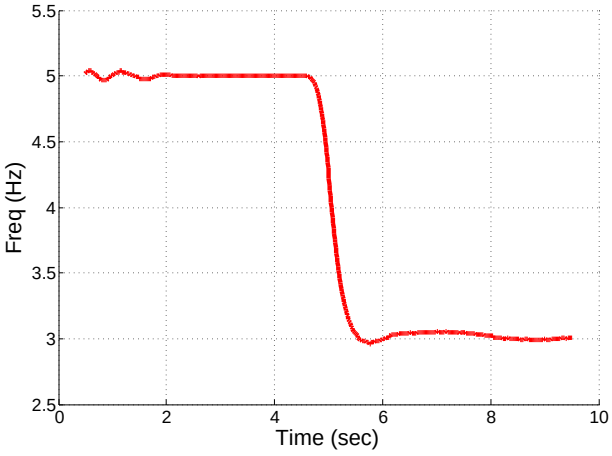

Figure 7.18: Frequency tracking - Output response signal of the structure with TMDVS.

Although it presents these slight differences from Figure 6.8, the spectrum of Figure 7.17 displays a more perfect frequency transition (from 5 Hz to 3 Hz) than the one in Figure 7.15.

The aforementioned statement is confirmed by the Figure 7.18 frequency tracking diagram, where the vibration frequency of the structure is relatively well defined over time, approaching the diagram presented Figure 6.9.

This improvement is due to the fact that, unlike the Suppressor, the TMD comprises a built-in damper, allowing it to have a more sustained action.

Then, through the analysis performed with the previously mentioned "single numerical model", one obtains the following acceleration-time graphic for the Tuned Mass Damper (TMDVS) action:

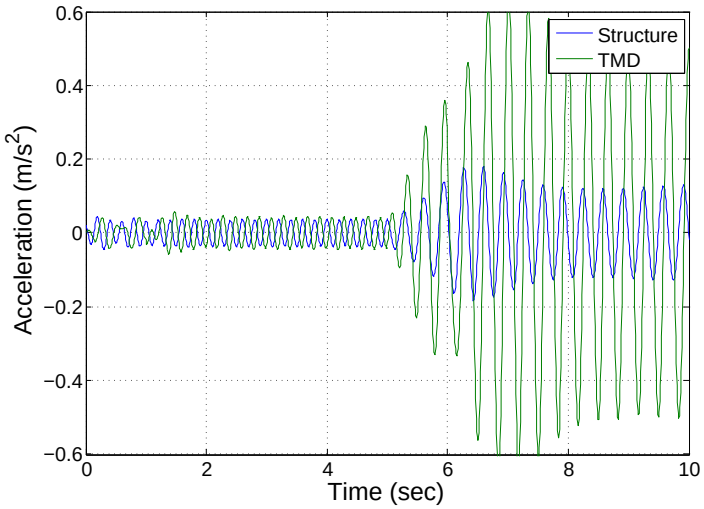

Figure 7.19: Acceleration-time graphic for the TMDVS action - STFT in the Output response signal.

Regarding Figure's 7.19 acceleration-time graphic, one obtains the following results:

1^{st} phase $\rightarrow$ $a_{\max}\,(f = 5\text{Hz}) = 0,044\,\text{m/s}^2$

2^{nd} phase $\rightarrow$ $a_{\max}\,(f = 3\text{Hz}) = 0,180\,\text{m/s}^2$

Comparing the graphic from Figure 7.19, with the one obtained in Figure 7.12 (with STFT algorithm in the Input force signal), one can conclude that, in general, the structural behavior presents himself similar in both cases.

Regarding the acceleration values, it is possible to observe that in Figure 7.19, the maximum structural acceleration value is slightly higher (in the 2^{nd} phase). Once again, this effect may be caused by the presence of the 2^{nd} Degree of Freedom (TMDVS) in the system, which causes changes in the way the structure moves and consequently those slightly changes in the vibration frequency of the system (see Figure 7.18).

Even with this slightly "more onerous" behavior, reproduced by the single numerical model with the STFT frequency tracking algorithm applied in the Output response signal, the Tuned Mass Damper (TMDVS) action also presents itself extremely effective, maintaining the structural acceleration far beneath the recommended limits.

Chapter 8

Summary, Conclusions and Future Work

This chapter presents the conclusions of the work developed in this document. Some possible future work of interest to the field of study, is also mentioned.

8.1 Summary and Conclusions

Currently, the development of new guidelines imposing harder service limitations to structures has been growing, and so does the need to explore new techniques that allow structures to comply with these guidelines, fulfilling all the necessary requirements and allowing them to provide a smooth operation. In order to do this, new materials with different and revealing characteristics are continuously studied in order to be applied in civil engineering problems, as well as in other fields of engineering.

Regarding this dissertation main purpose of designing a vibration control system (TMD type) which comprises the variable stiffness property and takes into account the possibility to use those new materials, one considered the hypothesis of performing a symbiosis between these two subjects.

Then, this dissertation presented a study carried out on Shape Memory Alloys (SMAs), emphasizing their ability to vary their mechanical properties, such as the modulus of elasticity (E), knowing that they are temperature sensitive materials. This ability derives from a crystallographic phase transformation that occurs in SMA materials called martensitic transformation. Martensitic transformation is highly dependent of stress and temperature and allows the occurrence of a transition between a high energy phase (austenite) and a low energy phase (martensite), giving birth to these materials remarkable properties.

The SMA material was then applied in two vibration control systems, already studied in the literature (Suppressor and Tuned Mass Damper), changing their main features and increasing their operating range.

Choosing *FLEXINOL* ® as the specific NiTi shape memory alloy studied in this section, an experimental program, including temperature controlled tensile tests, was conducted in order to perform the Young Modulus mapping of this material.

These experimental tests comprised an exhaustive analysis of a *FLEXINOL* ® sample providing a valuable insight on the main variables influencing this material's Young Modulus variability. It is also noteworthy that the experimental device developed in section 3, may be considered as a small scale prototype of the ATMDs operation basis, mentioned in this thesis.

After discussing the theoretical background concerning constitutive models for SMAs, a numerical model, coupling the mechanical and kinetic laws, was also developed. This model was based on a differential scanning calorimetry (DSC) test performed in [32].

The good performance of the numerical model was confirmed by comparing the numerical simulations with the experimental obtained data and the literature results. Regarding the literature results, one can conclude that the data obtained through both numerical and experimental approaches is highly representative of the one-way transformation, only differing at the level of the alloy's upper and lower elastic modulus limit values obtained. Afterwards, comparing the numerical data with the experimental one, it was possible to conclude that, despite some differences in the exponential growth behavior of the elastic modulus, both approaches present similar results, providing a trusted mapping of the *FLEXINOL* ® elastic modulus as function of temperature.

Considering the alloys upper and lower elastic modulus limit values, defined in the *FLEXINOL* ® actuator wires technical report [8], which increased the range of the E values covered by the transformation, one has obtained the stiffness-temperature relation, presented in the Appendix D. This relation was further used for the design of the vibration control systems.

Regarding the control systems studied in this document - initially the design models of both systems (Suppressor and TMD) were introduced, followed by a study carried out on the implementation of the "variable stiffness" property.

As mentioned before, this property comes from the use of the *FLEXINOL* ® material in the "spring" component of each control system. As it happens in the material, the control systems are also subjected to some predefined operating limits which are directly related with the SMA alloys modulus of elasticity limits. These operating limits are mainly felt in the "spring" stiffness boundaries and consequently affect the range of frequencies of the vibration controller action. Although not critical, this constraint has been mitigated especially in the Suppressor case, when the implementation of the so-called "transition stiffness" was carried out.

In order to correctly tune the control systems, a frequency tracking algorithm, based on the implementation of the short-time-fourier-transforms (STFT) was developed. This algorithm, computed in the MATLAB (The Mathworks, 2014) software, has the peculiarity of being able to find the vibration frequencies of a specific signal in real time. In order to test the implementation of the two vibration control systems in concern, one as computed a numerical model that performs a temporal analysis of the behavior of a two degree of freedom (TDOF) system. This numerical model computes the acceleration, velocity and displacement of both degrees of freedom (structure and vibration control device) when the primary DOF is subjected to a certain harmonic force.

Thereby, using the aforementioned numerical model, the two control systems with variable stiffness were applied to this thesis case study (footbridge described in section 5.2), and the results, regarding its behavior, were obtained.

Once performed the numerical analysis of the structural behavior, comprising both control systems, it was possible to draw some conclusions:

- Regarding section 7.2 case, for a specific harmonic action (exciting the resonance effect), the structure without any vibration control system, achieves a maximum vertical acceleration of 3,5 m/s^2 which is clearly beyond the 0,7 m/s^2 acceleration limit defined in the literature.

  For the same action, with the implementation of the Suppressor control system the maximum vertical acceleration value decreases to 0,107 m/s^2. With the implementation of the TMD control system, the maximum vertical acceleration achieves values in the order of 0,1315 m/s^2.

  According to these results, the vibration control effects can be rather important, amounting up to a 96% percentage of improvement in both Suppressor and TMD case.

- Regarding the importance of the "variable stiffness" property, section 7.3.1 shown that, in the worst case scenario (regarding the excitation frequency), a Suppressor with variable stiffness can provide up to a 96% of improvement when compared with a "constant stiffness" one.

  Section 7.4.1 shown that a TMD with variable stiffness can provide up to a 31,5% of improvement when compared with a "constant stiffness" one, subjected once again to the worst case scenario.

- Now considering the final numerical model developed, where the STFT algorithm is directly applied to the structural response, one may withdraw some important conclusions.

  Although theoretically the Suppressor with variable stiffness (SVST) present higher efficacy in the vibration control, one should note that this effect only happens for a correct tuning in real time, without any misalignments. Thus, if a failure in the tuning process occurs, the opposite effect might be triggered and the structural acceleration could possibly increase exponentially.

  In the TMD (TMDVS) case, the improvement achieved may not always be so sharp, but the control system features the redundancy property i.e. if something in the tuning process fails, it does not cause major problems, giving it an advantage over the Suppressor (SVST).

The numerical tests performed with the developed models showed that the vibration control mechanism investigated is very efficient for harmonic excitations, achieving substantial reductions in the structural acceleration and displacement, especially for excitation frequencies near the natural frequencies of the structure.

Some examples of this type of dynamic actions, in civil engineering structures, are the already mentioned action of the pedestrians walking rate or even the wind action, which, in some cases, may jeopardize the safety of the structure and/or the comfort of its occupants. Thus, a vibration control mechanism such as the one investigated in this thesis, would actively control the accelerations in the structures using the temperature control of the SMA actuators integrated on it.

8.2 Future Works

In general, the proposed objectives for this dissertation were fulfilled. However, even though the studies carried out in this document successfully yielded a different vibration control system, at least for academic pursuits, there are several aspects of improvement, which can be further studied through an additional research.

Regarding the SMA study:

- Taking into account the difficulties in the real time tuning of the control systems described in this document, it would be important to produce a more complete model, able to accurately predict the SMAs behavior.

  To do so, one might consider the studies carried out by D. Grandi, M. Maraldi and L. Molari [11] [18], where a macroscale phase-field model for shape memory alloys with non-isothermal effects is developed.

  The above mentioned model relies on a Time dependent Ginzburg-Landau free energy model, defined as function of macroscopically measurable quantities, accounting for thermal effects. Based on thermodynamic principles, various relevant physical aspects are established, in particular, the influence of the strain rate and of the ambient conditions on the response of the model.

  Considering the aforementioned, it would be possible to produce a "3-dimensional" model, comprising the variation of the SMAs elastic modulus as function of real time temperature and/or stress variations.

Regarding the Vibration Control Systems in concern:

- In order to experimentally evaluate the studies carried in this dissertation, it would be really interesting to develop a prototype of the vibration control systems concerned. This prototype would then be implemented and tested in a reduced scale model of the section's 5.2 case study structure.

- The main drawback of the presented control systems comes from their, real time, tuning difficulties. Therefore, one would have to implement a specific sensor in the system, measuring the structural acceleration in real time, computing the recorded data into the developed control algorithm.

- Being an active control system, electrically driven by SMA actuators, a movement sensor with specific requirements would need to be implemented in the structure in order to trigger the control system's action, only when strictly necessary.

  To do so, new requirements of fast response, lower power consumption and other promising alternatives should be further studied.

Bibliography

[1] Alam, M. S., Bhuiyan, M. R., and Billah, A. M. Seismic fragility assessment of SMA-bar restrained multi-span continuous highway bridge isolated by different laminated rubber bearings in medium to strong seismic risk zones. *Bulletin of Earthquake Engineering 10*, 6 (2012), 1885–1909.

[2] Bhowmick, S., and Mishra, S. K. Shape memory alloy-tuned mass damper (sma-tmd) for seismic vibration control. In *Advances in Structural Engineering*. Springer, 2015, pp. 1405–1418.

[3] Brinson, L., and Huang, M. Simplifications and comparisons of shape memory alloy constitutive models. *Journal of intelligent material systems and structures 7*, 1 (1996), 108–114.

[4] Chopra, A. K. *Dynamics of structures*, vol. 3. Prentice Hall New Jersey, 1995.

[5] Chopra, I., and Sirohi, J. *Smart structures theory*. No. 35. Cambridge University Press, 2013.

[6] Cismasiu, C., and Dos Santos, F. P. A. Numerical simulation of a semi-active vibration control device based on superelastic shape memory alloy wires. *Corneliu Cismasiu (Ed.), ISBN: 978-953-307-106-0, InTech, Available from: http://www.intechopen.com/books/shape-memory- alloys/numerical-simulation-of-a-semi-active-vibration-control-device-based-on-superelastic-shape-memory-al* (2010).

[7] da Silva Ferreira, F. L. *Controlo semi-ativo de estruturas de engenharia civil*. PhD thesis, FEUP, 2014.

[8] DYNALLOY, I. Technical characteristics of *FLEXINOL* ® actuator wires. Tech. rep., DYNALLOY.

[9] European Committee for Standardization (CEN):. *EN1990: Eurocode 0: Basis of structural design*, 2002.

[10] Follador, M., Cianchetti, M., Arienti, A., and Laschi, C. A general method for the design and fabrication of shape memory alloy active spring actuators. *Smart Materials and Structures 21*, 11 (2012), 115029.

[11] Grandi, D., Maraldi, M., and Molari, L. A macroscale phase-field model for shape memory alloys with non-isothermal effects: Influence of strain rate and environmental conditions on the mechanical response. *Acta Materialia 60*, 1 (2012), 179–191.

[12] Hartog, J. D. *Mechanical vibrations*. Courier Corporation, 1985.

[13] Indirli, M., Castellano, M. G., Clemente, P., and Martelli, A. Demo-application of shape memory alloy devices: the rehabilitation of the s. giorgio church bell tower. In *SPIE's 8th Annual International Symposium on Smart Structures and Materials* (2001), International Society for Optics and Photonics, pp. 262–272.

[14] Ivshin, Y., and Pence, T. J. A thermomechanical model for a one variant shape memory material. *Journal of intelligent material systems and structures 5*, 4 (1994), 455–473.

[15] Krus, T. d. C. A. P. Análise dinâmica e controlo passivo de vibrações de uma ponte pedonal. Master's thesis, FCT-UNL, 2012.

[16] Liang, C., and Rogers, C. A. One-dimensional thermomechanical constitutive relations for shape memory materials. *Journal of intelligent material systems and structures 1*, 2 (1990), 207–234.

[17] Malukhin, K., and Ehmann, K. A model of the kinetics of the temperature-induced phase transformation in niti alloys and its experimental verification. *Journal of Intelligent Material Systems and Structures* (2011), 1045389X11430728.

[18] Maraldi, M., Molari, L., and Grandi, D. A non-isothermal phase-field model for shape memory alloys: Numerical simulations of superelasticity and shape memory effect under stress-controlled conditions. *Journal of Intelligent Material Systems and Structures 23*, 10 (2012), 1083–1092.

[19] Meinhardt, C. Application of tuned mass dampers for bridge decks. In *Footbridge 2008-Third International Conference* (2008).

[20] Mercier, H., Ammann, W. J., Deischl, F., Eisenmann, J., Floegl, I., Hirsch, G. H., Klein, G. K., Lande, G. J., Mahrenholtz, O., Natke, H. G., et al. *Vibration problems in structures: practical guidelines*. Birkhäuser, 2012.

[21] Mizar, S. P. *Thermomechanical characterization of NiTiNOL and NiTiNOL based structures using ACES methodology*. PhD thesis, Worcester Polytechnic Institute, 2005.

[22] Modena, C., Lourenco, P. B., and Roca, P. *Structural Analysis of Historical Constructions-2 Volume Set: Possibilities of Numerical and Experimental Techniques-Proceedings of the IVth Int. Seminar on Structural Analysis of Historical Constructions, 10-13 November 2004, Padova, Italy*. CRC Press, 2004.

[23] Moutinho, C. An alternative methodology for designing tuned mass dampers to reduce seismic vibrations in building structures. *Earthquake Engineering & Structural Dynamics 41*, 14 (2012), 2059–2073.

[24] Moutinho, C. M. R. *Controlo passivo e activo de vibrações em pontes de peões*. PhD thesis, UNIVERSIDADE DO PORTO, 1998.

[25] Nagarajaiah, S., and Sonmez, E. Structures with semiactive variable stiffness single/multiple tuned mass dampers. *Journal of Structural Engineering 133*, 1 (2007), 67–77.

[26] Nagarajaiah, S., and Varadarajan, N. Short time fourier transform algorithm for wind response control of buildings with variable stiffness TMD. *Engineering Structures 27*, 3 (2005), 431–441.

[27] Ostowari, K., and Soroushian, P. Field trial of shape memory-based rehabilitation system. Tech. rep., Transportation Research Board, 2000.

[28] Paredes, M. M., et al. Utilização de amortecedores de massas sintonizadas no controlo de vibrações em estruturas. Master's thesis, FEUP, 2013.

[29] Rao, A., Srinivasa, A., and Reddy, J. *Design of Shape Memory Alloy (SMA) Actuators*. Springer, 2015.

[30] Rodrigues, A. F. T. Estudo de uma estrutura adaptativa baseada no conceito de tensegridade. Master's thesis, FCT-UNL, 2014.

[31] Santos, F. P. A. d. *Vibration control with shape-memory alloys in civil engineering structures*. PhD thesis, FCT-UNL, 2011.

[32] Santos, F. P. A. d., and Cismasiu, C. Vibration control of an under-deck cable-stayed prototype bridge using shape-memory alloys. *No prelo* (2015).

[33] Semião, L. A. P. Utilização de ligas com memória de forma no controlo de vibrações em estruturas inteligentes de engenharia civil. Master's thesis, FCT-UNL, 2010.

[34] Seo, J., Kim, Y. C., and Hu, J. W. Pilot study for investigating the cyclic behavior of slit damper systems with recentering shape memory alloy (SMA) bending bars used for seismic restrainers. *Applied Sciences 5*, 3 (2015), 187–208.

[35] Sétra, Footbridges. *Assessment of vibrational behaviour of footbridges under pedestrian loading - Practical Guidelines*, 2006.

[36] Šittner, P., Michaud, V., and Schrooten, J. Smart materials-fundamentals and applications. Modelling and material design of SMA polymer composites. *Materials transactions 43*, 5 (2002), 984–993.

[37] Song, G., Chaudhry, V., and Batur, C. Precision tracking control of shape memory alloy actuators using neural networks and a sliding-mode based robust controller. *Smart materials and structures 12*, 2 (2003), 223.

[38] Song, G., Ma, N., and Li, H.-N. Applications of shape memory alloys in civil structures. *Engineering structures 28*, 9 (2006), 1266–1274.

[39] Tanaka, K. A thermomechanical sketch of shape memory effect: one-dimensional tensile behavior. *Res Mechanica 18* (1986), 251–263.

[40] Telo, G. J. d. C. Estudo de um actuador baseado em ligas com memória de forma. Master's thesis, Faculdade de Ciências e Tecnologia, 2013.

[41] Tiseo, B., Ameduri, S., Gianvito, A., et al. A shape memory alloys based tuneable dynamic vibration absorber for vibration tonal control. *Journal of Theoretical and Applied Mechanics 48*, 1 (2010), 135–153.

[42] Varadarajan, N., and Nagarajaiah, S. Wind response control of building with variable stiffness tuned mass damper using empirical mode decomposition/hilbert transform. *Journal of engineering mechanics 130*, 4 (2004), 451–458.

[43] Wang, L., and Melnik, R. V. Nonlinear dynamics of shape memory alloy oscillators in tuning structural vibration frequencies. *Mechatronics 22*, 8 (2012), 1085–1096.

[44] Williams, K., Chiu, G.-C., and Bernhard, R. Dynamic modelling of a shape memory alloy adaptive tuned vibration absorber. *Journal of Sound and Vibration 280*, 1 (2005), 211–234.

[45] Williams, K. A., Chiu, G. T.-C., and Bernhard, R. J. Nonlinear control of a shape memory alloy adaptive tuned vibration absorber. *Journal of Sound and Vibration 288*, 4 (2005), 1131–1155.

[46] Zhang, X., Feng, P., He, Y., Yu, T., and Sun, Q. Experimental study on rate dependence of macroscopic domain and stress hysteresis in NiTi shape memory alloy strips. *International Journal of Mechanical Sciences 52*, 12 (2010), 1660–1670.

[47] Zotov, N., Marzynkevitsch, V., and Mittemeijer, E. J. Evaluation of kinetic equations describing the martensite–austenite phase transformation in NiTi shape memory alloys. *Journal of Alloys and Compounds 616* (2014), 385–393.

Appendix

Appendix A

Experimental approach - SMA wire Young Modulus Mapping

This Appendix presents a more detailed analysis of the results of the experimental test described in section 3.3

Table A.1: Test Temperature: 20°C - experimental results

T1=Tenv (°C)	A (m2)	L (m)	g (m/s2)	Laser1 (mm)
20	1,9635E-07	0,45	9,81	0

FLEXINOL® Catalog properties		
E_M (Gpa)	E_A (Gpa)	σ_Ced (Mpa)
28-40	83	345

Weight	Force (N)	Stress (σ) (Mpa)	Laser1- P (mm)	Li (m)	Lf (m)	Lf-Li (m)	ε (m/m)	ε (%)	E (Gpa)	
P10 - Temp	7,05339	35,9226203	0	0,45	0,45	0	0	0		
P11	16,86339	85,88454	0,8	0,45	0,4508	0,0008	0,00177778	0,17777778	28,1035799	
P12	26,67339	135,84646	1,5	0,4508	0,4515	0,0015	0,00333333	0,33333333	32,118377	
P13	36,48339	185,808379	2	0,4515	0,452	0,002	0,00444444	0,44444444	44,9657278	
P14	46,29339	235,770299	2,7	0,452	0,4527	0,0027	0,006	0,6	32,118377	E_20°C
P15	56,10339	285,732219	3,5	0,4527	0,4535	0,0035	0,00777778	0,77777778	28,1035799	(Gpa)
P16	65,91339	335,694139	3,95	0,4535	0,45395	0,00395	0,00877778	0,87777778	49,9619197	33,990774

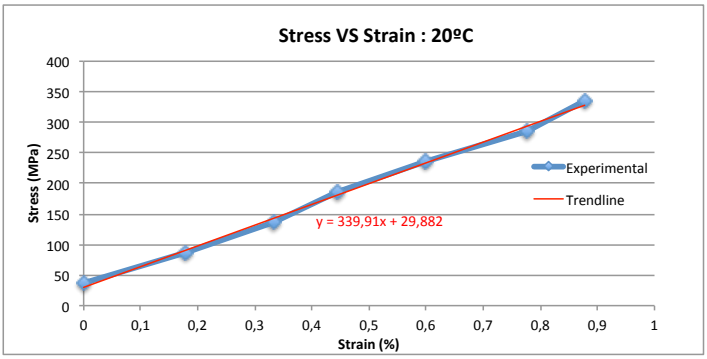

Figure A.1: Stress-Strain curve for 20°C

Table A.2: Test Temperature: 30°C - experimental results

T2 (°C)	A (m2)	L (m)	Laser1 (mm)
30	1,9635E-07	0,4496	0,4

Weight	Force (N)	Stress (σ) (Mpa)	Laser1- P (mm)	Li (m)	Lf (m)	Lf-Li (m)	ε (m/m)	ε (%)	E (Gpa)	
P20 - Temp	7,05339	35,9226203	0	0,4496	0,4496	0	0	0		
P21	16,86339	85,88454	0,9	0,4496	0,4505	0,0009	0,00200178	0,20017794	24,9587546	
P22	26,67339	135,84646	1,5	0,4505	0,4511	0,0015	0,0033363	0,33362989	37,4381319	
P23	36,48339	185,808379	2,1	0,4511	0,4517	0,0021	0,00467082	0,46708185	37,4381319	
P24	46,29339	235,770299	3	0,4517	0,4526	0,003	0,0066726	0,66725979	24,9587546	E_30°C
P25	56,10339	285,732219	3,4	0,4526	0,453	0,0034	0,00756228	0,75622776	56,1571978	(Gpa)
P26	65,91339	335,694139	3,8	0,453	0,4534	0,0038	0,00845196	0,84519573	56,1571978	34,6625462

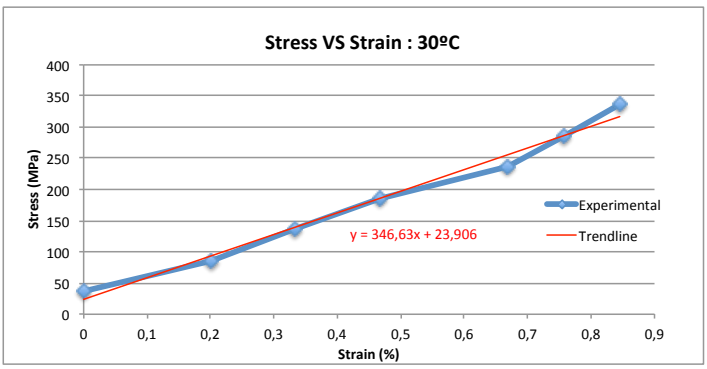

Figure A.2: Stress-Strain curve for 30°C

Table A.3: Test Temperature: 40°C - experimental results

T3 (°C)	A (m2)	L (m)	Laser1 (mm)
40	1,9635E-07	0,4486	1,4

Weight	Force (N)	Stress (σ) (Mpa)	Laser1- P (mm)	Li (m)	Lf (m)	Lf-Li (m)	ε (m/m)	ε (%)	E (Gpa)	
P30 - Temp	7,05339	35,9226203	0	0,4486	0,4486	0	0	0		
P31	16,86339	85,88454	1	0,4486	0,4496	0,001	0,00222916	0,22291574	22,4129172	
P32	26,67339	135,84646	1,5	0,4496	0,4501	0,0015	0,00334374	0,33437361	44,8258344	
P33	36,48339	185,808379	2,35	0,4501	0,45095	0,00235	0,00523852	0,52385198	26,3681379	
P34	46,29339	235,770299	2,8	0,45095	0,4514	0,0028	0,00624164	0,62416407	49,8064827	E_40°C
P35	56,10339	285,732219	3,5	0,4514	0,4521	0,0035	0,00780205	0,78020508	32,0184531	(Gpa)
P36	65,91339	335,694139	4,2	0,4521	0,4528	0,0042	0,00936246	0,9362461	32,0184531	32,9854713

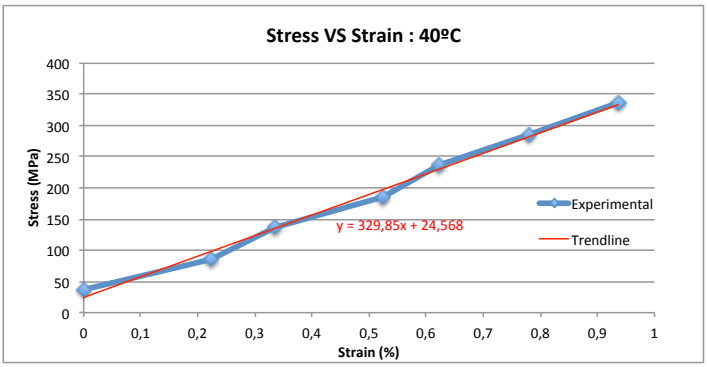

Figure A.3: Stress-Strain curve for 40°C

Table A.4: Test Temperature: 50°C - experimental results

T4 (°C)	A (m2)	L (m)	Laser1 (mm)
50	1,9635E-07	0,445	5

Weight	Force (N)	Stress (σ) (Mpa)	Laser1- P (mm)	Li (m)	Lf (m)	Lf-Li (m)	ε (m/m)	ε (%)	E (Gpa)	
P40 - Temp	7,05339	35,9226203	0	0,445	0,445	0	0	0		
P41	16,86339	85,88454	0,8	0,445	0,4458	0,0008	0,00179775	0,17977528	27,7913179	
P42	26,67339	135,84646	1,6	0,4458	0,4466	0,0016	0,00359551	0,35955056	27,7913179	
P43	36,48339	185,808379	2,2	0,4466	0,4472	0,0022	0,00494382	0,49438202	37,0550905	
P44	46,29339	235,770299	3,6	0,4472	0,4486	0,0036	0,00808989	0,80898876	15,8807531	E_50°C
P45	56,10339	285,732219	4,4	0,4486	0,4494	0,0044	0,00988764	0,98876404	27,7913179	(Gpa)
P46	65,91339	335,694139	5,5	0,4494	0,4505	0,0055	0,01235955	1,23595506	20,2118675	23,9993188

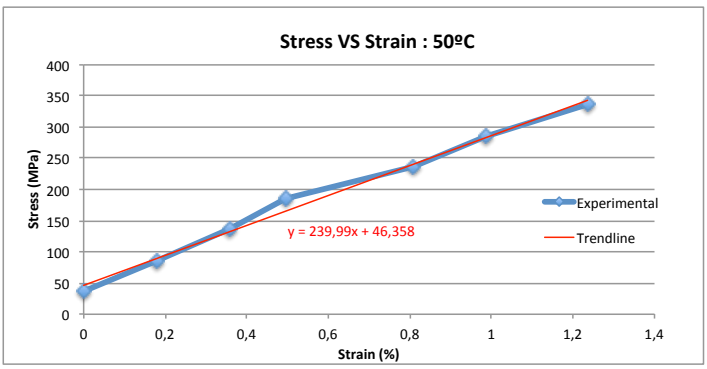

Figure A.4: Stress-Strain curve for 50°C

Table A.5: Test Temperature: 60°C - experimental results

T5 (°C)	A (m2)	L (m)	Laser1 (mm)
60	1,9635E-07	0,4305	19,5

Weight	Force (N)	Stress (σ) (Mpa)	Laser1- P (mm)	Li (m)	Lf (m)	Lf-Li (m)	ε (m/m)	ε (%)	E (Gpa)	
P50 - Temp	7,05339	35,9226203	0	0,4305	0,4305	0	0	0		
P51	16,86339	85,88454	0,3	0,4305	0,4308	0,0003	0,00069686	0,06968641	71,6953548	
P52	26,67339	135,84646	0,6	0,4308	0,4311	0,0006	0,00139373	0,13937282	71,6953548	
P53	36,48339	185,808379	1,3	0,4311	0,4318	0,0013	0,00301974	0,30197445	30,7265806	
P54	46,29339	235,770299	1,8	0,4318	0,4323	0,0018	0,00418118	0,41811847	43,0172129	E_60°C
P55	56,10339	285,732219	2,4	0,4323	0,4329	0,0024	0,00557491	0,55749129	35,8476774	(Gpa)
P56	65,91339	335,694139	3,5	0,4329	0,434	0,0035	0,00813008	0,81300813	19,5532786	36,4258658

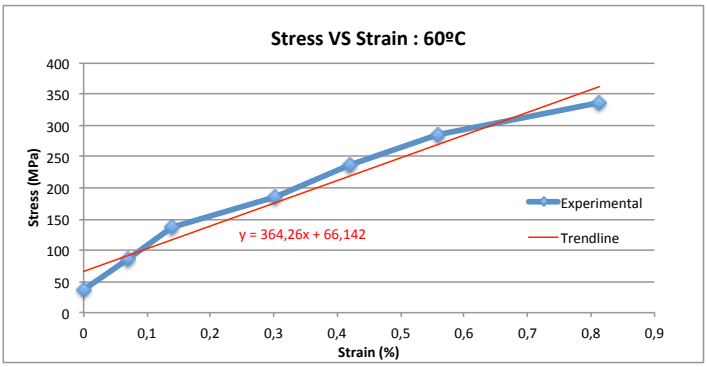

Figure A.5: Stress-Strain curve for 60°C

Table A.6: Test Temperature: 70°C - experimental results

T6 (°C)	A (m2)	L (m)	Laser1 (mm)
70	1,9635E-07	0,43005	19,95

Weight	Force (N)	Stress (σ) (Mpa)	Laser1- P (mm)	Li (m)	Lf (m)	Lf-Li (m)	ε (m/m)	ε (%)	E (Gpa)	
P60 - Temp	7,05339	35,9226203	0	0,43005	0,43005	0	0	0		
P61	16,86339	85,88454	0,15	0,43005	0,4302	0,00015	0,0003488	0,03487967	143,240824	
P62	26,67339	135,84646	0,45	0,4302	0,4305	0,00045	0,00104639	0,104639	71,6204119	
P63	36,48339	185,808379	0,85	0,4305	0,4309	0,00085	0,00197651	0,19765144	53,715309	
P64	46,29339	235,770299	1,4	0,4309	0,43145	0,0014	0,00325544	0,32554354	39,0656792	E_70°C
P65	56,10339	285,732219	1,95	0,43145	0,432	0,00195	0,00453436	0,45343565	39,0656792	(Gpa)
P66	65,91339	335,694139	2,4	0,432	0,43245	0,0024	0,00558075	0,55807464	47,7469413	49,8514433

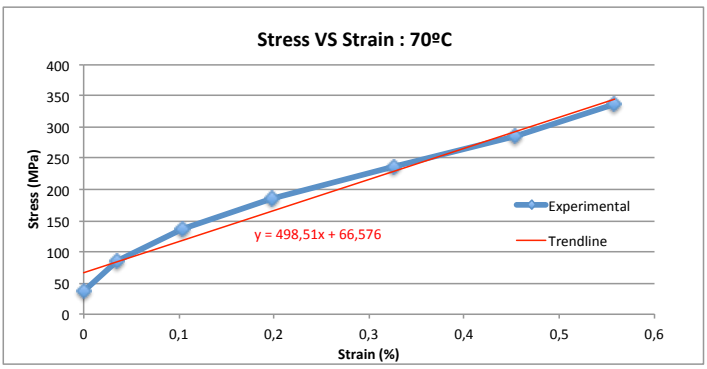

Figure A.6: Stress-Strain curve for 70°C

Table A.7: Test Temperature: 80°C - experimental results

T7 (°C)	A (m2)	L (m)	Laser1 (mm)
80	1,9635E-07	0,43	20

Weight	Force (N)	Stress (σ) (Mpa)	Laser1- P (mm)	Li (m)	Lf (m)	Lf-Li (m)	ε (m/m)	ε (%)	E (Gpa)	
P70 - Temp	7,05339	35,9226203	0	0,43	0,43	0	0	0		
P71	16,86339	85,88454	0,3	0,43	0,4303	0,0003	0,00069767	0,06976744	71,612085	
P72	26,67339	135,84646	0,5	0,4303	0,4305	0,0005	0,00116279	0,11627907	107,418127	
P73	36,48339	185,808379	0,95	0,4305	0,43095	0,00095	0,0022093	0,22093023	47,74139	
P74	46,29339	235,770299	1,3	0,43095	0,4313	0,0013	0,00302326	0,30232558	61,3817871	E_80°C
P75	56,10339	285,732219	1,95	0,4313	0,43195	0,00195	0,00453488	0,45348837	33,0517315	(Gpa)
P76	65,91339	335,694139	2,2	0,43195	0,4322	0,0022	0,00511628	0,51162791	85,9345019	55,1352938

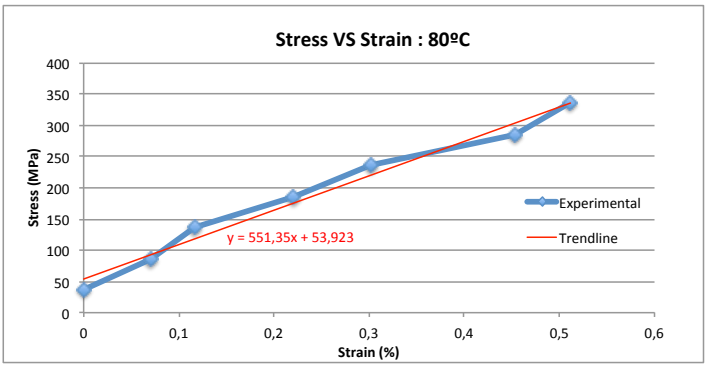

Figure A.7: Stress-Strain curve for 80°C

Table A.8: Test Temperature: 90°C - experimental results

T8 (°C)	A (m2)	L (m)	Laser1 (mm)
90	1,9635E-07	0,43	20

Weight	Force (N)	Stress (σ) (Mpa)	Laser1- P (mm)	Li (m)	Lf (m)	Lf-Li (m)	ε (m/m)	ε (%)	E (Gpa)	
P80 - Temp	7,05339	35,9226203	0	0,43	0,43	0	0	0		
P81	16,86339	85,88454	0,55	0,43	0,43055	0,00055	0,00127907	0,12790698	39,0611372	
P82	26,67339	135,84646	0,8	0,43055	0,4308	0,0008	0,00186047	0,18604651	85,9345019	
P83	36,48339	185,808379	1,2	0,4308	0,4312	0,0012	0,0027907	0,27906977	53,7090637	
P84	46,29339	235,770299	1,6	0,4312	0,4316	0,0016	0,00372093	0,37209302	53,7090637	E_90°C
P85	56,10339	285,732219	2,1	0,4316	0,4321	0,0021	0,00488372	0,48837209	42,967251	(Gpa)
P86	65,91339	335,694139	2,6	0,4321	0,4326	0,0026	0,00604651	0,60465116	42,967251	51,0520507

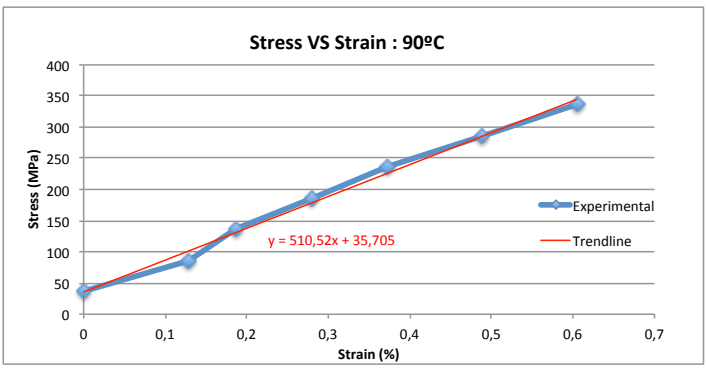

Figure A.8: Stress-Strain curve for 90°C

Table A.9: Test Temperature: 100°C - experimental results

T9 (°C)	A (m2)	L (m)	Laser1 (mm)
100	1,9635E-07	0,43	20

Weight	Force (N)	Stress (σ) (Mpa)	Laser1- P (mm)	Li (m)	Lf (m)	Lf-Li (m)	ε (m/m)	ε (%)	E (Gpa)	
P90 - Temp	7,05339	35,9226203	0	0,43	0,43	0	0	0		
P91	16,86339	85,88454	0,3	0,43	0,4303	0,0003	0,00069767	0,06976744	71,612085	
P92	26,67339	135,84646	0,5	0,4303	0,4305	0,0005	0,00116279	0,11627907	107,418127	
P93	36,48339	185,808379	0,85	0,4305	0,43085	0,00085	0,00197674	0,19767442	61,3817871	
P94	46,29339	235,770299	1,15	0,43085	0,43115	0,00115	0,00267442	0,26744186	71,612085	E_100°C
P95	56,10339	285,732219	1,55	0,43115	0,43155	0,00155	0,00360465	0,36046512	53,7090637	(Gpa)
P96	65,91339	335,694139	2	0,43155	0,432	0,002	0,00465116	0,46511628	47,74139	64,9375277

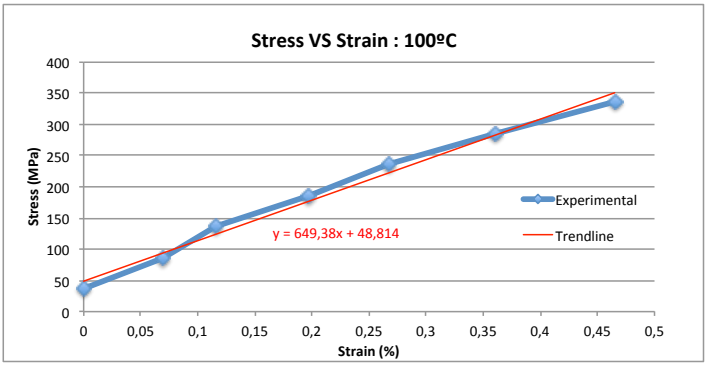

Figure A.9: Stress-Strain curve for 100°C

Table A.10: Test Temperature: 110°C - experimental results

T10 (°C)	A (m2)	L (m)	Laser1 (mm)
110	1,9635E-07	0,43	20

Weight	Force (N)	Stress (σ) (Mpa)	Laser1- P (mm)	Li (m)	Lf (m)	Lf-Li (m)	ε (m/m)	ε (%)	E (Gpa)	
P100 - Temp	7,05339	35,9226203	0	0,43	0,43	0	0	0		
P101	16,86339	85,88454	0,4	0,43	0,4304	0,0004	0,00093023	0,09302326	53,7090637	
P102	26,67339	135,84646	0,7	0,4304	0,4307	0,0007	0,00162791	0,1627907	71,612085	
P103	36,48339	185,808379	1	0,4307	0,431	0,001	0,00232558	0,23255814	71,612085	
P104	46,29339	235,770299	1,2	0,431	0,4312	0,0012	0,0027907	0,27906977	107,418127	E_110°C
P105	56,10339	285,732219	1,7	0,4312	0,4317	0,0017	0,00395349	0,39534884	42,967251	(Gpa)
P106	65,91339	335,694139	2,3	0,4317	0,4323	0,0023	0,00534884	0,53488372	35,8060425	58,7442884

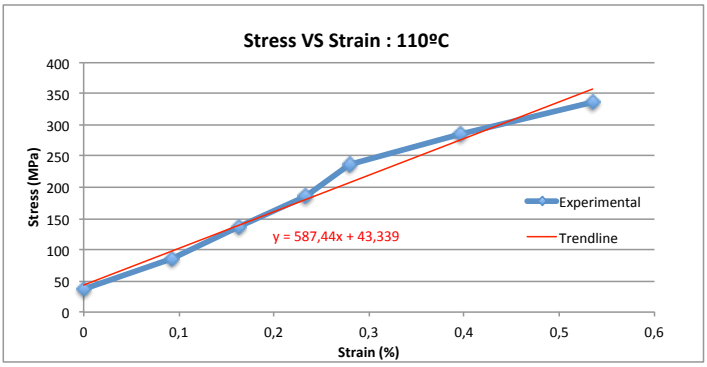

Figure A.10: Stress-Strain curve for 110°C

Appendix B

Proportional-Integral-Derivative (PID) Control Algorithm

This appendix describes the PID algorithm used in the experimental procedure of chapter 3.

The PID controller calculates the error between a variable value being measured and a specific target value. Then, the controller seeks to minimize this error through a response that depends on three parameters: P - proportional, I - integral and D - derivative.

- P, depends on the present error,
- I, dependes upon the accumulation of errors in the past,
- D, is a prediction of future errors.

The basic operating principle behind a PID controller is given by: Considering the data recorded with a sensor (Input signal), obtain an Output signal capable of producing the expected system's response by adding a proportional, integral and derivative calculation in real time.

According to the PID algorithm, the output response $u(t)$ produced by the controller can be mathematically represented by:

$$u(t) = K_p\, e(t) + K_i \int_o^t e(\tau)d\tau + K_d \frac{d\, e(t)}{dt} \tag{B.1}$$

Where:

- K_p - proportional gain (tuning parameter);
- K_i - integral gain (tuning parameter);
- K_d - derivative gain (tuning parameter);
- e - error;
- t - instantaneous time;
- τ - variable of integration (taking values between 0 and the present time).

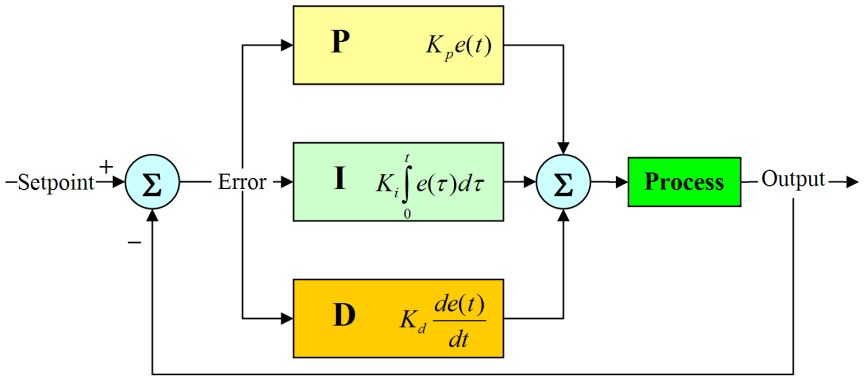

Figure B.1: Proportional-Integral-Derivative (PID) Controller layout.

During the experimental test, the PID algorithm compares the value of the instantaneous temperature of the wire (read by the thermocouple) with a target temperature value previously set, calculating the error and consequently the response to be imposed to the system (through the previously defined gains), in order to change the wire's temperature. This process is repeated sequentially until the desired temperature becomes reached.

Appendix C

Numerical approach - SMA wire Young Modulus Mapping

This Appendix presents a more detailed analysis of the results of the numerical approach described in section 3.4

Table C.1: Heat Flux values from DSC curve (M → A transition).

Heat Flux	
T(ºC)	DSC(mW/mg)
X	Y
39,962013	0,07701863
44,94777	0,07282609
48,93637	0,06653727
52,725548	0,05291149
55,717	0,032996893
58,11016	0,015178571
59,905033	-0,014169254
60,902184	-0,042468943
62,298195	-0,07181677
63,295345	-0,09697205
64,292496	-0,12003106
65,09022	-0,14728262
66,08737	-0,17138976
66,88509	-0,19968945
67,48338	-0,22379659
68,48053	-0,23742236
69,27825	-0,23113354
69,27825	-0,21645963
69,477684	-0,19759317
69,67712	0,17663044
70,07597	-0,1525233
70,275406	-0,13051242
70,47483	-0,11059783
70,873695	-0,088586956
71,07313	-0,066576086
71,471985	-0,044565216
71,67142	-0,02150621
72,26971	0,001552795
72,868	0,023563664
73,26685	0,04138199
74,662865	0,05291149
76,45774	0,061296582
78,45204	0,06653727
80,44634	0,070729814
84,434944	0,07492236
90,01899	0,07806677
39,962013	0,07806677

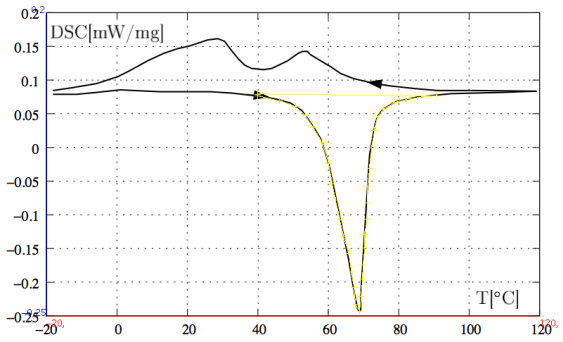

Figure C.1: Heat Flux - PlotDigitizer analisys.

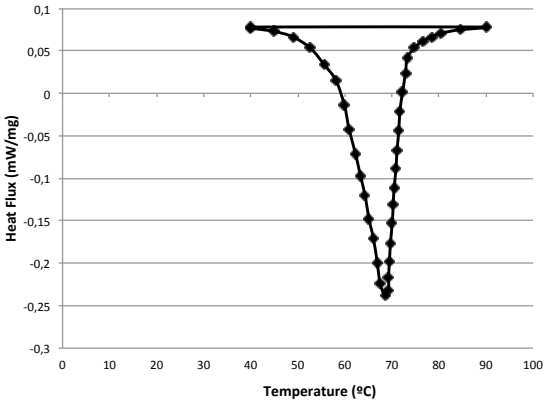

Figure C.2: Heat Flux [mW/mg].

Table C.2: Baseline-corrected-unsmeared Heat Flux values.

Unsmeared Heat Flux	
T(ºC)	Fu (mW/mg)
0	0
5	0
10	0
15	0
20	0
25	0
30	0
35	0
39,962013	0
44,94777	1,04515E-05
48,93637	3,97157E-05
52,725548	0,000105247
55,717	0,000207149
58,11016	0,000333821
59,905033	0,000471154
60,902184	0,000576191
62,298195	0,000763482
63,295345	0,000924435
64,292496	0,001109427
65,09022	0,001277488
66,08737	0,001513169
66,88509	0,001722617
67,48338	0,00189538
68,48053	0,002202132
70	0
75	0
80	0
85	0
90	0
95	0
100	0

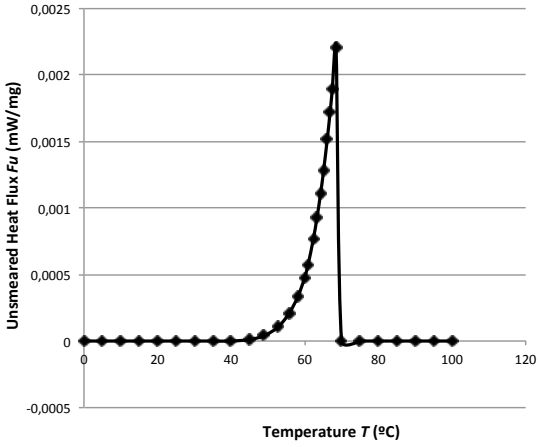

Figure C.3: Unsmeared Heat Flux of the $M \rightarrow A$ transformation.

Table C.3: Austenite phase fraction (DSC analysis).

Austenite Fraction	
T(ºC)	f(T)
0	0
5	0
10	0
15	0
20	0
25	0
30	0
35	0
39,962013	0
44,94777	0,001863299
48,93637	0,009018356
52,725548	0,028659794
55,717	0,062076213
58,11016	0,108369483
59,905033	0,160033614
60,902184	0,197377882
62,298195	0,264252462
63,295345	0,324437001
64,292496	0,396956646
65,09022	0,465043423
66,08737	0,564547331
66,88509	0,65684771
67,48338	0,734249887
68,48053	0,88035113
70	1
75	1
80	1
85	1
90	1
95	1
100	1

Table C.4: Fit parameters.

Fit Parameters			f(T)
g	v	Tm	(df/dtmax)
0,225	6	68,3619723	0,8629802

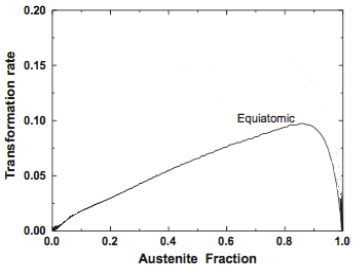

Figure C.4: Transformation rate.

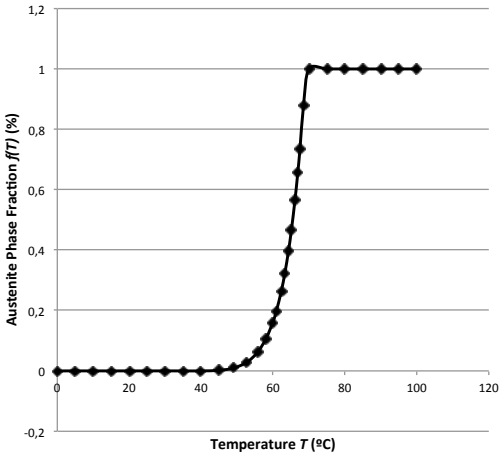

Figure C.5: Austenite phase fraction evolution (DSC analysis).

Table C.5: Austenite phase fraction (Equation (2.3)).

Austenite Fraction	
T(ºC)	f(T,g,v,Tm)
0	2,08893E-07
5	6,43436E-07
10	1,98192E-06
15	6,10475E-06
20	1,88039E-05
25	5,79202E-05
30	0,000178407
35	0,000549532
39,962013	0,001678272
44,94777	0,0051529
48,93637	0,012641623
52,725548	0,029652896
55,717	0,058127362
58,11016	0,099593544
59,905033	0,149148446
60,902184	0,186661321
62,298195	0,255534893
63,295345	0,319764845
64,292496	0,399989837
65,09022	0,478000152
66,08737	0,594911332
66,88509	0,702172005
67,48338	0,784975461
68,48053	0,902379686
70	0,982822877
75	0,999978623
80	0,999999975
85	1
90	1
95	1
100	1

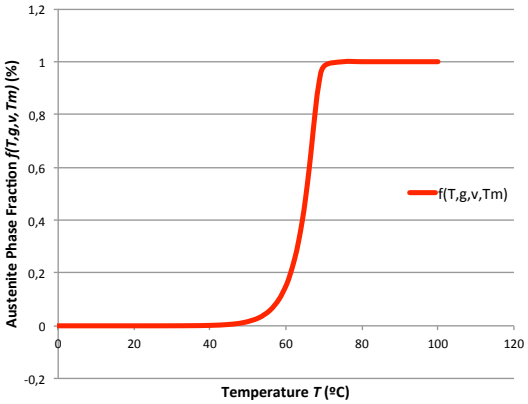

Figure C.6: Austenite phase fraction (Equation (2.3)).

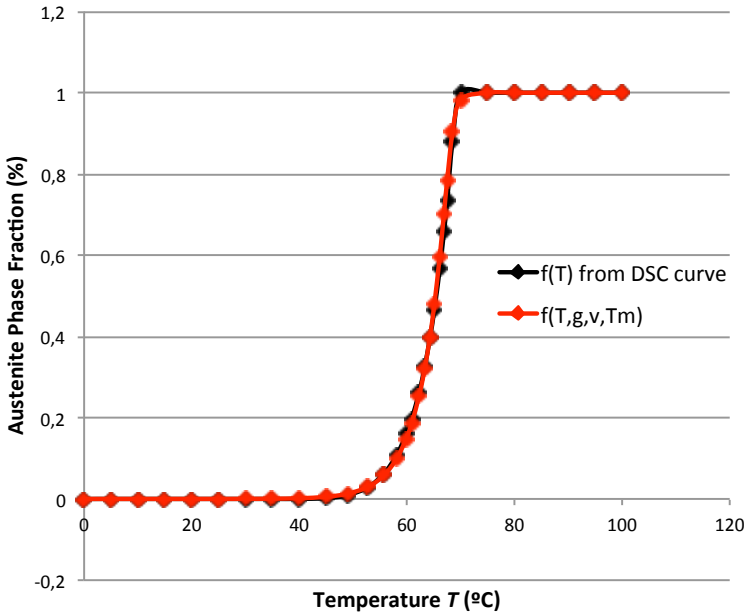

Figure C.7: Suitability of equation (2.3) to the graphical data of Figure 3.11. Figures C.5 and C.6 overlay.

Table C.6: Voight scheme (E vs. T).

Voight Model Young Modulus	
T(ºC)	E(Gpa)
0	34
5	34
10	34
15	34
20	34
25	34
30	34
35	34
39,962013	34
44,94777	34,05776227
48,93637	34,27956904
52,725548	34,88845361
55,717	35,9243626
58,11016	37,35945397
59,905033	38,96104203
60,902184	40,11871434
62,298195	42,19182632
63,295345	44,05754703
64,292496	46,30565603
65,09022	48,41634611
66,08737	51,50096726
66,88509	54,36227901
67,48338	56,7617465
68,48053	61,29088503
70	65
75	65
80	65
85	65
90	65
95	65
100	65

Table C.7: Young Modulus in Martensite/Austenite phase.

Em (Gpa)	Ea (Gpa)
34	65

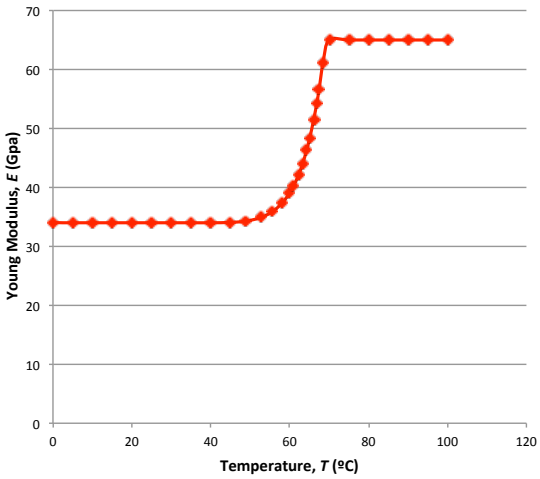

Figure C.8: Voight scheme - Modulus of elasticity as function of temperature.

Table C.8: Reuss scheme (E vs. T).

Reuss Model Young Modulus	
T(ºC)	E(Gpa)
0	34
5	34
10	34
15	34
20	34
25	34
30	34
35	34
39,962013	34
44,94777	34,03024098
48,93637	34,1468678
52,725548	34,47116977
55,717	35,03729952
58,11016	35,85302439
59,905033	36,80943299
60,902184	37,53314785
62,298195	38,90285248
63,295345	40,22390484
64,292496	41,93998508
65,09022	43,6900032
66,08737	46,52726324
66,88509	49,50969608
67,48338	52,32223912
68,48053	58,60651998
70	65
75	65
80	65
85	65
90	65
95	65
100	65

Table C.9: Young Modulus in Martensite/Austenite phase.

Em (Gpa)	Ea (Gpa)
34	65

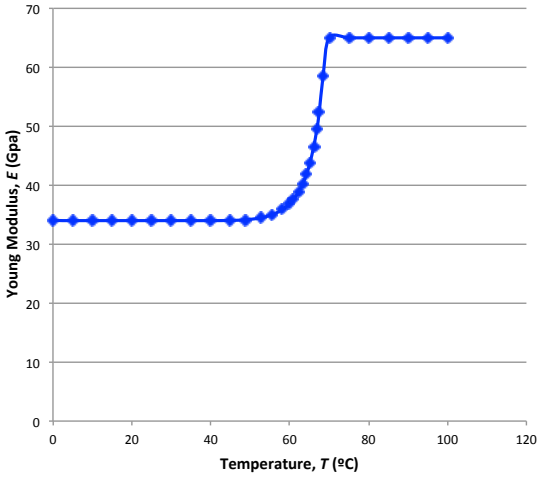

Figure C.9: Reuss scheme - Modulus of elasticity as function of temperature.

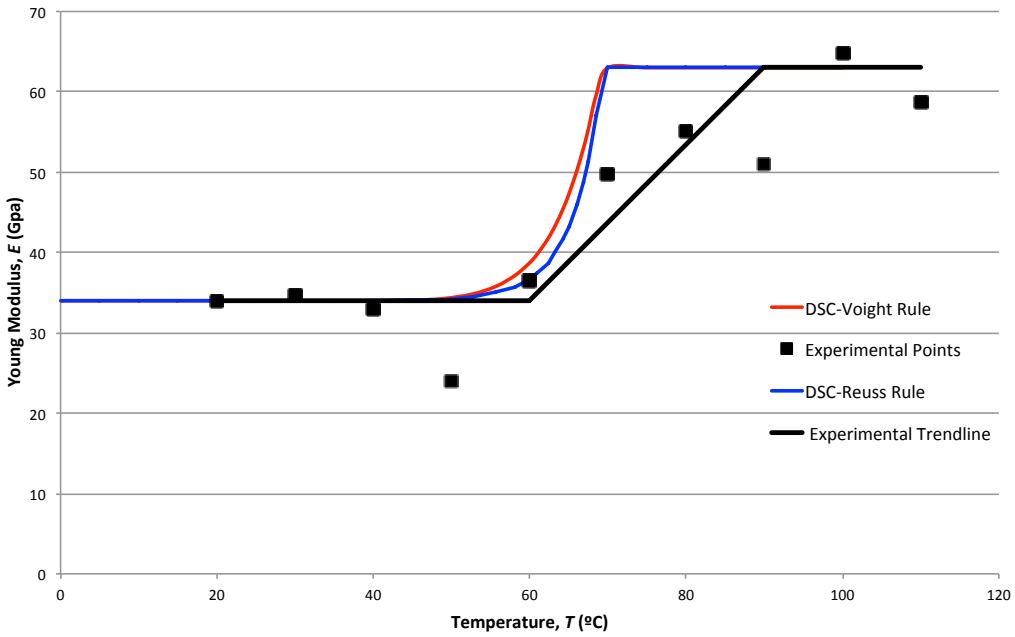

Figure C.10: Experimental approach Vs. Numerical approach - Young modulus of the SMA wire.

Appendix D

Design of SMA Wires Under Constant Force

This Appendix presents all the numerical data of section 5.4 and section 5.5. It also displays a stiffness-temperature mapping of the SMA element, used in the vibration control system.

Appendix D. Design of SMA Wires Under Constant Force

Table D.1: Design of Shape Memory Alloy (SMA) actuators.

Masses		m2/m1	Structure's natural frequency	Force in the wire	Max Stress	Wire's minimum Area	Wire's minimum Diameter	Wire's Length	Young Modulus		Stiffness	
m1	m2	μ	fn	F	σ_max	A_min	d_min	L	E_Martensite	E_Austensite	K_Martensite	K_Austensite
(kg)	(kg)	-	(Hz)	(N)	(Pa)	(m^2)	(mm)	(m)	(GPa)	(GPa)	(kN/m)	(kN/m)
10680	440	0,041199	3,03	4312	103000000	4,1864E-05	7,30	15	40	83	111,6375	231,6479

Table D.2: Stress influence in the wire's strain/stiffness.

Strain		Length		Stiffness		"error" (%)	
Martensite	Austenite	Martensite	Austenite	Martensite	Austenite	Martensite	Austenite
ε_M	ε_A	L+ε_M	L+ε_A	K (L+ε_M)	K (L+ε_A)	ΔK	ΔK
(m/m)	(m/m)	(m)	(m)	(kN/m)	(kN/m)	(%)	(%)
0,002575	0,00124096	15,0386	15,0186	111,350812	231,3608	-0,2568	-0,1239

Table D.3: Temperature influence in the wire's strain/stiffness.

Strain				Total Strain		Stroke	Length		Stiffness		"error" (%)	
Martensite		Austenite		ε_total		S	Martensite	Austenite	Martensite	Austenite	Martensite	Austenite
ε_M		ε_A		(ε_M-ε_A)		(ε_M-ε_A)*L	L+ε_M	L+ε_A	K (L+ε_M)	K (L+ε_A)	ΔK	ΔK
(m/m)	%	(m/m)	%	(m/m)	%	(m)	(m)	(m)	(kN/m)	(kN/m)	(%)	(%)
0,002575	0,2575	0,05	5	-0,0474	-4,7425	-0,7114	15,0386	14,3273	111,3508	242,5251	-0,2568	4,6956

- Suppressor:

Table D.4: Suppressor operating limits - Numerical values.

frequency				Operating limits	
Martensite		Austenite		Martensite	Austenite
ω_supp	f_supp	ω_supp	f_supp	f_supp/fn	f_supp/fn
(rad/s)	(Hz)	(rad/s)	(Hz)	(Hz/Hz)	(Hz/Hz)
15,9082	2,5319	23,4775	3,7366	0,8356	1,2332

Table D.5: Suppressor operating limits - Considered values.

frequency		Operating limits		Stiffness limits	
Martensite	Austenite	Martensite	Austenite	Martensite	Austenite
f_supp	f_supp	f_supp/fn	f_supp/fn	K_M	K_A
(Hz)	(Hz)	(Hz/Hz)	(Hz/Hz)	(kN/m)	(kN/m)
2,54	3,73	0,8383	1,2310	112,07	241,67

- TMD:

Table D.6: TMD operating limits - Numerical values.

frequency						Operating limits	
Martensite			Austenite			Martensite	Austenite
ω_2optm	ω_exc	f_exc	ω_2optm	ω_exc	f_exc	f_exc/fn	f_exc/fn
(rad/s)	(rad/s)	(Hz)	(rad/s)	(rad/s)	(Hz)	(Hz/Hz)	(Hz/Hz)
15,9082	16,5636	2,6362	23,4775	24,4447	3,8905	0,8700	1,2840

Table D.7: TMD operating limits - Considered values.

frequency		Operating limits		Stiffness limits	
Martensite	Austenite	Martensite	Austenite	Martensite	Austenite
f_exc	f_exc	f_exc/fn	f_exc/fn	K_M	K_A
(Hz)	(Hz)	(Hz/Hz)	(Hz/Hz)	(kN/m)	(kN/m)
2,6447	3,8836	0,8728	1,2817	112,07	241,67

- SMA E and K Mapping considering new E_M and E_A values - Reuss Model:

Table D.8: Reuss scheme (E vs. T).

Reuss Model Young Modulus	
T(ºC)	E(Gpa)
0	40
5	40
10	40
15	40
20	40
25	40
30	40
35	40
39,962013	40
44,94777	40,0386503
48,93637	40,1877637
52,725548	40,6028651
55,717	41,3291439
58,11016	42,3793113
59,905033	43,6161724
60,902184	44,5561324
62,298195	46,3446727
63,295345	48,0816515
64,292496	50,3557786
65,09022	52,6957923
66,08737	56,5352109
66,88509	60,6331247
67,48338	64,5572082
68,48053	73,5409735
70	83
75	83
80	83
85	83
90	83
95	83
100	83

Table D.9: Young Modulus in Martensite/Austenite phase.

Em (Gpa)	Ea (Gpa)
40	83

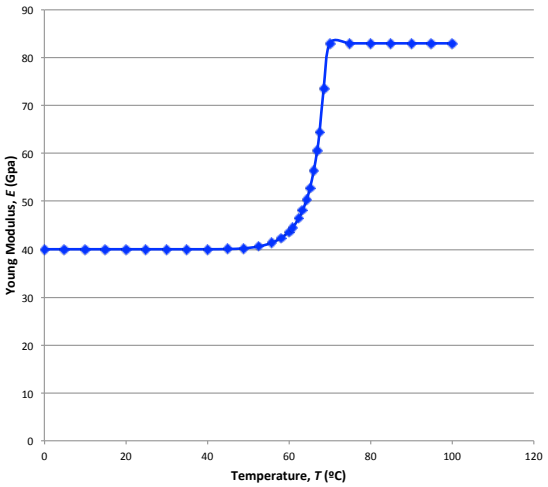

Figure D.1: Reuss scheme - Modulus of elasticity as function of temperature.

Table D.10: SMA Stiffness.

Stiffness			A (m^2)
T(ºC)	L (m)	K (kN/m)	4,1854E-05
0	15,0386	111,323842	
5	15,0386	111,323842	
10	15,0386	111,323842	
15	15,0386	111,323842	
20	15,0386	111,323842	
25	15,0386	111,323842	
30	15,0386	111,323842	
35	15,0386	111,323842	
39,962013	15,0386	111,323842	
44,94777	14,991173	111,78394	
48,93637	14,943746	112,55634	
52,725548	14,896319	114,080999	
55,717	14,848892	116,492499	
58,11016	14,801465	119,835307	
59,905033	14,754038	123,729214	
60,902184	14,706611	126,803278	
62,298195	14,659184	132,320041	
63,295345	14,611757	137,724923	
64,292496	14,56433	144,708621	
65,09022	14,516903	151,927911	
66,08737	14,469476	163,531648	
66,88509	14,422049	175,961877	
67,48338	14,374622	187,967995	
68,48053	14,327195	214,834391	
70	14,327195	242,466935	
75	14,327195	242,466935	
80	14,327195	242,466935	
85	14,327195	242,466935	
90	14,327195	242,466935	
95	14,327195	242,466935	
100	14,327195	242,466935	

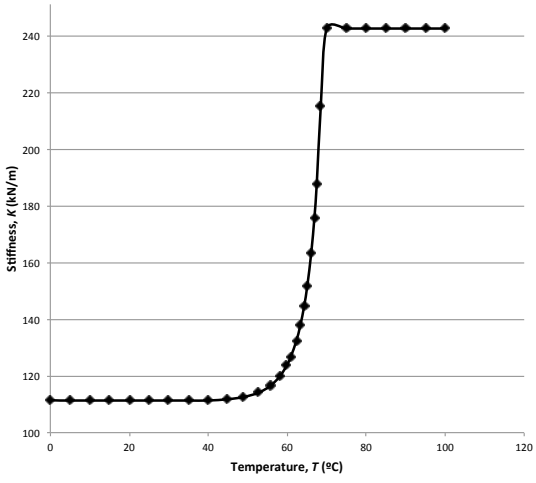

Figure D.2: Stiffness mapping as function of temperature.

Appendix E

Short-time Fourier transforms - MATLAB implementation

This appendix describes the MATLAB implementation of the simple STFT frequency-tracker model, mentioned in section 6.3.2.

Throughout the following function, the STFT frequency-tracker model returns the frequency-time spectrogram of a specific signal:

$$[\text{S,F,T,ps}] = \text{spectrogram(x,window,noverlap,nfft,fs)} \tag{E.1}$$

where,

Output Arguments:

- **S** - Short-time Fourier transform, returned as a matrix. Time increases across the columns of S and frequency increases down the rows, starting from zero.
- **F** - Cyclical frequencies, returned as a vector. F has a length equal to the number of rows of S.
- **T** - Time instants, returned as a vector. The time values in T correspond to the midpoint of each section.
- **ps** - Power spectral density (PSD) or power spectrum, returned as a matrix.

Input Arguments:

- **x** - Input signal, specified as a row or column vector.
- **window** - Window, specified as an integer or as a row or column vector. Use window to divide the signal into sections.
- **noverlap** - Number of overlapped samples, specified as a positive integer. If window is a vector, then noverlap must be smaller than the length of window.
- **nfft** - Number of DFT (Discrete Fourier transform) points, specified as a positive integer scalar. This parameter must be large enough to provide good frequency-time results, but if too large, it will introduce high computational effort.
- **fs** - Sample rate, specified as a positive scalar. The sample rate is the number of samples per unit time. If the unit of time is seconds, then the sampling frequency is in Hz.

Appendix F

Vibration Control Algorithm

This appendix displays a representative diagram of the final control algorithm for both control systems.

Appendix F. Vibration Control Algorithm

- Suppressor SVST - Vibration control algorithm:

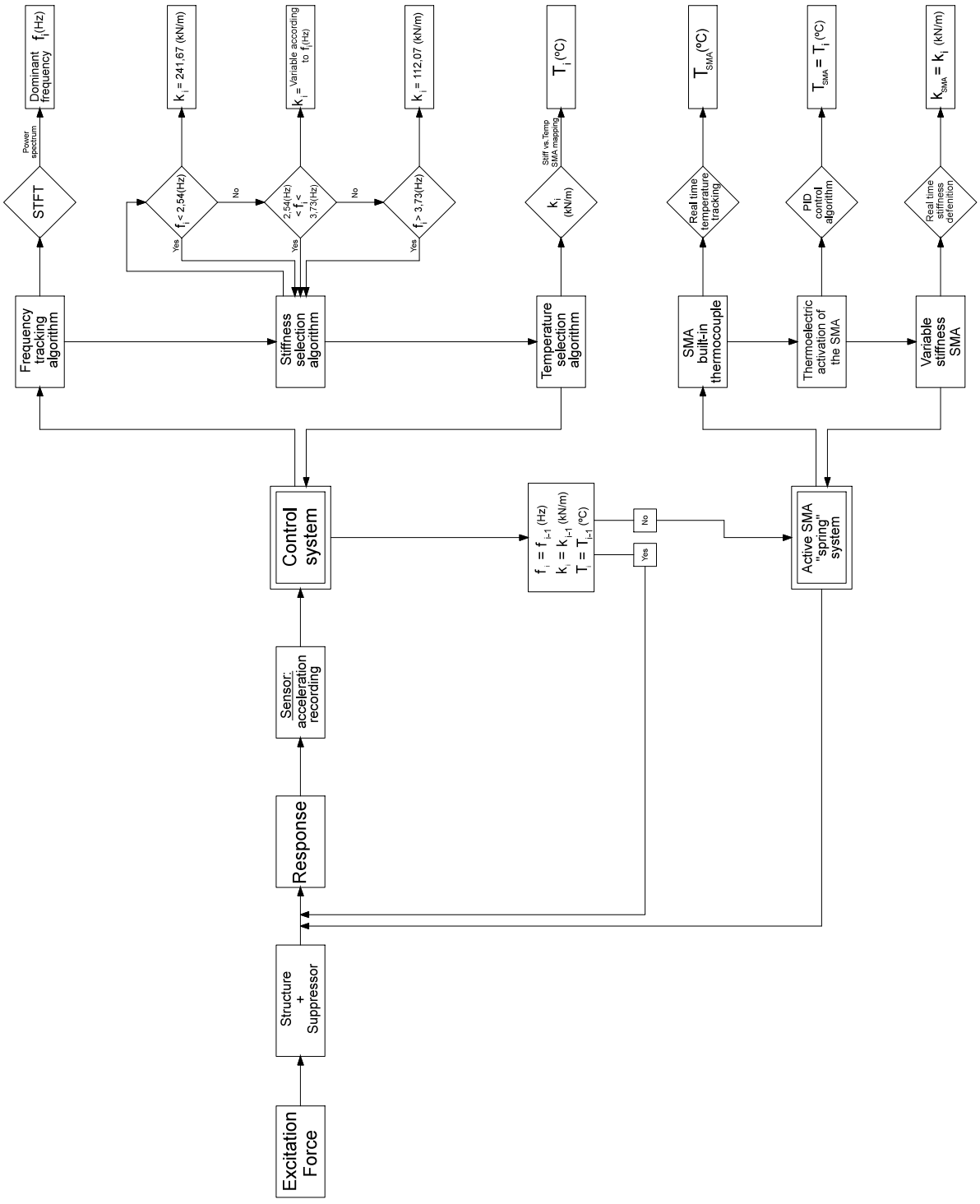

Figure F.1: Suppressor Vibration control algorithm.

- Tuned mass damper TMDVS - Vibration control algorithm:

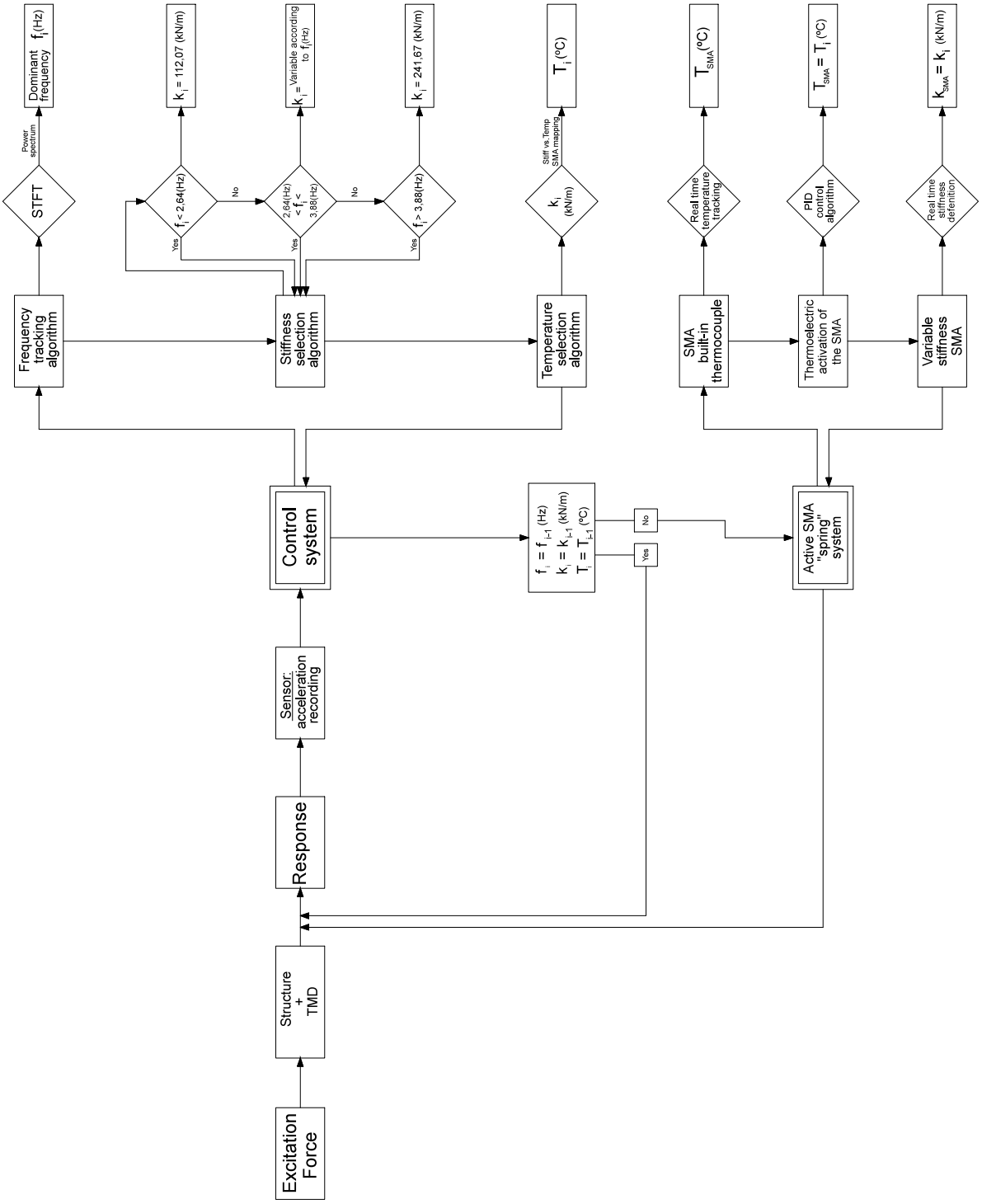

Figure F.2: TMD Vibration control algorithm.